Ana Cristina Marques Ribeiro

**Magnetic hyperthermia
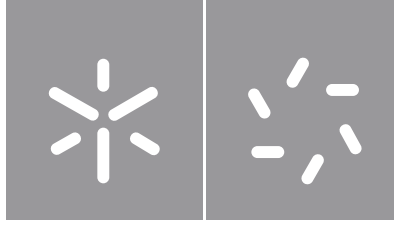assisted genetic amplification**

**Magnetic hyperthermia assisted
genetic amplification**

Ana Ribeiro

UMinho | 2022

october 2022

Universidade do Minho
Escola de Ciências

Ana Cristina Marques Ribeiro

Magnetic hyperthermia assisted genetic amplification

Master Thesis
Master in Biophysics and Bionanosystems

Work developed under the supervision of
Doctor Juan Gallo Páramo
and
Professor Doctor Paulo José Gomes Coutinho

october 2022

ACKNOWLEDGMENTS

First and foremost, I would like to express my sincere gratitude to my primary supervisor, Dr. Juan Gallo Páramo, for providing me with the necessary advice, encouragement, conversations, and patience, all of which contributed to the most beneficial learning process. I am thankful to Dr. Manuel Banõbre for the opportunity to integrate his research group and for his thoughtfulness and willingness to help throughout this process. I also want to express my gratitude to Professor Dr. Paulo Coutinho for his valuable teachings that ultimately led me here.

I would like to thank Dr. Sanna Sillankorva for guiding me through this journey, for all the advice and patience.

I am grateful for my parents and my dear sisters, for their sacrifice and encouragement that allowed me to achieve all of my academic accomplishments. Thank you for teaching me determination and perseverance. I would like to express my gratitude to my boyfriend, Ricardo, for his unconditional support, for always calming me and listening throughout every step of this journey. I would like to thank Marta and Catarina for their friendship and advice.

Special thanks to Dr. Milene, Nuria, and my colleagues Beatriz, Cátia, Raquel, Vitor and Celso for all opinions and discussions regarding this project, as well as the conversations.

Finally, I want to thank the University of Minho and the institution that accepted me, specially the INL Nanomedicine group, that provided all resources for the conclusion of this dissertation.

STATEMENT OF INTEGRITY

I hereby declare having conducted this academic work with integrity. I confirm that I have not used plagiarism or any form of undue use of information or falsification of results along the process leading to its elaboration.

I further declare that I have fully acknowledged the Code of Ethical Conduct of the University of Minho.

Título: Amplificação genética assistida por hipertermia magnética

RESUMO

A amplificação controlada de um gene desejado envolvido em uma patologia humana poderia potencialmente permitir o tratamento. Para isso, nano-vetores que combinem capacidades de diagnóstico e tratamento são de grande interesse. Muitos relatórios propuseram sistemas de entrega capazes de distribuir as ferramentas necessárias para amplificação de genes aos tecidos, mas esses sistemas carecem de especificidade e controlo. A combinação de enzimas termo-estáveis com nanopartículas magnéticas (MNPs) e hipertermia na forma de campos magnéticos alternados (AMF), pode ser um fator revolucionário neste campo. Enzimas termo-estáveis (por exemplo, *Taq* polimerase) atingem sua atividade ideal em temperaturas bem acima da temperatura corporal e a aplicação de AMF a nanopartículas magnéticas pode induzir especificamente e localmente um aumento na temperatura. Isso, quando as MNPs são funcionalizadas com as enzimas termoestáveis, permitirá um controle sob demanda da atividade enzimática, aumentando a especificidade e reduzindo potenciais efeitos fora do alvo. Nesta tese, nanopartículas de magnetite foram sintetizadas pelo método hidrotérmico e funcionalizadas via reações de acoplamento peptídico com a *Taq* polimerase. A amplificação de um gene selecionado foi possível com nanopartículas de magnetite revestidas com ácido poliacrílico (Fe$_3$O$_4$@PAA) funcionalizadas com *Taq*, pois esta enzima manteve sua funcionalidade após a funcionalização. O grande potencial de aquecimento da magnetite é explorado ao longo do projeto, à medida que as temperaturas necessárias para as fases específicas de amplificação do gene são atingidas (sob campos magnéticos alternados). A amplificação assistida por hipertermia magnética foi tentada, mas sem sucesso. O sistema desenvolvido mostrou-se enzimaticamente funcional e capaz de gerar calor. Apesar de não ter conseguido provar a prova de conceito, esse esforço abre caminho para a amplificação gênica controlada externamente e representa o primeiro exemplo de uma nova tecnologia para a ativação sob demanda de enzimas com controle espacial.

Palavras-chave: Amplificação genética, Distúrbios genéticos, Hipertermia magnética, Nanopartículas magnéticas, Reação em Cadeia de Polimerase.

Title: Magnetic hyperthermia assisted genetic amplification

ABSTRACT

The controlled amplification of a desired gene involved in a human pathology could potentially allow for treatment. To this end, nano-vectors that combine diagnosis and treatment capabilities are of great interest. Many reports have proposed delivery systems able to distribute the necessary tools for gene amplification to tissues, but these systems lack specificity and control. The combination of thermostable enzymes with magnetic nanoparticles (MNPs) and hyperthermia in the form of alternating magnetic fields (AMF), can be a game changer in this field. Thermostable enzymes (e.g. *Taq* polymerase) reach their optimal activity at temperatures well above body temperature and the application of AMF to magnetic nanoparticles can specifically and locally induce an increase in temperature. This, when the MNPs are functionalised with the thermostable enzymes, will enable an on-demand control of the enzymatic activity, increasing specificity and reducing potential off-target effects. In this thesis, magnetite nanoparticles were synthesised by the hydrothermal method and were functionalized via peptide coupling reactions with *Taq* polymerase. Amplification of a selected gene was possible with *Taq*-functionalised polyacrylic acid coated magnetite nanoparticles (Fe_3O_4@PAA), as this enzyme retained its functionality after functionalization. Magnetite great heating potential is further explored throughout the project, as the temperatures required for the specific phases of gene amplification are attained (under alternating magnetic fields). Magnetic hyperthermia assisted amplification was attempted, yet unsuccessful. The developed system proved to be enzymatically functional and capable of heat generation. Despite being unsuccessful in proving the proof-of-concept, this effort pave the way for externally controlled gene amplification, and represents the first example of a new technology for the on-demand activation of enzymes with spatial control.

Keywords: Genetic amplification, Genetic disorders, Magnetic hyperthermia, Magnetic nanoparticles, Polymerase Chain Reaction.

MOTIVATION

Many human diseases have a genetic component. The consequences of genetic disorders may have no impact on health or development, but they can also be life threatening. The need of research to better understand these disorders, as well as to develop new tools for their diagnosis and treatment is pressing. A new methodology for gene amplification, with the long term of in vivo applications, may contribute to solving this problem.

This study will comprise the creation, development, and characterisation of a new system combining magnetic nanoparticles (with both great heat generation capabilities and MRI contrast) with thermostable enzymes (*Taq* polymerase, genetic amplification enzyme) and magnetic hyperthermia, to address the challenge of specific and local gene amplification in vivo. On top of this, there is an immense variety of purposes that this new concept (MNPs+thermostable enzymes+AMF) could be applied to with little changes in its composition.

TABLE OF CONTENTS

LIST OF TABLES

LIST OF ABBREVIATIONS AND ACRONYMS

AMF – alternated magnetic fields

BSA – bovine serum albumin

CFU – colony-forming units

CPMG – Carr-Purcell-Meiboom-Gill

DLS – dynamic light scattering

DNA – deoxyribonucleic acid

dNTPs - deoxyribonucleotide triphosphate

EDC - 1-ethyl-3-(3-dimethylaminopropyl)

ELS – electrophoretic light scattering

Fe_3O_4@PAA – polyacrylic acid bounded magnetite nanoparticles

Fe_3O_4@PAA-*Fluorescein* – polyacrylic acid bounded magnetite nanoparticles with *fluorescein cadaverine* functionalized

Fe_3O_4@PAA-BSA – polyacrylic acid bounded magnetite nanoparticles with Bovine Serum Albumin functionalized

Fe_3O_4@PAA-*Taq* - polyacrylic acid bounded magnetite nanoparticles with *Taq* polymerase functionalized

FT-IR – fourier transform infra-red spectroscopy

H_c - coercivity

ILP – intrinsic loss power

IR – Infra-Red

MH – magnetic hyperthermia

MNPs – magnetic nanoparticles

M_r - remanence

MRI – magnetic resonance imaging

M_s - magnetic saturation

MWCO - molecular weight cut-off

NPs – nanoparticles

ρ - density

PAA – polyacrylic acid

PAANa - sodium polyacrylate

PBS - phosphate buffered saline

PCR – Polymerase Chain Reaction

PDI – polydispersity index

PES - polyether sulfone

SAR – specific absorption rate

SPIONs – superparamagnetic iron oxide nanoparticles

sulfo-NHS - N-hydroxysulfosuccinimide sodium salt

T – temperature

T_E – time to echo

TEM – transmission electron microscopy

TGA – thermogravimetric analysis

T_I – inversion time

T_R – repetition time

UV-Vis – ultraviolet-visible

VSM – vibrating samples magnetometer

χ_i - initial susceptibility

XRD – X-ray diffraction

CHAPTER ONE:

INTRODUCTION

CHAPTER ONE: INTRODUCTION

1. Gene therapy

Recent advances in genetic research have associated over 3000 genes with disease phenotypes[1] and brought gene therapy to the forefront of scientific research, as a promising therapeutic tool for the treatment of several human pathologies. US Food and Drug Administration describes human gene therapy as "products that mediate their effects by transcription or translation of transferred genetic material or by specifically altering host (human) genetic sequences[2]." Gene therapy techniques alter genes to treat or cure diseases. This is accomplished by replacing unhealthy genes with healthy ones, inactivating genes, or even introducing new genes.

There are different types of genetic therapy currently being developed: cell-based gene therapy, RNA therapy, and epigenetic therapy[3]. Examples of diseases with gene therapy treatments available are Leber congenital amaurosis and spinal muscular atrophy. However, those treatments manipulate DNA differently than gene therapy.

Gene amplification involves an increase in the number of copies of a gene sequence[4,5], which can also result in an increase in RNA and protein from that gene. It is a natural procedure that occurs in cells to favour growth and/or survival. However, gene amplification in pathological tissues, such as cancer cells, can have a detrimental impact for human health, as it is often used by cancer cells to promote tumour growth[4]. Recently, artificial gene amplification has also been exploited in the laboratory, to amplify certain genes for research purposes. However, the primary application of amplification of a gene is the induction of overproduction of protein[6,7].

Regardless of the final objective, genetic amplification is a powerful tool for the diagnose of infections[8], and human biology and pathologies[9,10]. This process is involved in cellular adaptation to cytotoxic drugs and tumorigenesis[5,11–13]. Also, it has the potential of allowing for genetic improvement by correcting an altered/mutated gene or even being employed *in-situ* therapeutic treatments[14]. The careful and premeditated design of vehicles able to deliver extrachromosomal material to target cells and, consequently, their optimization could potentially allow for the treatment has made possible to potentially treat of an array of health problems such as cystic fibrosis, haemophilia, muscular dystrophy, sickle cell anaemia, cancer, and even viral infections[14]. It makes for an extremely interesting research subject. And so, in this thesis the main goal we aim to achieve is the execution of genetic amplification of selected genetic material on demand, using magnetic nanoparticles.

A vector is a symbolic vehicle designed to deliver therapeutic genetic material from one cell to another. Vectors can be of different natures, such as plasmidial, nanostructured, or even viral. They all have different purposes and different efficacies in introducing genetic material into cells. That is why an efficient and safe mechanism that provides all these needs is necessary. Some nanostructured vehicles can be advantageous vectors for genetic material delivery, due to their biocompatible composition, size, charge, and ease of modifying functional groups on the surface of these nanoparticles, making them versatile constructs that can be manipulated and applied accordingly to the final purpose. The combination of the different capacities of these tools can be very promising in the biomedical field, for example, to treat diseases originated by genetic mutations or other genetic complications. Making use of these innovative ideas, it is possible to think of a theranostic system that can amplify DNA under very specific circumstances with accurate results, to improve a broad list of conditions/diseases just by altering its basic components. These pathologies could be addressed through the combination of gene amplification tools and nanoparticles. The main challenge stands beside the *in vivo* control of the nanostructure, may it be temporal or spatial.

However, there are a number of cellular barriers that can impact the successful application of this type of vectors[15]. Upon internalisation through the plasma membrane by endocytosis [15], the vectors need to circumvent the endosomal pathway to then find its way inside the nucleus (in eucaryotic cells), which would most likely require targeting the nanoparticles towards this organelle[15]. Moreover, the efficacy of this gene delivery depends on the system being biocompatible and stable, as well as being able to transfer exogenous genetic materials to a targeted specific site with maximum therapeutic efficacy[15,16]. To decrease the number of barriers to overcome, we will deal with bacteria which have plasmid DNA, since it is a simpler system to study.

Despite recent developments in this area, there are limitations to the systems and technologies already in use[1], such as lack of efficiency, moderate toxicity, host immune response, short-term correction[17–19], and new and better alternatives are actively being investigated. Indeed, genome amplification tools arise to become the solution to this ongoing challenge, surpassing past constraints.

1.1. Polymerase Chain Reaction

The Polymerase Chain Reaction (PCR) is a standard technique used to produce copies of a specific DNA fragments *in vitro* from only trace amounts of DNA – it is a highly sensitive assay.

This technique relies on a DNA polymerase for linking individual nucleotides together to form the PCR product, and on DNA primers, designed specifically for the amplification of the region of interest (amplicon), serving as an extension point. The process itself is quite simple: the PCR instrument rises and lowers the temperature of the sample to achieve its purpose.

Different DNA polymerases can amplify DNA and depending on the application they are designed to amplify longer or shorter regions with possibly different yields. In this work, was used the *Taq* polymerase, a thermostable enzyme isolated from *Thermus aquaticus*, a bacteria. This enzyme presents a low enzymatic activity at 37 °C, and its optimal activity is achieved at a much higher temperature (approximately 72 °C)[20]. As this enzyme can survive long periods of time at high temperatures, it facilitates the PCR process, enabling multi-cycle methodology[20].

Experimentally, as represented in **Figure 1**, the solution is heated above the melting point of the complementary DNA strands, in what is known as the denaturation stage, at which point the two complementary DNA strands separate. Next, for the primers (short DNA seeding sequences specific to the region to copy) to bind with specificity to the target DNA, the temperature is lowered – known as hybridization or annealing stage. At this point, the temperature is again elevated so that the polymerase can extend the primers – extending stage[21].

Nanomaterials have been proposed to be used to enhance the efficiency of PCR amplification, in a technique titled nanomaterial-assisted PCR[22]. Higashi *et al.*, 2015[22], were able to amplify target DNA using heat generated from magnetic nanoparticles under high-frequency magnetic fields. This PCR application was achieved by simple adsorption of the PCR components on to the nanoparticle surface[23]. However, this adsorption can be affected by the concentration of the components, the enzyme used, as well as the presence of other proteins[23] being thus difficult to control and reducing the robustness of the process. Additionally, the high macroscopic temperatures required for the PCR were only achieved with high superparamagnetic iron oxide nanoparticles (SPIONs) concentrations, which is incompatible with *in vitro* or *in vivo* applications – subjecting cells to 57, 72 or 95 °C would lead to cell death.

1.1.1. Colony PCR

Colony PCR is a useful technique for screening a desired DNA sequence by PCR in intact bacteria, fungi, yeast or even microalgae[24,25]. An initial step at high temperature (95 °C) is essential for the bacteria lysis and chains denaturation. The main benefit of this methodology is that DNA purification is not required - a small aliquot of bacteria culture is enough for amplification[24,25].
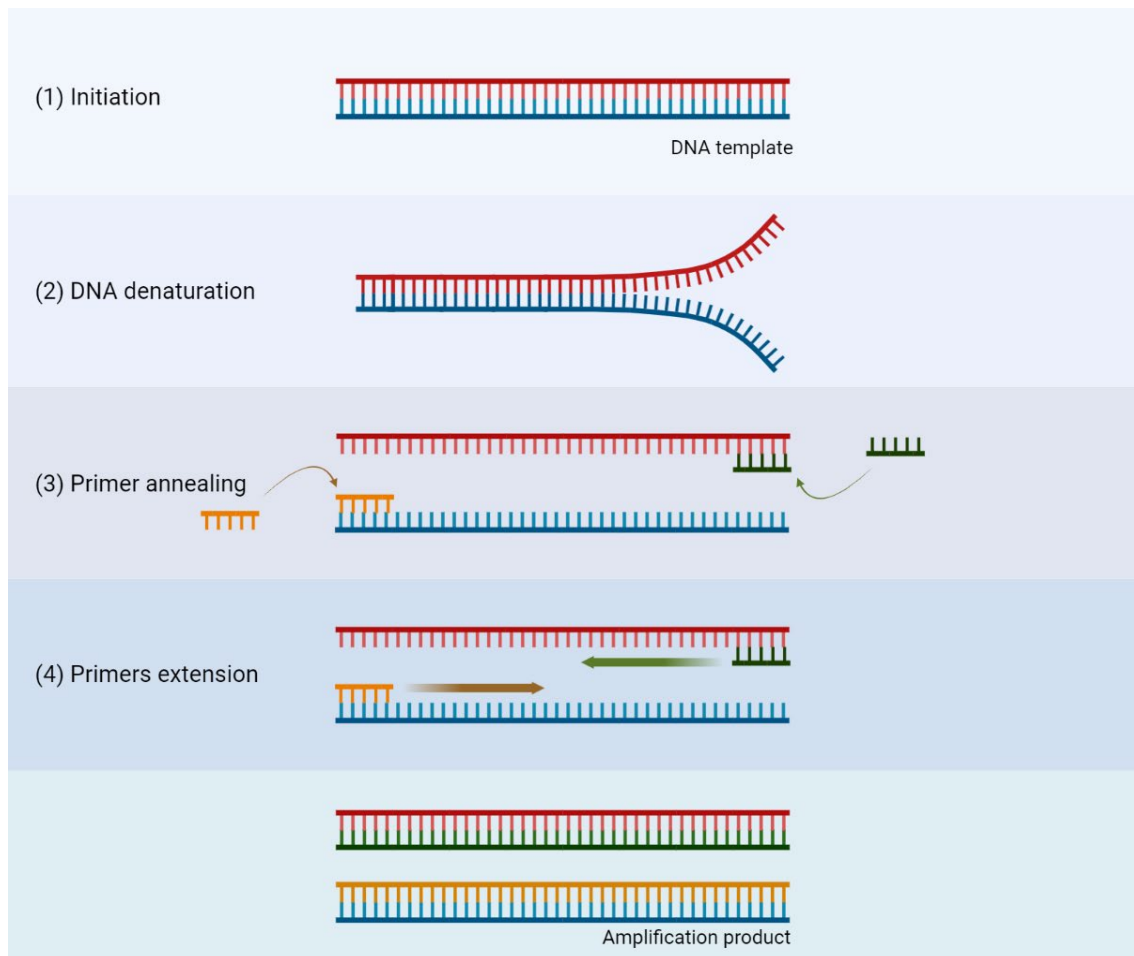
Figure 1. Steps of a PCR reaction.

1.2. Primers for GFP amplification

A gene named EGFP, specific of pCMV-GFP plasmid, which codes For the Enhanced Green Fluorescent Protein, is commonly used for biological applications [26]. Amplification of the EGFP gene requires the proper forward and reverse primers, as well as free deoxyribonucleotide triphosphate (dNTPs), a DNA polymerase of choice (*Taq* polymerase) and the DNA template (pCMV-GFP).

The primers provide a starting point for the DNA synthesis, by allowing their extension after annealing. They are designed to flank the target region of amplification, so their sequences are matches for binding by complementary base pairing in opposite strands of this chosen region - the forward and reverse primer. Additionally, these primers need to be very carefully designed. Primers should be specific and unique to the complementary sequence on the DNA template, but they also need to have similar melting temperatures (the temperature at which half the DNA duplex will dissociate and become single stranded) to the annealing temperature (temperature at which the PCR primers bind to the complementary template region) and between themselves (about 5 °C between them) – higher melting temperature promotes hybridization and extension of an undesired DNA sequence, while lower melting temperature leads to annealing failure. In general, the primers

length should be between 18 and 22 nucleotides. Moreover, they should not have complementary regions between themselves.

The GC percentage in the primers should be between 40 and 60 %, as it relates to the annealing temperature and stability of the primer itself. Since the guanine cytosine pair presents three hydrogen bonds and the adenine thymine two bonds, the higher the content of guanine and cytosine the higher the annealing temperature. The 3' end of the primer should be one guanine or cytosine nucleotide as it promotes binding – named the GC clamp. If the GC content is too high, it can lead to mismatch[27].

2. Nanomedicine

Nanomedicine is an interdisciplinary field, first studied by the father of Nanotechnology, Richard P. Feyman, in 1959[28]. Now, in the 21st century nanotechnology is becoming a key tool in biomedical research. As the name suggests, it encompasses all technology/science/engineering at the nano scale (1 a 100 nm)[29,30], where changes in the chemical, physical and mechanical properties that occur with this size reduction are taken advantage of[31]. More broadly, nanotechnology is focused on three branches: nanomaterials, molecular nanotechnology and biotechnology[32]. Driven by the immense possibilities made feasible by nanotechnology, we can attain a future perspective with countless diagnostics and therapeutics possibilities that can benefit every subfield of medicine. Moreover, nanomedicine complements general medicine by using a more specific approach, which is based on targeting techniques – to achieve the desired clinical outcomes while reducing side effects[33].

Nanotechnology is shaping the diagnostic methodology, drug-release techniques, and regenerative medicine in the modern world[34] (**Figure 2**). Diagnostic technology is currently limited, as the existing methodologies frequently detect existing diseases in an advanced stage[34]. Early detection allows for earlier treatment, diminishing potential damage to the remaining organism[34]. In diagnostic applications, nanoparticles can provide higher sensitivity than traditional methodologies, allowing for detection in smaller samples and/or more accurate measurements[34,35]. The application of nanotechnology in medical diagnostics can be done through *in vitro* diagnostic devices (e.g., nanobiosensors, microarrays or Lab-on-a-Chip) and/or *in vivo* imaging[34]. For medical applications (molecular imaging), some types of these nanoparticles can be used *in vivo* as markers in various imaging techniques, such as Infra-Red (IR) or magnetic resonance imaging (MRI) methods to increase the resolution and sensitivity[36]. The potential diagnostic and screening
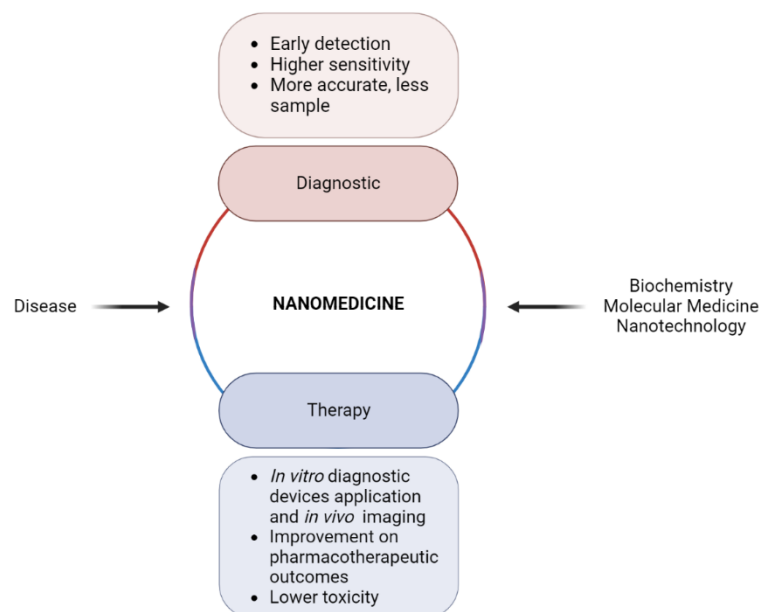
Figure 2. Nanomedicine possible applications in the diagnostic and therapeutic courses of diseases. Created with BioRender.com.

applications of nanostructures can provide a more accurate prognosis, as well as increased chances of effective treatment. Therapeutic applications of nanomedicine include the design of nanovehicles capable of improving pharmacotherapeutic outcomes through the targeted bioaccumulation in the desired tissues, which simultaneously lowers toxicity to healthy cells and increases effectiveness in pathological tissues[34]. Given that the physical and chemical processes involved can be better controlled and even intensified, nanomedicine emerges as a molecular medicine complement[36].

There are endless problems one can approach with nanotechnology, which is rapidly proving to be a major asset in the development of novel treatments for human pathologies.

3. Magnetic nanoparticles

Magnetic nanoparticles (MNPs) are a category of particles that are capable of being controlled by an external magnetic field. Magnetic elements including iron, nickel, cobalt, and their oxides are frequently found in MNPs[37]. Magnetic nanoparticles have high scientific interest in biomedical applications as they are multifunctional and can be used both for diagnostic (magnetic sensing, magnetic resonance imaging) and therapeutic (magnetic hyperthermia, magnetic guidance) applications, as well as for sample preparation (magnetic separation, analyte enrichment)[38–42].

7

3.1. Superparamagnetic behaviour

Magnetic materials are categorized based on their susceptibility to magnetic fields: paramagnetic, diamagnetic, ferromagnetic, ferrimagnetic, antiferromagnetic materials[43,44]. Superparamagnetic materials share some properties of paramagnetic and ferromagnetic materials: the absence of magnetization when the external magnetic field is removed (as paramagnetic materials) and the high levels of magnetization in the presence of low magnetic field (as ferromagnetic materials). Specifically, the structure of ferromagnetic materials domains is dependent on 3 different energetic terms: the magnetostatic energy, that is responsible for the formation of the Weiss domains; the anisotropic energy, that limits the thickness of the Bloch walls (walls that separate the domains); and the exchange energy, that is responsible for the ferromagnetic behaviour (favours the pairing of parallel electronic spins)[45]. So, below a critical size it is less energetically favourable to form a Bloch wall than to support the magnetostatic energy of a monodomain, resulting in nanoparticles consisting of a single magnetic domain[46], particularly in ferromagnetic and ferrimagnetic materials[47]. This domain is constituted by a collective coupling of spins, that are collinear along one direction[48]. The critical size of the single-domain is affected by various factors, including the shape of the particles[49].

Superparamagnetism is a form of magnetism present in ferromagnetic and ferrimagnetic materials. If or when the size of magnetic nanoparticles is critically small, below a certain limit, their magnetization can flip direction randomly[44]. In the superparamagnetic state, when no magnetic field is applied and the measurement time is superior to the time between flips (Néel relaxation time), the average magnetization of the nanoparticles is zero[50]. However, in the presence of an applied magnetic field these nanoparticles show great susceptibility[50]. Superparamagnetism of the nanoparticles is an interesting magnetic feature as it has an enormous potential in applications as targeted drug delivery[51], high-density storage media of data[52] or biosensors[53].

The blocking temperature (T_B) of a material is defined as the temperature between the blocked and superparamagnetic states of said material[54,55]. Below the T_B, the thermal energy is much smaller than the energy associated with the anisotropy barrier and, thus, the magnetization persists null and the magnetic moments of the nanoparticles become blocked[44,56]. But above the blocking temperature, nanoparticles exhibit superparamagnetic behaviour[48], as the magnetic moments of the particles are randomly oriented by thermal excitations[57]. Since T_B of SPIONs is below room temperature, when present in the body their magnetic moments are not blocked, and therefore, are able to react to the applied alternating magnetic field (AMF).

3.2. Physico-chemical properties of nanoparticles

Nanoparticles' properties influence their *in vivo* behaviour: their size, surface charge and morphology (shape) affect their circulation time and biodistribution within the body[58], which makes understanding the correlation between these crucial[59].

The morphology of nanoparticles is strongly affected and can be, to a certain extent, controlled by the synthesis/preparation methodology[49]. There is evidence that the shape of magnetic nanomaterials can alter thermal conductivity and dynamic viscosity of the nanofluid that they constitute[60]. Shape is critically important in how the nanoparticles navigate through the body, their ability to overcome biological barriers and their circulation time, as different shapes create different immunological responses (e.g. being more or less likely to suffer opsonization)[58].

The surface charge of nanoparticles affects their interaction with biological components, and consequently, their fate in the biodistribution and cellular uptake[61]. It is easier for positively charged NPs to be internalized than neutral or negatively charged ones, but they are also more rapidly cleared from the plasma[61,62]. It is critical to find the balance between those outcomes by planning the design of the nanoparticles with their application in mind. Surface modification, protein adsorption and synthesis methods play an important role in the surface charge and can be used to manipulate properties of the final product[61].

Preferably, after application of a formulation, the NPs should remain in the body in circulation until they reach their target, overcoming the main physiological, physical, and chemical barriers. These nanoparticles can be captured by cells of the reticuloendothelial system[63] and/or be eliminated via filtration by the lungs, liver, kidneys or spleen[58]. Their small size is advantageous because the nanoparticles can extravasate through the endothelium or penetrate microcapillaries, have an efficient uptake by various types of cells and allow target site drug accumulation[64]. A smaller size results in a subsequent higher surface-to-volume ratio, leading to, for example in the case of magnetic nanoparticles, superparamagnetism, or in the case of quantum dots or upconversion nanoparticles to high quantum yields and photostable luminescence[65]. Still size-wise, the presence of a polydisperse suspension can result in unexpected behaviours from NPs.

3.3. Ferrite nanoparticles: magnetite

Ferrite nanoparticles have been widely used in biomedical research and industry. Magnetite (Fe_3O_4) have great magnetic properties, biocompatibility and biodegradability[66], and have already been approved by the Food and Drug Administration for *in human* applications as MRI

contrast agents[66] and started clinical trials for hyperthermia in cancer[67], metastatic breast cancer[68] and recurrent glioblastoma[69]. Bulk magnetite is a ferrimagnetic material, a common iron oxide constituted of iron II and iron III that shows strong magnetism[65].

Magnetite crystals have a face centered cubic spinel (cubic inverse spinel) structure of a general formula $(A)[B_2]O_4$: in which A are the divalent metal ions (Fe^{2+}) in tetrahedral interstitial sites, in B are the trivalent metal ions (Fe^{3+}) in the largest octahedral interstitial sites, and the oxygen is located in a cubic compacted arrangement[44,59,70]. The crystal structure of magnetite is shown in **Figure 3**[59]. For magnetite nanoparticles, the unique physico-chemical properties described above occur for sizes below 30 nm in diameter, and they are referred to as superparamagnetic iron oxide nanoparticles, SPIONs[65]. These properties strongly depend on the synthesis and on the nonmagnetic matrix or substrate. Not only magnetite superparamagnetic properties but also their biocompatibility, are a great benefit in biomedical studies and applications. Research groups have use magnetite as MRI contrast agents, thermoablation agents, for magnetically guided drug delivery, and magnetic hyperthermia. This last example applies to this project as there will be manipulation of magnetite nanoparticles with an external magnetic field. Also, surface modifications can improve colloidal stability, distribution, efficiency and recognition. On top of that functionalization of nanoparticles can act as protection for the inorganic core or even enhance or add different properties[65,71].
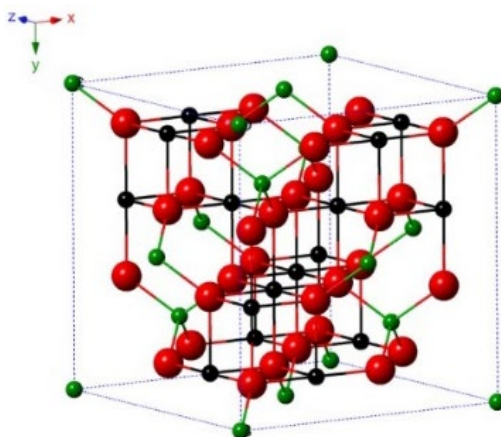
Figure 3. Crystal structure of magnetite.

3.4. Biomedical applications

SPIONs are one of the preferred materials in medical sciences, due to their minimal toxicity, low sensitivity to oxidation and all of the above referred characteristics[72]. They can be

considered the gold standard of nanoparticle application into human health as they have been used in the clinic since the 1990s.

These nanoparticles are used for their contrast agent qualities in MRI. Due to their distinct magnetic properties that react to an applied magnetic field and enable them to have a targeted distribution on the body, iron oxide nanoparticles are also widely used in guided drug administration[72,73]. Moreover, magnetic separation is another fundamental biomedical application, for example in the form of immunomagnetic purification of certain cells from bodily fluids[74]. They can also be used sensing applications, e.g. magneto-resistive platforms[75,76]. Additionally and more relevant for this Thesis, SPIONs can also be employed in conventional magnetic hyperthermia[77] to generate heat.

3.4.1. Magnetic Hyperthermia

Homeostatic control mechanisms of our body keep the body temperature extremely regulated[78]. Hyperthermia is the elevation of temperature beyond normal on the whole body, a region or only a local spot. Hyperthermia effects on mammalian cells are pleiotropic and a short exposure to heat at 40 or 41 °C can cause growth inhibition, cytotoxicity, can alter signal transduction pathways, induce resistance to heat, among other effects[79]. Temperatures above 42 °C can present severe consequences to the structural and functional proteins within cells, leading to necrosis[80]. The increase in macroscopic temperature here referred is fundamentally different from nanoscopic temperature increases, and their effects would also be different. It is critical to control the outcome of the hyperthermia stimulation by an external AMF, so that in *in vitro* and *in vivo* scenarios the cellular integrity is not compromised. In order for the nanoparticles to be safe for hyperthermia application they need to be: responsive to magnetic fields; biocompatible and non-toxic for the organisms; water compatible, as most reactions happen in an aqueous environment; stable (they are protected and are surface-stable); and do not suffer aggregation – the control of nanoparticle aggregation lies on the control of the strength of repulsive forces, which can be achieved through steric stabilization by particularly coating the MNPs (as already discussed), depending on the ionic strength and pH of solution[33,81].

Due to their magnetic properties, magnetic nanoparticles obey Coulomb's law and react accordingly to the application of an external magnetic field gradient[82]. Here, we explore this notion in the practice of induced heat by an electromagnetic field locally by SPIONs capacity of magnetization. This approach shows low toxicity and has been explored on cancer treatments and other applications[83].

11

Magnetite nanoparticles do not experience coercive force since they consist of single-domain particles. Therefore, they are only magnetized in the presence of an external magnetic field, showing a strong and fast magnetic response to said field[84]. It is extremely important to register that this response is without remnant (residual) magnetization and without coercivity[85] in the absence of applied field. This is demonstrated in **Figure 4**[48] since the nanoparticles present a sigmoid curve (*M vs H*) that passes through the origin (pseudo-zero coercivity and residual magnetization, red line). The application of an alternated magnetic field (AMF) triggers magnetic nanoparticles (like SPIONs) to generate heat by magnetic hysteresis losses and/or Néel relaxation[85].
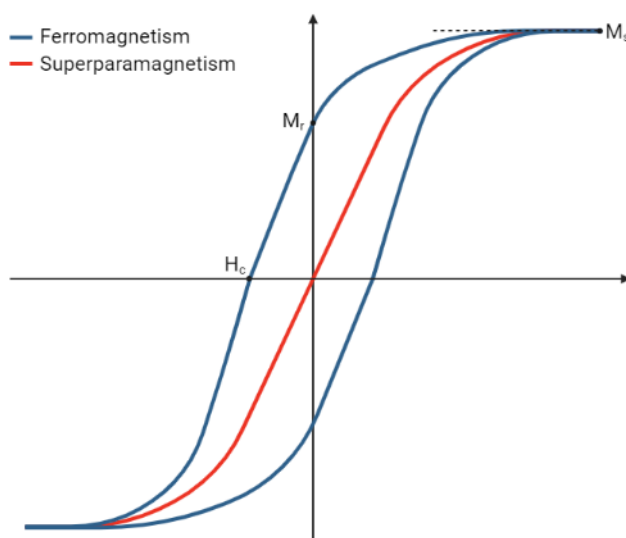
Figure 4. Graphical representation of the magnetic response of a **(A)** magnetic material and **(B)** a superparamagnetic nanoparticle (a sigmoidal curve). Created with Biorender.com.

In the presence of an external magnetic field, the nanoparticles can rotate their magnetic moments to align with the external field applied – Néel relaxation[85,86]; or they can rotate as a whole – Brownian relaxation[86]. These rotations are easily comprehended by **Figure 5**. This loss process is a very complex process, affected by size, size distribution, shape, chemical composition, surface modifications, magnetic saturation, environment, amplitude and frequency of the applied AMF – these last two technical factors can be used to optimize these losses[86]. In magnetic hyperthermia treatment, it is important for the nanoparticles to have an adequate size and size distribution, low toxicity, and a high saturation moment to minimize application doses.

It is advised to use minimal amounts of NPs to diminish potential off-target toxic effects in hyperthermia applications[87]. Thus, the heat efficiency of the nanoparticles needs to be optimised. Currently, this optimization in the generation of thermal energy is dependent on the type of material - which is commonly iron oxide because of its biocompatibility and easy synthesis -, as well as the applied frequency and the size and anisotropy of the nanoparticles[88]. It is critical to control the

outcome of the hyperthermia stimulation by an external AMF, so that in *in vitro* and *in vivo* scenarios the cellular integrity is not compromised.
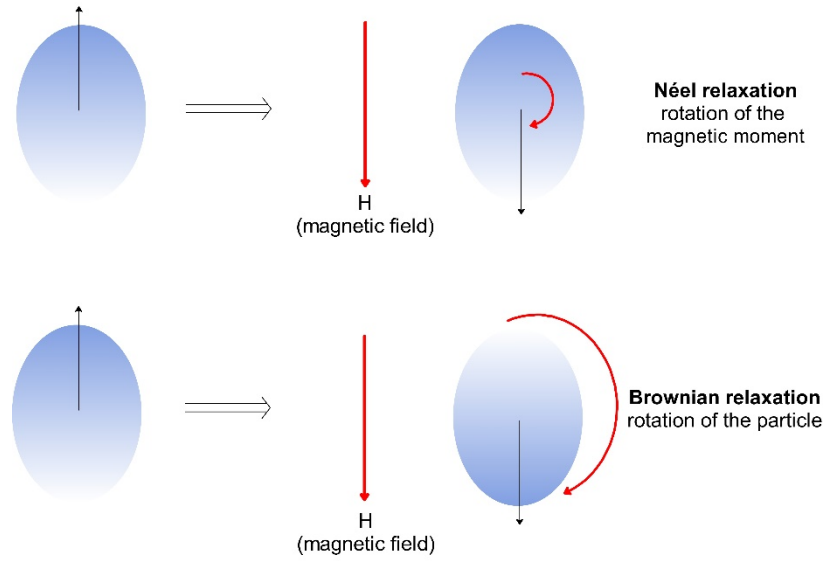
Figure 5. Néel and Brownian relaxation behaviour through the application of an external magnetic field.

The specific heat absorption rate (SAR) or the intrinsic loss power (ILP) parameters help evaluate the magnetic heating efficiency of magnetic nanoparticles. They can be determined by calorimetric methods like heat quantification, the measurement of the heat evolution with time which is a straightforward technique. All that is in the sample affects these measurements and so, thermal properties and geometric characteristics must be accounted for, as they are in **equation (1)** and **equation (2)**:

$$SAR = \frac{C}{m_{Fe}} \frac{\Delta T}{\Delta t} \ (W.g^{-1}) \tag{1}$$

$$ILP = \frac{SAR}{H^2 * f} \ (W.(g.kHz)^{-1}.mT^{-2}) \tag{2}$$

where C is the volumetric specific heat capacity of the solution (J.(g.K)$^{-1}$), m_{Fe} is the mass concentration of the magnetic element in the solution (g.mL^{-1}), $\frac{\Delta T}{\Delta t}$ is the initial slope of the temperature-versus-time exponential curve (K.s^{-1}), H is the field (mT), and f is the frequency the alternating magnetic field (kHz). SAR is directly related to energy losses of the magnetic nanoparticles when under an alternating current field[87]. So does the ILP, but in this case in a way independent of the field and frequency used for the measurement.

3.4.2. *Magnetic Resonance Imaging*

Magnetic Resonance Imaging is a non-invasive, non-ionizing, *in vivo* imaging modality that produces detailed three dimensional anatomically accurate images[89,90]. MRI takes advantage of the nuclear properties of water protons, for instance the nuclear spin. After exposure to an external

13

magnetic field, the magnetic moments with the water protons are aligned. Then, a radio frequency is employed, energizing the nuclei – the magnetic moment of the nuclear spin of the water protons are "flipped" form the longitudinal plane to the transversal plane[90–92]. The relaxation time, the time in which the signal returns to equilibrium, depends on two relaxation processes that are independent: the longitudinal relaxation (T_1) process that consists of the realignment to the external magnetic field, and the transverse relaxation (spin-spin relaxation, T_2) that consists of the dephasing of the processing spins[92]. Both relaxation times are dependent on the macromolecular environments, and so, their magnetic dipole moments act as probes sensitive to their environment[91]. An alternating current in a receiver coil is induced, measured, and reconstructed into 3D images[90,91] - high quality cross-sectional images of the body in any plane are created, using externally controlled magnetic fields[93]. This makes it possible to reliably detect a wide range of pathological illnesses, such as cancer, heart disease, and musculoskeletal issues.

However, the signal-to-background ratio of MRI is extremely low due to the large amount of water protons[94]. Contrast agents can increase contrast between tissues, helping in the diagnostic of said pathologies. The spin relaxation time of water protons is altered: superparamagnetic nanoparticles can flip the orientation of water protons within their environment with very high relaxivity values[95]. The provoked disturbances in the magnetic field result in a detectable change in the resulting signal.

Currently, gadolinium-enhanced MRI techniques are the standard. However, gadolinium-based contrast agents have been shown to have inadequate specificity for chronic infections, due to its inability to be taken up by macrophages[96]. SPION-based contrast agents, are taken up by macrophages in inflamed tissues, resulting in a higher MRI contrast[96]. Generally, SPIONs are used as a T_2-weighted contrast agent as they can reduce the spin-spin relaxation (T_2) time aiding to generate contrast.

The magnetite NPs when located in the target tissue can induce a local field inhomogeneity (**Figure 6**), causing negative contrast by shortening the T_2 relaxation time of water protons[95]. This effect displays as dark (hypointense) domains in MR images, as the T_2 of the water is shortened[97]. Magnetite NPs (depending on their size and M_s) sometimes can also generate T_1 contrast for biomedical applications. Besides SPIONs exhibiting good biocompatibility, the amount of contrast agent needed for injection (0.5 mg.kg^{-1}) is similar to the body daily requirement of iron[98].

The contrast properties of MNPs can aid in the spatial control of a formulation in *in vivo* applications. Real-time MRI can be an advantageous technique, since it allows to examine MNPs

biodistribution, assuring that the MNPs are in the pathological tissue (may it be for diagnostic, therapy or both intentions).
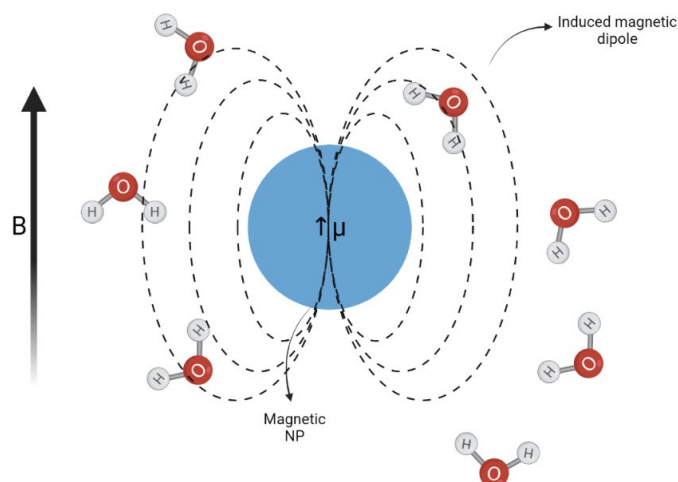
Figure 6. Fundamentals of MRI: concept of nuclear resonance principle.

3.5. Magnetic Nanoparticles challenges

SPIONs present a high surface to volume ratio, which promotes interactions with body components, thus potentially increasing their toxicity. Their capability to cross body barriers[99] and their resistance to degradation also play a potential role in the toxicity of the nanoparticles[72]. Although they have been approved to use in the clinic, several reports[100–102] have shown some potential underlying toxicity of these nanoparticles. Not only size and high surface to volume ratio are involved in this potential toxicity, but the administration route, chemical composition, immunogenicity, degradation and elimination pathway from the body might also play a role.

Even though superparamagnetic nanoparticles seem ideal at first glance for a wide range of biomedical applications, as they are made of different materials from the organic biomolecules that compose the body[48], they are actively cleared by reticuloendothelial system cells that are responsible for the innate immune responses[63]. Additionally, since nanoparticles have a high volume-surface ratio, they tend to suffer opsonization (they absorb plasma proteins), making them easily recognizable by macrophages[62]. To remain in the body, nanoparticles in general have a size constriction: below 10 nm in size, NP are filtrated and rapidly secreted by the kidneys[103]; above 200 nm they are cleared in the liver and spleen[62]. Having a negatively or neutral charged surface can also lead to higher circulation times[62].

Given that the conventional approach for bulk synthesis of magnetite nanoparticles relies on uncontrolled factors such as magnetite oxidation to maghemite[104] or mixing and nucleation parameters that are not well controlled[105], the synthesis of reproducible and biomedically safe

nanoparticles still needs optimization and exploring, in order to make nanobiotechnology prosperous for biomedical applications. This consistency issues have been a target of study: it challenges their application and the comprehension of the methodology. In any case, characterization of the nanoparticles by various techniques becomes fundamental in the study of the product, providing insights of what might be their future behaviour, *in vitro* and *in vivo*.

3.6. Methods and approaches of synthesis

The synthetic process of nanoparticles affects their physical and chemical characteristics. Nucleation, growth, aggregation and impurities adsorption are some of the factors influencing the morphology of iron oxide nanoparticles[106]. Synthesis conditions can help control the outcome[48]. Biomedical applications of nanoparticles *in vivo* require a narrow size distribution, physiologically stable NPs, biocompatibility, and of course their own suitable magnetic properties[48]. As in this Thesis the nanoparticles will be used for heat production it is ideal that their size is controllable and preferably with a small distribution in size: this will allow for a better outcome in magnetic hyperthermia. Obtaining a large quantity of magnetic nanoparticles with a simple and easy protocol is also a factor. Because of this premise, a novel challenge arises on the attempt to synthetise magnetite nanoparticles with a controlled size. There are different methods of synthesis that can be employed.

The nucleation and growth theory describes the formation of crystalline materials via spontaneous formation of nuclei[107], which depend on supersaturation[108]. Crystal growth of nanoparticles during synthesis is achieved by a process called nucleation. This process can be thermodynamically explained: the total free energy of a nanoparticle combines the sum of the surface free energy and the bulk free energy[109]. Even more, there is a maximum free energy for the formation of a stable nucleus, and for that reason, there is also a critical radius of the nanoparticles, so they don't redissolve in solution[109]. After nucleation, crystals grow sequentially or simultaneously causing increasing sizes[108].

The co-precipitation method of nanoparticle synthesis is an efficient soft chemical route that involves dissolving of the starting materials (iron salts) and adding a precipitating agent, forming a single phase inorganic solid[110], by taking advantage of the different solubility of salts in the water[111]. This is a simple method that results in large amounts of nanoparticles with high purity[112], but, nonetheless, these show poor crystallinity as well as a poor size control and size distribution control.

The thermal decomposition is a wet chemistry method of nanoparticles synthesis that make use of an endothermic chemical decomposition. Heat is a source of energy used to break down the chemical bonds of the iron precursors (organometallic compounds), allowing the controlled preparation of magnetite to take place[113,114]. This method offers stable monodispersed nanoparticles (great size and size distribution control) with controllable shape[115] and high crystallinity[116], but the resulting particles are typically soluble only in non-polar solvents[117]. The reactions that occur in this process are actually complex[118] and they present a relatively low production rate[119].

The hydrothermal method exhibits high yields[120], large production amounts, good crystallinity[113,120,121] and good quality. Moreover, it easily provides a solution of controllable and well-defined size nanoparticles and better morphological control than other techniques, besides being relatively simple and cost-effective[120,122]. This method has the highest efficiency in nanocrystals synthesis since it exploits the solubility of some inorganic substances[122] and there is no need to heat the sample after treatment (thus avoiding of particle agglomeration)[120]. The growth conditions influence the crystal morphology[123].

4. A new system in theranostic

Genetic amplification is a field of study still in development, tolerant to new hypotheses as noted before. The limitations of current methodologies as well as the rising in the issues of genetic nature call for other alternatives. As the targets of genetic disorders may differ extensively in their nature and treatments, a versatile system that could overcome most challenges and be the answer to the previous deepening concerns would be a powerful tool. Nanoparticles' flexible design is an adjuvant in their various applications and can also be in gene therapy. Becoming a vector themselves - by acting as nanovehicles that can deliver genetic material (such as primers and even *Taq* polymerase in this case) - or indirectly leading to the amplification of genetic material, makes this a new proposed nanosystem. Combining their magnetic abilities (e.g. hyperthermia through the application of an external AMF and imaging capabilities as contrast agents) and their purpose as a nanovehicle (through functionalization of these molecules on the surface via peptide coupling reaction) this new system could be controlled, temporal and spatially, to amplify a target region of DNA. Thus, the conjugation of magnetite nanoparticles properties under AMF (heat generation) and the *Taq* polymerase activity in a PCR reaction is proposed as a new genetic amplification system. This work will be developed and tested in bacteria, as they have no nuclear membrane,

which translates in easier access to genetic material. JM109 cells (*Escherichia coli*) will be used as they are simple organisms, with fast cell division and easy manipulation. The aim of this project is demonstrating the proof-of-concept of a new theranostic system (**Figure 7**).
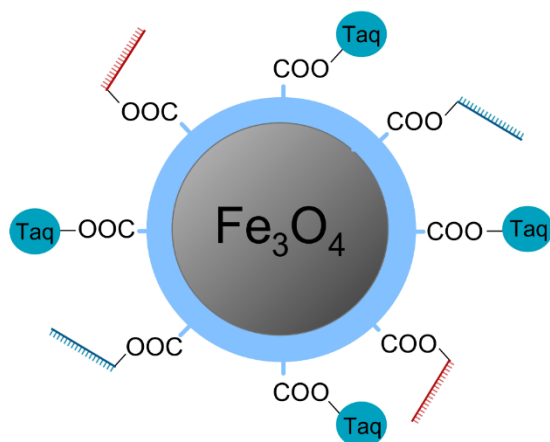
Figure 7. Illustration of a superparamagnetic magnetite nanoparticle coated in polyacrylic acid and functionalized with *Taq* polymerase and EGFP primers (red and blue). Created with Biorender.com.

First, polyacrylic acid coated magnetite nanoparticles will be synthesised in the desired shape and size that are optimal for the magnetic hyperthermia applications. The principal goal of this phase is to obtain large quantities of well-rounded nanoparticles with a magnetic inorganic core close to 16 nm, high crystallinity, and good quality. In this work the hydrothermal method for nanoparticles synthesis was chosen due to its advantages.

Furthermore, a ligand molecule named capping agent, can be introduced in the synthesis reaction[124]. Polar groups are able to form stable bonds with the metal atoms or ions, as it contains functional groups with donor atoms (nitrogen, oxygen, sulphur or phosphate)[124]. These molecules inhibit the over-growth of nanoparticles, control their agglomeration as well as their physico-chemical characteristics[125] – which is why it is a necessity for biomedical applications. As a capping agent, polyacrylic acid (PAA), allows the stabilization of the magnetite nanoparticles[126] and increases their shelf-life by providing electrostatic and steric repulsion against particle aggregation[127,128]. In PAA, every two carbon atoms of the main chain there is a carboxylic group (as shown in **Figure 8**) and, when those are deprotonated, PAA presents a high negative charge density[129]. It is adsorbed on the surface of the magnetite NPs through a chemical bond, where carboxylic groups (-COOH) coordinate strongly to Fe^{3+} (from Fe_3O_4 crystal surface), leaving extra uncoordinated carboxylate groups spread onto the water (the used dispersion medium). This allows for high water dispersibility and serves as an efficient carrier for biomolecules[127], being capable of forming flexible polymer chain-protein complexes[130].
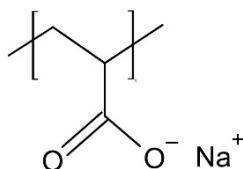
Figure 8. Poly(acrylic acid) chemical structure.

The different reaction parameters of the hydrothermal synthesis of magnetite can affect the final nanoparticle size. As the ferrous/ferric ions molar ratio increases, the particle size and crystallinity of magnetite nanoparticles also increases[131]; if the reaction time increases, so does the nanoparticle size[132]; if the concentration of PAA is increased, the nanoparticle size increases[133,134]; increasing reaction temperature has the same outcome as well[132], since the temperature at which the hydrothermal synthesis of the nanoparticles is executed plays a fundamental role in achieving single-phase nanocrystals[135].

The physical, chemical, and functional characterization of the nanoparticles will confirm their properties. Characterization techniques as dynamic light scattering, ultraviolet-visible spectroscopy, transmission electron microscopy, thermogravimetric analysis, superconducting quantum interference device, X-ray diffraction, magnetic resonance imaging, magnetic hyperthermia, Fourier transform infra-red spectroscopy, fluorescent spectroscopy, and others will be executed to obtain a fully characterized and more predictable sample.

In this Thesis JM109 cells, an *Escherichia coli* strain, were used for plasmid expansion and its posterior extraction. The selected plasmid for this work (pCMV-GFP) is illustrated in **Figure 9**. Its vector backbone is pCAGE, and it is constructed with an ampicillin resistant gene and with the Enhanced Green Fluorescent Protein (EGFP), detailed in light green and fluorescent green, respectively. The sequence of this plasmid is detailed in **Annex 1**. The target of amplification is the GFP gene, named EGFP (fluorescent green) in **Figure 9**.

Through the functionalization of the nanoparticles via EDC (1-ethyl-3-(3-dimethylaminopropyl)) and sulfo-NHS (N-hydroxysulfosuccinimide sodium salt) coupling, a stable covalent functionalization will be formed with the following ligands: *Taq* polymerase and modified primers to obtain the final theranostic system. The functionalization of primers onto the surface of the magnetite nanoparticles in the 5' end of both forward and reverse primers was enabled by the presence of 5'end amino link C_{12} modifications. This modification is composed of an amino group followed by a 12-carbon spacer arm, which allows for future coupling reactions. Each of these
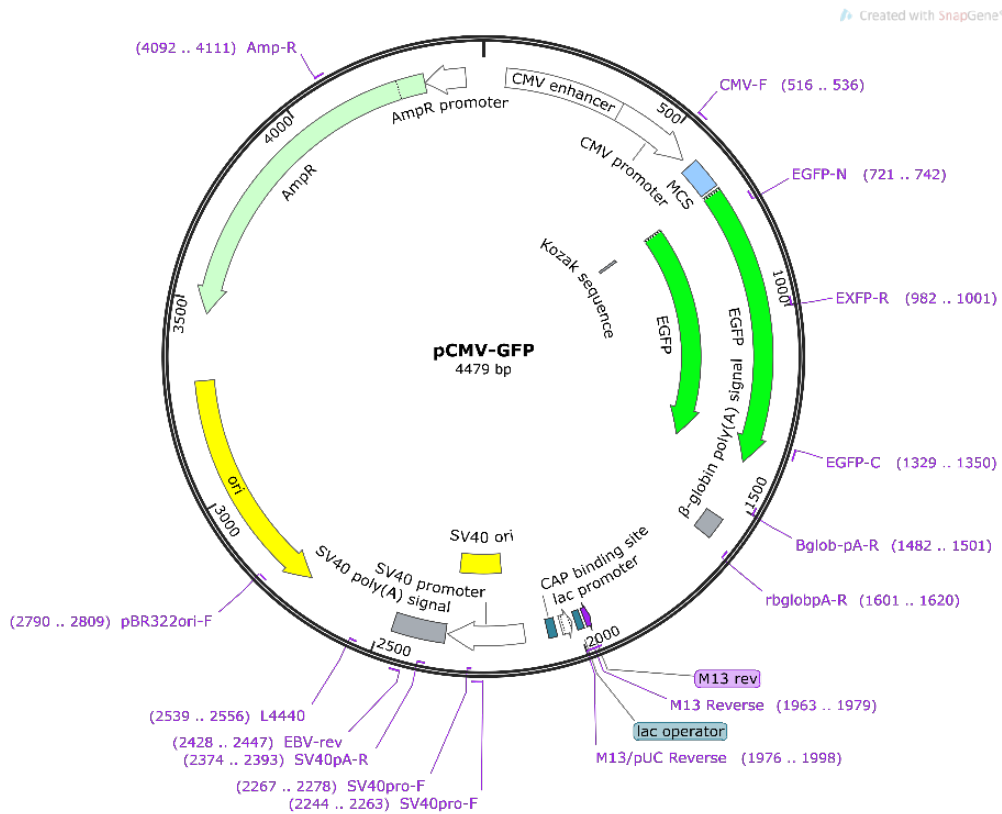
Figure 9. Map of the plasmid DNA (pCMV-GFP vector). Created with SnapGene®.

systems will also be physically, chemically, and functionally characterized in the techniques that seem fit.

Viability and toxicity studies will be performed on *Escherichia coli* to prove that magnetic nanoparticles and their ability to generate heat do not lead to cell death. Simultaneously, the PCR process will be optimized. Assays on the influence of the coupling of *Taq* polymerase to nanoparticles on the activity of the enzyme will be conducted. PCR experiments using the magnetic hyperthermia capability of the synthetised magnetite nanoparticles will be performed to assess the veracity of this Thesis proof-of-concept. The hyperthermia process will be controlled externally through an alternating magnetic field. In this application, it is not the aim to induce macroscopic temperature increase of the nanoparticle's solutions, but to induce a very local 'nanoscopic' temperature increase on the surface of the nanoparticles, which will directly affect the enzyme and primers. Finally, experiments in *Escherichia coli* bacteria will be performed to apply this new concept.

This is a completely new field with promising potential in the biomedical field, as this work can revolutionize the approach to gene amplification and how it can be perceived, as well as performed and externally controlled. The ability to perform on-demand genetic amplification locally

with external control of the process is an ideal practice for treatment (and imaging) of genetic diseases as well as cancer.

CHAPTER TWO:

MATERIALS AND METHODS

CHAPTER TWO: MATERIALS AND METHODS

1. Materials

In this section, the equipment, software, materials, and reagents/solutions required for the development of this Thesis are listed below with its corresponding manufacturer (when applied).

Table 1. List of used equipment, software, materials, and reagents/solutions.

EQUIPMENT

- Centrifuge 5810R - Eppendorf
- Centrifuge minispin - Eppendorf
- Dynamic Light Scattering – Zeta potential - SZ-100Z – Horiba Scientific
- Electrophoresis System - BioRad
- FluoMax-4 Spectrofluorometer SOP - HORIBA
- Fluorescence plate reader - SYNERGY H1 - Biotek
- Fourier Transform Infrared Spectroscopy – Vertex 80v – Bruker
- Gel Imaging System - GelDocTM EZ - BioRad
- Inductive Plasma Atomic Emission Spectrometer - ICPE 9000 - SHIMADZU
- Magnetic Hyperthermia equipment – DM1 - nanoScale Biomagnetics
- MR solutions 3.0 Tesla benchtop magnetic resonance imaging system
- NanoDrop™ 2000c Spectrophometer – Thermo Fisher Scientific
- Orbital Incubator - Fisher Scientific
- Oven VENTI-Line®- VL115 – VWR
- pH meter - Seven Compact pH/Ion meter - Mettler Toledo
- Precision balance – ABT 120-5DM – KERN
- Superconducting Quantum Interference Device – Vibrating Sample Measurement – MPMS - Quantum Design
- Thermal Cycler - Veriti 96-well - Veriti®
- Thermogravimetric Analyser – TGA/DSC 1/1100 SF STARe System - Mettler Toledo
- Transmission Electron Microscope – JEOL JEM 2100 200 kV (Cryo & Tomography) - JEOL
- UV-Vis SpectroPhotoMeter - UV-2550 – SHIMADZU corporation
- Vertical autoclave - 3870ELV - Tuttnauer
- Vortex – VV3 - VWR

- X-Ray Diffraction System – X PERT PRO MRD – PANalytical

SOFTWARES

- GIMP 2

- GraphPad Prism 8.0.4

- Image J

- Microsoft Office 365

- Origin 9.0

- ApE

- SnapGene Viewer 6.0.5

- OligoAnalyzer™

- Primer3web (version 4.1.0)

MATERIALS

- 0.22 μm PES syringe filters - Branchia®

- GRS Plasmid Purification Kit – GriSP®

- Inoculating Loops and Needles - VWR®

- NucleoSpin® Gel and PCR Clean-Up Kit – Macherey-Nagel®

- Pur-A-Lyzer™ Midi Dialysis Kit - Midi 6000, MECO 6-8KDa – Sigma-Aldrich®

- QIA prep® Spin Miniprep Kit - Qiagen®

- QIAGEN Plasmid Giga Kit - Qiagen®

- Sterile plastic 90 mm plates

- Vivaspin 500, 100 000 MWCO PES – Satorius

- Zippy Plasmid Miniprep Kit – Zymo®

REAGENTS/SOLUTIONS

- 1-ethyl-3-(3-dimethylaminopropyl) carbodiimide hydrochloride - Sigma-Aldrich®

- 5x Green Go *Taq*® Reaction Buffer - Promega

- Acetone - Honeywell

- Ammonia solution 30% AGR – labkem

- Ampicillin Trihydrate - TCI

- Bovine Serum Albumin - Sigma-Aldrich®

- EGFP primers (no modification) – Eurogentec

- EGFP primers with amino link C_{12} modiication - Sigma-Aldrich®

- Ethylenediaminetetraacetic acid disodium salt dihydrate - Sigma-Aldrich®

- *Fluorescein cadaverine* – Biotium

- GeneRuler 1 kb Plus DNA Ladder - Sigma-Aldrich®

- Go*Taq*® DNA Polymerase - Promega

- Hydrochloric acid 37 % - Fisher Scientific®

- Iron (II) chloride tetrahydrate - Sigma-Aldrich®

- Iron (III) chloride hexahydrate - Sigma-Aldrich®

- LB agar (Miller) - Sigma-Aldrich®

- LB medium (Luria Bertani) - Liofilchem®

- LB medium (Miller) - VWR®

- Milli-Q water (ultra-pure)

- N-hydroxysulfosuccinimide sodium salt - Sigma-Aldrich®

- pCMV-GFP – AddGene®

- PCR Nucleotide Mix - Promega

- Phosphate Buffer Solution, ph 7.4

- Poly (acrylic acid sodium salt) - Sigma-Aldrich®

- Sodium chloride 99.5% - Sigma-Aldrich®

- SYBR Safe™ DNA Gel Stain – Invitrogen™

2. General procedures

The methods used for the development of this work, are detailly described in this section. Assays, kits, and others are also mentioned with preferred procedures.

2.1. Synthesis of magnetite nanoparticles

The magnetite nanoparticles in this project were synthesised by hydrothermal synthesis, following the reaction represented in **Figure 10**.
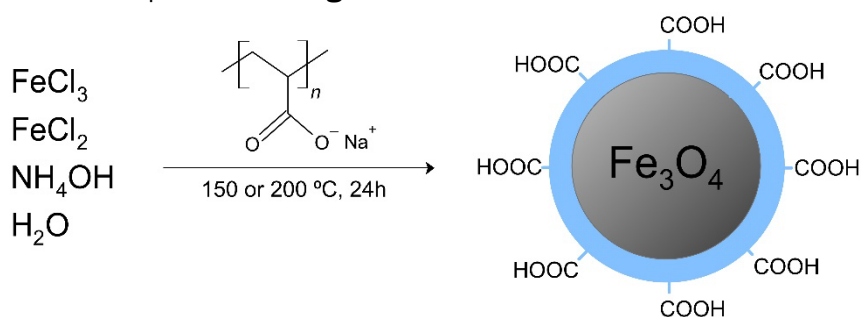
Figure 10. Schematic illustration of the hydrothermal synthesis reaction of magnetite nanoparticles.

FeCl$_3$.6H$_2$O (1.59 g, 8x10^{-4} mol, 1 equiv) and FeCl$_2$.4H$_2$O (3.78 g, 1.4x10^{-3} mol, 1.75 equiv) powders were weighted and diluted in 7 mL of milli-Q water in a 40 mL polytetrafluoroethylene (PTFE) vessel. A solution of ammonium hydroxide (15 mL of 28 to 30%, 480.5 equiv) was added to this solution. This was immediately followed by the addition of a sodium polyacrylate (PAANa) solution (5 mL) in milli-Q water, which resulted in a dark coloured precipitate of Fe$_3$O$_4$. The autoclave reactor was closed and then placed in an oven at for 24h. Four different formulations were assembled: their differences are highlighted in **Table 2.**

Table 2. Differences between the four different PAA coated magnetite nanoparticles formulations.

Formulation	PAANa	PAANa addition	Oven temperature (°C)
Fe$_3$O$_4$@PAA (I)	1 g, 2x10^{-4} mol, 0.25 equiv	Immediately after NH$_4$OH	200
Fe$_3$O$_4$@PAA (II)	2 g, 4x10^{-4} mol, 0.5 equiv	After NH$_4$OH	150
Fe$_3$O$_4$@PAA (III)	2 g, 4x10^{-4} mol, 0.5 equiv	Immediately after NH$_4$OH	200
Fe$_3$O$_4$@PAA (IV)	4 g, 8x10^{-4} mol, 1 equiv	Immediately after NH$_4$OH	200

The following day, the autoclave was allowed to cool down and the particles were diluted down with acetone and centrifuged at 4000 rpm for 10 min. The pellet was resuspended with water and this solution was centrifuged at 9000 rpm for 1.5 h. The supernatant was discarded, and this purification procedure was repeated as needed. The pellet was resuspended in water, the solution centrifuged at 3000 rpm for 5 minutes and its supernatant constitutes the final solution (Fe$_3$O$_4$@PAA) - which was kept stored in water at 4 °C.

Before use, these nanoparticles were purified by diluting a chosen volume in acetone and centrifuging at 4000 rpm from 90 seconds to 3 minutes. Finally, the pellet was resuspended in water.

2.2. Magnetite nanoparticles functionalization

1-ethyl-3-(3-dimethylaminopropyl) carbodiimide hydrochloride (EDC) catalyses the formation of amide bonds between carboxy and amine bonds[136], so when in contact with the carboxylic groups of PAA forms an unstable reactive O acylisourea ester. N-hydroxy sulfosuccinimide (sulfo-NHS) increases the stability of the active intermediate in these coupling reactions by forming an active ester functional group with carboxylates[136]. Finally, the addition of the ligand with amine groups leads to the formation of a stable amide bond between the ligand

and the carboxylate groups. This reaction, represented in **Figure 11**, is named EDC/sulfo-NHS coupling and allows for PAA coated nanoparticles to be covalently functionalized. Magnetite nanoparticles were functionalized with *fluorescein cadaverine*, Bovine Albumin Serum (BSA), *Taq* polymerase and specific primers of the chosen GFP gene through the duration of this dissertation.
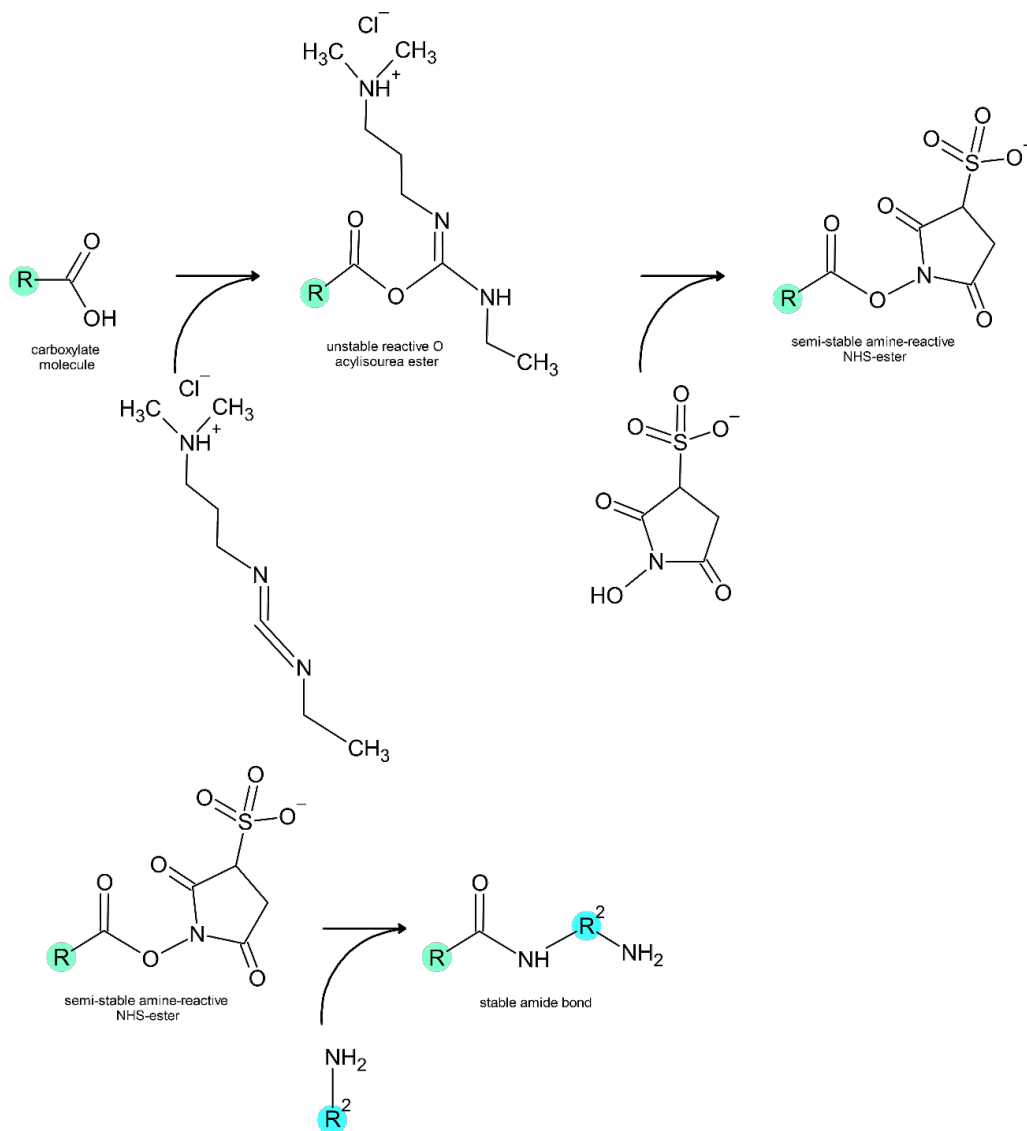
Figure 11. Mechanism of EDC/sulfo-NHS coupling reaction.

2.2.1. Fluorescein cadaverine assay

The determination of the number of available carboxylic groups on the surface of the nanoparticles was achieved through the *fluorescein cadaverine* functionalization, represented in **Figure 12**. First, 16.35 µL of Fe_3O_4@PAA (III) nanoparticles (415 mM) were centrifuged with 500 µL of acetone and the pellet resuspended with milli-Q water. Nine reactions were performed simultaneously varying the concentration of magnetite nanoparticles while maintaining the *fluorescein cadaverine* concentration (0.25 mM). An EDC and sulfo-NHS solution and a *fluorescein cadaverine* solution were prepared with concentrations of **2.3 mM**, **2.3 mM**, and **1.390 mM**,

27

respectively. The magnetite nanoparticles were resuspended in the milli-Q water and the EDC/sulfo-NHS solution was added. The samples were stirred at 500 rpm for 30 minutes. Then, *fluorescein cadaverine* was added to the different reactions, which were further stirred for one day at 500 rpm. All the concentrations are listed in **Table 3**.
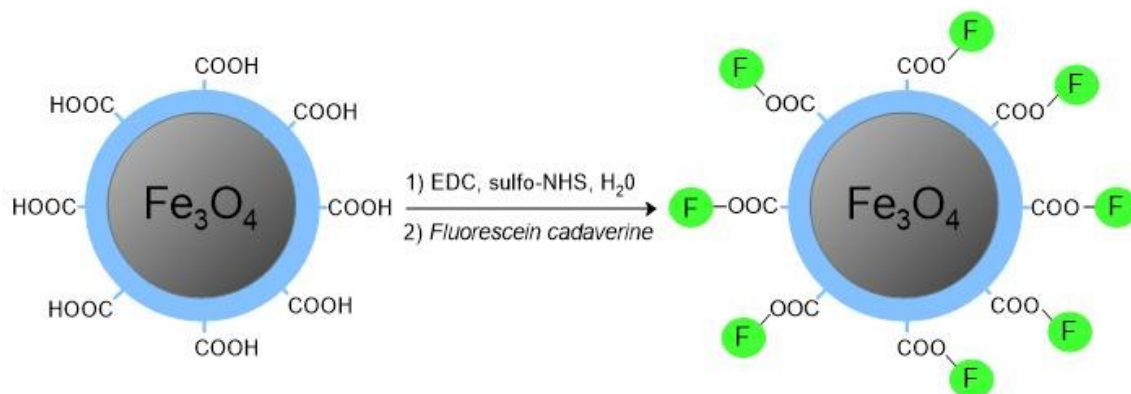
Figure 12. Schematic illustration of the coupling reaction of the carboxylic groups of the polyacrylic acid coating the magnetite nanoparticles to *fluorescein cadaverine*.

Table 3. Registration of concentration of different components on the coupling reactions of *fluorescein* cadaverine with Fe$_3$O$_4$@PAA nanoparticles.

Reaction	1	2	3	4	5	6	7	8	9
Fe$_3$O$_4$@PAA (mM)	3.86×10^{-5}	1.86×10^{-4}	2.80×10^{-4}	3.73×10^{-4}	5.59×10^{-4}	7.46×10^{-4}	9.32×10^{-4}	1.12×10^{-4}	1.86×10^{-3}
EDC/sulfo-NHS (mM)					0.33 and 0.33				
fluorescein cadaverine (mM)					0.25				

The different suspensions were centrifuged at 13 400 rpm for 30 min to induce nanoparticle precipitation. The supernatant, composed by water, EDC, sulfo-NHS, and the uncoupled *fluorescein cadaverine*, was recovered. Then, it was diluted in Phosphate Buffered Saline (PBS) pH 7.4 (dilution of 1:10). Ultraviolet-visible spectrum from 200 to 900 nm was obtained for *fluorescein cadaverine* standards and sample measurements: the wavelength of 481 nm (peak of absorbance) was employed for *fluorescein cadaverine* quantification.

2.2.2. *Bovine Serum Albumin functionalization*

The optimization of protein functionalization onto the surface of the magnetite nanoparticles started with the functionalization with BSA, represented in **Figure 13**. The goal for this functionalization was to obtain a ratio of three BSA proteins per one nanoparticle. First, Fe$_3$O$_4$@PAA (III) nanoparticles (100 µL, 1 equiv) were centrifuged with 500 µL of acetone and the pellet resuspended with milli-Q water. An EDC and sulfo-NHS solution and a bovine serum albumin

(BSA) solution were prepared with concentrations of 2.44 mM, 2.44 mM and 64.73 µM, respectively. The magnetite nanoparticles were resuspended in milli-Q water and EDC and sulfo-NHS (264 µL, 0.45 equiv) were added. The sample was stirred at 500 rpm for 30 minutes before adding the BSA solution (969 µL, 0.04 equiv). The reaction was stirred for three days at 500 rpm.
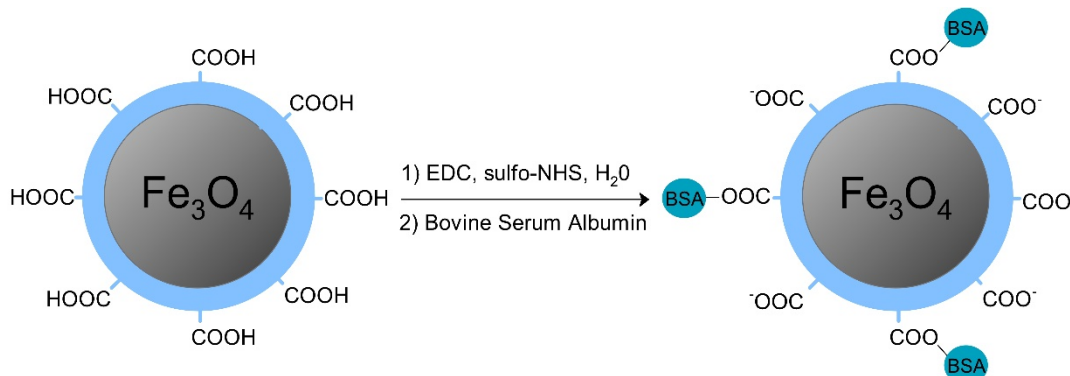
Figure 13. Schematic illustration of the coupling reaction of the carboxylic groups of the polyacrylic acid coating the magnetite nanoparticles to Bovine Serum Albumin (BSA).

The suspension was centrifuged at 7000 rpm for 10 minutes using Vivaspin® 500 with 100 000 MWCO (Molecular Weight Cut-Off) PES (polyether sulfone) membrane, as to separate the nanoparticles from the rest of the suspension. This solution, composed of water, EDC, sulfo-NHS and the uncoupled BSA protein, was recovered. Dialysis was then carried out as specified in section **2.3** and the uncoupled protein quantification was done as described in section **2.4**.

2.2.3. *Taq polymerase functionalization*

The functionalization of *Taq* polymerase was carried out similarly to the BSA functionalization, as represented in **Figure 14**. The goal for this functionalization was to obtain a ratio of three *Taq* polymerase proteins per one nanoparticle, and for *Taq* to retain its functionality after the functionalization. First, Fe$_3$O$_4$@PAA nanoparticles (0.578 µL, 1 equiv) were centrifuged with 500 µL of acetone and the pellet resuspended with milli-Q water. An EDC and sulfo-NHS solution was prepared at a concentration of 2.3 mM each, and 10 µL of a Go*Taq*® DNA

Figure 14. Schematic illustration of the coupling reaction of the carboxylic groups of the polyacrylic acid coating the magnetite nanoparticles to *Taq* polymerase.

Polymerase solution from Promega® was used. The magnetite nanoparticles were resuspended in 498 μL of milli-Q water and the EDC/sulfo-NHS solution (2 μL, 0.45 equiv) was added. The suspensions were stirred at 500 rpm for 30 minutes and centrifuged at 13 400 rpm for 10 minutes. The protein *Taq* polymerase (10 μL, 0.04 equiv) was added, and the reaction was stirred for one day at 500 rpm.

The suspension was centrifuged at 13 4000 rpm for 10 minutes, to precipitate the nanoparticles from the rest of the suspension. This solution, composed of water, EDC, sulfo-NHS and the uncoupled *Taq* polymerase, was recovered. Then, dialysis was carried out as specified in section **2.3** and the uncoupled protein quantification was carried out as in section **2.4**. The pellet, composed by Fe_3O_4@PAA-*Taq*, was resuspended in 20 μL of PBS pH 7.0 and stored at -20 °C until further use.

2.2.4. Primer's functionalization

Initially, the EGFP-F and EGFP-R primers functionalization was attempted separately onto Fe_3O_4@PAA surface. First, Fe_3O_4@PAA nanoparticles (0.5 μL, 1 equiv) were centrifuged with 1000 μL of acetone at 13 400 rpm for 10 minutes. The pellet was resuspended with 495 μL of nuclease free milli-Q water. An EDC and sulfo-NHS solution was prepared with concentrations of 2.3 mM and 2.3 mM, respectively, and EGFP-F (1.023×10^{-3} M) and EGFP-R (1.034×10^{-3} M) solutions were prepared. To the resuspended magnetite nanoparticles were added the EDC/sulfo-NHS solution (2.31 μL, 0.75 equiv), and the suspension was stirred at 500 rpm for 30 minutes. Then, the EGFP-F (2.60 μL, 0.37 equiv) or EGFP-R (2.57 μL, 0.37 equiv) primers were added to the reaction and stirred for one day at 500 rpm.

After one day, the suspension was centrifuged at 13 400 rpm for 30 minutes and the supernatant was taken out for primer quantification. Dialysis with Slide-A-Lyzer Mini Dialysis Devices, 3.5 K MWCO, 0.5 mL was performed as specified in section **2.3**. Primer quantification is possible by UV-Vis at 260 nm or by Nanodrop. Pellet was resuspended in 5 μL of PBS pH 7.0 and kept stored at -20 °C.

All attempts at primer functionalization are further detailed in **Annex 2, Table 12**.

2.3. Dialysis kit

After EDC/NHS coupling reactions, separating the functionalized nanoparticles from the leftover EDC and sulfo-NHS was essential to quantify the yield of the reaction, as EDC and sulfo-NHS interfere with the protein quantification (detailed in section **2.4**). For this application, Pur-A-

Lyzer™ Midi Dialysis Kits from Sigma-Aldrich®, with a MWCO of 6 to 8 KDa and a capacity of 50 to 800 µL; and Slide-A-Lyzer® Mini Dialysis Devices, 3.5 K MWCO, 0.5 mL from Thermo Scientific™, with a capacity of 5 to 500 µL, were used.

The Pur-A-Lyzer was filled with 800 µL of milli-Q water and incubated for at least 5 minutes. The tube was emptied and then loaded with the sample. The tube was closed with the provided caps and placed in the floating rack. This floating rack was then placed in a stirred beaker containing a large volume of the buffer (100 to 1000-fold of the sample volume) and left overnight. The sample was carefully pipetted to a clean tube and the retrieved volume was measured.

The Slide-A-Lyzer was filled with 1000 µL of nuclease-free milli-Q water and incubated for at least 5 minutes. The mini device was emptied and immediately loaded with the sample. The device was placed in the tube with 14 mL of the used buffer, nuclease-free water. The buffer was exchanged at hour 2 and 4. The sample was left overnight, which then was carefully pipetted to a clean tube, and the retrieved volume was measured.

The Vivaspin 500 device with a 100 000 MWCO PES membrane was filled with 500 µL of the sample. The device was placed in the microcentrifuge for 10 min at 7 000 rpm. The flow-through (uncoupled primers) was quantified. The remaining sample was carefully pipetted to a clean tube (retrieved volume was measured) and kept at -20 ºC until use.

2.4. Bradford protein assay

The quantification of protein was essential to follow the progression of the reactions and their outcome. In this project, to quantify BSA or *Taq* polymerase, a Micro BCA™ Protein Assay Kit from Thermo Scientific™ corporation was used, a colorimetric method that exhibits very low levels of protein-to-protein variability. In a 96-well plate, the samples, as well as standard points with different concentrations of BSA, were mixed with equal volumes of working reagent (25 parts Micro-BCA reagent A, 24 parts Micro-BCA reagent B and 1 part Micro BCA reagent C) – total volume of 300 µL. The absorbance was measured at 562 nm with BioTek Synergy H1 equipment and was directly related to BSA concentration through a linear calibration curve.

2.5. Physico-chemical characterization techniques

2.5.1. Ultraviolet-Visible spectrophotometry

UV-Vis (ultraviolet-visible) spectrophotometry is a quantitative analytical technique that allows the measurement of radiation absorption in the UV-Vis spectrum region (between 180-780

nm). Additionally, there is a linear relationship between the absorbance (A) of the solute and its concentration (c) – ideal for quantitative measurements[137]. This correlation is expressed by the Beer-Lambert Law[138], articulated in **equation (3)**:

$$A = \varepsilon lc \qquad\qquad\qquad (3)$$

where A represents the absorbance of the solute, ε is the extinction coefficient, c is the concentration and l is the length of the beam through the sample.

The magnetite nanoparticles, magnetite nanoparticles functionalized with BSA or *Taq* polymerase were diluted with milli-Q water (1:1000). The *fluorescein cadaverine* standards and samples were prepared with the dispersion medium Phosphate-Buffered Saline (10 mM PBS) and, the samples further diluted in PBS (1:10). The wavelength range used was from 200 to 900 nm, the split aperture was 5 nm, and 10 mm path length quartz cells were used.

2.5.2. Fourier Transform Infra-Red Spectroscopy

Fourier Transform Infra-Red Spectroscopy (FT-IR) is extensively used in quantitative as well as in qualitative analysis[139]. This technique is based on the ability of the sample to absorb several different frequencies of light at once and changing those parameters by each repetition of data points. The IR spectrum results from the plot of absorption (or transmission) as a function of the wavelength (or frequency)[140]. The adsorption bands, from 780 nm to 1000 μm, are linked to particular vibrations of the sample functional groups and, therefore, identification of materials is made possible[140]. FTIR instrumentation is an asset for rapid and reproducible IR spectra for a variety of sample types, including nanomaterials[140].

The Fourier Transform Infra-Red Spectroscopy (FTIR) spectrum was captured using an ATR module with a spectral resolution of 4 cm^{-1}. Samples were prepared by drying and placing the resulting powder onto the sample compartment. Measurements were performed in a spectral range from 400 cm^{-1} to 4000 cm^{-1} with a compartment pressure of approximately 2 hPa.

2.5.3. Transmission Electron Microscopy

Transmission Electron Microscopy (TEM) is a technique that can measure the size of the nanoparticles in study, their shape, aggregation state and size monodispersity. An accelerated electron beam is transmitted through the sample, and the wavelike character of electrons is used to create an image of the sample[141]. The high resolution, in the order of 0.2-0.5 nm[142], is achievable with the application of really small wavelengths, which can be possible if the electron beams are accelerated at several hundred kV as is derivable from the **equation (4)**:

$$\lambda \sim \frac{1{,}23}{\sqrt{V}} \ (nm) \qquad\qquad\qquad (4)$$

where λ is the wavelength and V the accelerating voltage applied. Electrons cannot move in atmosphere, therefore is obligatory the use of high vacuum in this technique[141]. From TEM images an accurate size of inorganic structures is obtained[143], instead of a size based on a hydrodynamic radius.

JEM-2100-HT is the multipurpose electron microscope used to characterize these samples. It operates with a high brightness LaB6 electron gun, with a working range of 80 to 200 kV. It is equipped with "OneView" 4k x 4k CCD camera. Appropriate dilutions of all formulations were prepared with milliQ-water and 7 µL of each solution were casted onto a carbon coated copper TEM grid which was then allowed to dry. The analysis of the core size is done by averaging the size of more than 150 nanoparticles for each sample with the software ImageJ.

2.5.4. *Inductively coupled plasma atomic emission spectroscopy (ICP-AES)*

The technique inductively coupled plasma atomic emission spectroscopy (ICP-AES) allows the quantification of elemental species. Elemental ions are excited, and when returning to ground state emit characteristic energies that are element-specific. These emitted wavelengths are dispersed by a diffracting grating, which allows for simultaneous quantification of several elements present in the sample[144].

A stock solution of the element to be analysed – iron - with a well-defined concentration was used to prepare standards with a range of concentrations from 0.025 to 1 ppm. A calibration curve is then stablished. The sample preparation consisted in mixing 10 µL of the NPs solution and 990 µL of hydrochloric acid (37 %) in a 15 mL falcon and leaving them to react overnight. Then, 9 mL of milli-Q water were added, making up to 10 mL of total volume. The iron concentration was analysed using the iron emission wavelength of 235 nm.

2.5.5. *Confocal microscopy*

Confocal microscopy consist in the formation of an image, point by point, through a source of light that is directed to the sample. The reflected light from the specimen passes through a pinhole aperture – the light that comes from other planes other than the focal plan is rejected[145]. An important aspect of this type of microscopy is being able to work and study live cells – and the high-resolution confocal images that result from this technique[146]. From this data collection it is possible to reconstruct the sample in three dimensions[146].

Escherichia coli cells (JM109 – 1 McFarland) were incubated with magnetite nanoparticles as described further in section **2.7.5.** and then visualized under the scanning confocal microscope with the 488 nm laser line and 63x oil immersion objective.

2.5.6. Dynamic Light Scattering

Dynamic light scattering (DLS), also known as photon correlation spectroscopy, is a widely used technique to determine size, polydispersity index (PDI) and zeta potential of particles. Because this is technique is founded on the Brownian movement of particles, it grants the study of the hydrodynamic size of the particles. A laser source crosses through the sample and the fluctuations of the particles can be measured and correlated to the size. The experiment itself determines the velocity of this motion, known as the translational diffusion coefficient (D) expressed on **equation (5)**:

$$d(H) = \frac{K_B T}{3\pi\eta D} \tag{5}$$

where, $d(H)$ represents the hydrodynamic diameter, K_B the Boltzmann's constant, T the absolute temperature, η viscosity and D the translational diffusion coefficient.

Therefore, as the size of the nanoparticle increases the translational diffusion coefficient decreases – the bigger the particle the lower the velocity it has. The fact that the particles are dispersed in a liquid can change some of its characteristics. The hydrodynamic radius that is measured by DLS is the radius of the hypothetical hard sphere, that diffuses with the same speed as the particles under study[147]. The results from DLS can be influenced by factors such as sample preparation, sample concentration, coloured and fluorescent samples, agglomeration, shape, rotational diffusion, cuvette issues, and maintenance of the instrument[147]. This technique is a less expensive screening method, useful to obtain statistically reliable values of size, with a simpler sample preparation in comparison with other techniques (a dilution is enough). The polydispersity index (PI) indicates the homogeneity of a solution: small PI values indicate a narrow size distribution of particles and a value above 0.5 correlates to a broad distribution in size[148].

Often, DLS is combined with other techniques providing an integrated measurement like Electrophoretic Light Scattering (ELS). ELS is an analytical method that measures the electrophoretic mobility of a suspension of particles or macromolecules[149]. It differs from DLS in that over the random Brownian motion of particles a directed motion is imposed by the application of an electrical field[149]. This is a technique used to measure the zeta potential of particles - the potential at the slipping/shear plane of a colloid particle moving under electric field. The particles move according to their charge, creating an oscillating electric field driven by an electrical potential. Therefore, ELS only informs about relative charge and not the value itself. Also, it is important to understand that the higher the absolute value, the more stable the sample analysed is – evaluation of shelf stability. Zeta potentials greater than +30 mV and -30 mV are considered strongly cationic

and strongly anionic[150], respectively, hence there is sufficient repulsive force to attain better physical colloidal stability[148] – more stability.

The average size, PDI and zeta potential of magnetite nanoparticles and magnetite nanoparticles functionalized with BSA were measured with a Dynamic Light Scattering System. This equipment has a nanometric resolution from three Åm to eight μm. All measurements were performed with a carbon electrode cell at room temperature and with an appropriate dilution of each sample.

2.5.7. Thermogravimetric analysis

Thermogravimetric analysis (TGA), an analytic technique mostly used for qualitative measurements[151], monitors and records changes of physical or chemical properties of a sample (like its mass) as function of temperature or time[152]. A temperature program, that may consist of heating, cooling, isothermal holds or a combination between any of them, is employed[152] – the changes that are observed can be caused by various processes as degradation, decomposition, vaporization of bulk liquids, adsorption of liquids or gases, sublimation, metal oxides reduction, and desorption[153].

Normally, the sample size is between 1 and 100 mg and the sensitivity of the thermobalance can be as high as 1 μg[153]. In a TGA thermal curve, a downward curve signifies mass loss and vice versa. Therefore, TGA can be used to perform an evaluation on the thermal stability of a sample: the sample is subjected to a range of selected temperatures, and if there is no detected mass change it is thermally stable.

TGA experiments were performed in three steps, all of them under argon. First, the sample is heated at 10 °C per minute until 120 °C. The second step consist of maintaining the sample at 120 °C for 10 minutes (to completely remove water). The final step consists of raising the temperature from 120 °C to 800 °C, with an increase of 10 °C per minute. Data analysis is performed by considering the weight of the sample as the weight after the loss of water content at the end of the isothermal 120 °C step and assessing weight retention.

2.5.8. Superconducting quantum interference device (SQUID)

Superconducting quantum interference device (SQUID) is a very sensitive magnetometer that is able to measure extremely low magnetic fields, based on superconducting loops containing Joseph junctions[154]. This technique also provides a non-destructive evaluation[155]. When some materials are placed below a superconducting transition temperature, they become superconductors and no longer have resistance to the flow of electricity[156]. This critical temperature

is achieved with liquid helium coolant[156]. A superconducting loop only contains flux in multiples of flux quantum: if there is a change in the flux applied to this loop, the currents flow opposing the change and creating a phase difference across the junctions[154]. This leads to a detectable voltage on the loop – this transduction from flux to voltage is non-linear[154], as it is an oscillating function (with periodic variations) of the magnetic field intensity[154,156]. SQUID can measure magnetization as a function of magnetic field, assisting on finding the spin structure of a sample[157].

Under zero-field cooled (ZFC) conditions the magnetic nanoparticles are cooled below their blocking temperature with no applied field. In field-cooled (FC) conditions the measurements are performed also below the blocking temperature, but under an applied field. This allows for the determination of the blocking temperature, influenced by the distribution of the energy barriers. Field-heated (FH) conditions are used for the measurement of magnetization in function of temperature, obtaining a M-H curve ranging from 1.8 to 300 K.

The magnetic saturation (M_s), the remanence (M_r) and the coercivity (H_c) of the synthetised magnetite nanoparticles were measured with MPMS® SQUID VSM System from Quantum Design. This system has an unprecedent < $8x10^{-8}$ emu sensitivity at the full field of 7 Tesla and a temperature range from 1.8 to 400 K. The nanoparticles were dried and weighted (between 1 to 2 mg) into a gelatine capsule. The samples were fixed with cotton, placed in a straw attached to a measuring rod and inserted in the equipment. The magnetization measurements were executed at a field of 100 Oe at 5 K and 300 K, and the hysteresis loops were measured in the applied magnetic field range from -20 to +20 kOe at room temperature. Values of magnetic saturation (M_s) of the sample, its remanence (M_r) and its coercivity (H_c) were determined.

2.5.9.   Relaxometry

Relaxometry is the technique that allows the study of relaxation variables in nuclear magnetic resonance with the help of a low homogeneity field. The absorption of electromagnetic radiation by a nucleus (in our case H) is a detectable phenomenon and induces a change in the nuclear spin that is observed within a period of time until it relaxes back to equilibrium. Thus, this equipment allows for the measurement of relaxation times (T_1 and T_2) of water protons. There is a direct correlation between iron concentration and relaxivity: iron oxide nanoparticles can be used as MRI contrast agents since proton relaxivity is directly influenced by the efficiency of a paramagnetic substance to enhance the relaxation rate of water protons[158].

The relaxation times of the nanoparticles were measured with Minispec MQ-60 from Bruker, which provides T_1 and T_2 measurements with high accuracy and reproducibility. It is

equipped with a permanent 1.47 T magnetic field and an "intelligent" [1]H probe with 60 MHz operating frequency. Five different solutions of magnetite nanoparticles were prepared within the range of iron concentrations 0.125 - 2 mM. A PBS buffer (10 mM, pH 7.4) was used as the dispersion medium and all the measurements were done at a temperature of 37 °C. Standard inversion recovery (IR) and Carr-Purcell-Meiboom-Gill (CPMG) sequences were used to measure T_1 and T_2, respectively. Relaxivity values were calculated through the plot of relaxation times (s[-1]) as function of iron concentrations (mM).

2.5.10. X-ray diffraction

X-ray diffraction (XRD) is a relevant method in the study of the nature and morphology of nanocrystals. It is a non-destructive technique and works by estimating the nanocrystal size based on the broadening of the X-ray diffractions[148]. The atomic distance in crystalline materials is in the same order of magnitude as the wavelength of X-rays, it varies from 0.5 Å to 2.5 Å[159]. Incident X-rays are diffracted in a characteristic manner, depending on the sample's lattice spacing, shape and atom type[159] – the periodic nature of a crystalline structure will result in constructive or destructive scattering[160]. This is accomplished by the relation between scattering and structure, through Bragg's law, on **equation (6)**[159,161]:

$$n\lambda = 2d\,sin\theta \qquad (6)$$

where n is an integer representing the order of the diffraction peak, λ is de wavelength of the X-ray, θ is the scattering angle that is inversely proportionally to the interplanar distance d. The diffracted X-rays data is collected at an angle of 2θ, and represented as intensity distribution as a function of the 2θ.

The identification of the samples crystallographic structure was done by an X-Ray diffraction System, X'Pert PRO MRD from PANalytical, by using a copper X-ray tube in a Bragg Brentano configuration. It was equipped with a copper pole at 45 kV, and 40 mA and data were obtained at 2θ = [10 to 90] ° with a 0.0098477 ° step size and a scan velocity of 546.720 s. The dry magnetite nanoparticles were transferred to the sample holder, covering its circumference entirely.

2.6. Functional characterization

2.6.1. Magnetic hyperthermia

In magnetic hyperthermia, the temperatures rises as a consequence of the applied AMF on a magnetic material, like iron oxide[162]. The application of hyperthermia in biological tissues

involves physiological limitations as it can lead to necrosis or carbonization of healthy tissues[163]. There is safety threshold that must be respected, **equation (7)**[164]:

$$H \cdot f < 5\text{x}10^9 \; Am^{-1} \cdot s^{-1} \tag{7}$$

where H represents field strength and f the frequency of the AMF. Also, there is technical limitations, meaning that frequency can only vary between 100 and 300 kHz.

The efficiency of each application depends on the intensity and frequency of the externally applied magnetic field, as it is a compromise between healthy radiation and proper penetration depth into the human body[165]. As **Figure 15**[165] shows, an alternated current passes through an induction coil at a selected frequency, generating a non-uniform magnetic field. Because of that, the sample is centered at the coil, where the amplitude of the AMF is maximum. The temperature achieved is recorded as a function of time, field, or frequency.
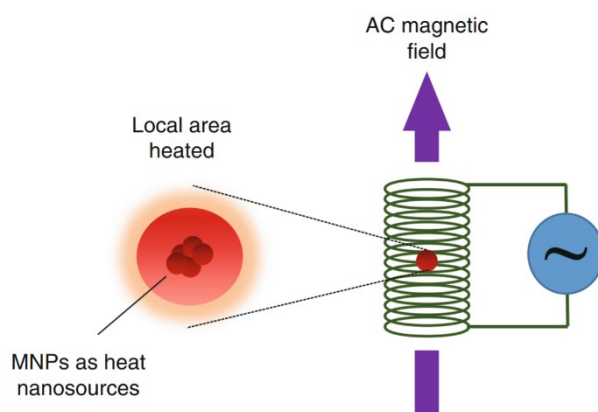
Figure 15. Schematic representation of an experimental set-up of magnetic hyperthermia.

The capacity to change the overall macroscopic temperature of the samples was tested in four solutions of $Fe_3O_4@PAA$: the stock samples with iron concentrations of 21, 23.2, 13.55 and 6.45 mg.mL^{-1} (respectively, of formulations (1), (2), (3) and (4)) and solutions of all formulations with iron concentrations of 0.928 mg.mL^{-1}, 0.232 mg.mL^{-1} and 0.0928 mg.mL^{-1}. The dispersion medium used was milli-Q water. The frequency was fixed at 869 kHz and the alternating magnetic field applied was fixed at 200 G (20 mT).

2.6.2. *Magnetic resonance imaging*

The evaluation of the formulations efficiency as MRI contrasting agents was executed on a MR Solutions 3.0 Tesla benchtop MRI system. The measurements were performed at room temperature with a field of 3.0 T. Sample suspensions of 25, 50, 75 and 100 µM in iron were prepared with milli-Q water as the dispersion medium. A fixed volume of 300 µL of each suspension was loaded into wells from a custom PLA printed MR holder, and the remaining spaces were filled with milli-Q water as reference. The quantitative measurements of parametric T_1 and T_2 maps were

obtained using the MPRAGE (magnetization prepared rapid gradient echo) and the MEMS (multi-echo multi-slice) sequences, respectively. The parameters, T_R (repetition time), T_E (time to echo) and T_I (inversion time), used for these four different measurements are listed in **Table 4**. The data was analysed with ImageJ program using MRI analysis calculator v1.0 plugin, and T_1 and T_2 maps are represented in a layout prepared with GIMP 2 freeware.

Table 4. Number of echoes, T_R, T_E, and T_I listed values for MRI procedures MPRAGE and MEMS.

	Echoes	T_R (ms)	T_E (ms)	T_I (ms)
MPRAGE	11	10000	5	50
MEMS	10	1500	15	15

2.7. *In vitro* studies

JM109 competent cells (Escherichia coli strand) from Promega® were harvested and used as host cells for the plasmid pCMV-GFP was a gift from Connie Cepko (Addgene plasmid # 11153 ; http://n2t.net/addgene:11153 ; RRID:Addgene_11153)[166].

2.7.1. *Growth of bacteria culture*

Lysogeny broth (LB) and LB agar were both prepared as instructed by their manufacturers. After autoclaving the medium, the antibiotic ampicillin (100 µg.mL^{-1}) was added in sterile conditions. LB agar was poured onto the plates and cooled. Both the plates and LB medium were kept at 4 °C. A fresh selective plate is prepared by streaking one colony across the agar plate and grown at 37 °C overnight. One colony (or even more biomass, as needed) from the selective plate was scooped and grown in LB media at 37 °C at 200 rpm to the required optical density at 600 nm. The total volume of LB was no more than a fifth of the total volume of the recipient.

2.7.2. *Competent bacteria transformation*

The competent cells were transformed by heat shock in an aseptic environment by using a laminar flow hood. JM109 cells were removed from conservation at -80 °C and were left to thaw on ice. In a chilled Eppendorf tube, a 25 µl aliquot of cells was pipetted together with 0.5 µL of plasmid DNA with a concentration of 0.25 mg.mL^{-1}. The tube was gently swirled on ice for a few seconds to mix the solutions by finger flicking the tube and incubated on ice for 30 minutes. The tube was then heat shocked by placing it in the Thermomixer® at 42 °C for 45 seconds with no agitation. Then, it was placed on ice for 2 to 5 minutes. 500 µl of chilled LB media were then added, gently shaked and incubated in the Thermomixer® at 37 °C for 90 min with shaking at 300 rpm. Bacteria were pelleted by centrifugation at 12 000 rpm for 30 seconds. The supernatant was discarded, except a volume of around 120 µL to resuspend the cells. 10 µl of bacteria solution

were spread onto LB selection plates with a sterile cell spreader. The plate was placed upside down in the 37 °C Orbital Shaker and incubated overnight. Plates were then stored at 4 °C.

2.7.3. Plasmid extraction

One colony from the selective plate was scooped and grown in 5 mL of selective LB at 37°C at 200 rpm overnight. The bacteria were collected by centrifugation for 15 minutes at 4 °C and the supernatant was discarded. The extraction of the plasmid pCMV-GFP from the *E. coli* cells was tried using the QIAprep Spin Miniprep Kit from Qiagen®, QIAGEN Plasmid Giga Kit from Qiagen®, GRS Plasmid Purification Kit from GRiSP®, Zippy Plasmid Miniprep Kit from Zymo®, and following each protocol, or additional lysis through 3 cycles of freeze-thawing and 10 cycles of sonication - an adaptation from Silva *et al*[167] – to QIAprep Spin Miniprep Kit protocol. The retrieved quantity of plasmid was quantified with NanoDrop™. The plasmid was stored at -20 °C until further use.

2.7.4. Minimum Inhibitory Concentration (MIC)

The determination of the Minimum Inhibitory Concentration (MIC) was performed following EUCAST reading guide for broth microdilution, updated on 1st January 2022. First, a new fresh plate was spread with the bacteria and grown at 37 °C overnight. Biomass was sampled to 5 mL of NaCl 0.95 % (m/v) solution, vortexed and corrected to the same turbidity as a 0.5 McFarland standard. Samples were diluted to an inoculum size of 10^5 CFU/mL. The last step was repeated two more times, as to have triplicates for every sample.

The negative control was composed of 200 μL of LB media and the positive control was composed of 100 μL of LB media and 100 μL of culture. The samples' wells were filled with 200 μL of LB media. 100 μL of a Fe_3O_4@PAA (III) solution (iron concentration of 1 mg.mL^{-1}) was pipette to the first well in triplicates. The solution was mixed thoroughly by pipetting up and down multiple times. Serial dilutions (1:2) were perform until there were 10 experimental samples. The range of tested iron concentration was between 3.3×10^{-1} mg.mL^{-1} and 1.3×10^{-3} mg.mL^{-1}. 100 μL of culture were added to experimental samples. The samples were incubated for 12-18 hours at 37 °C. Inhibition of growth was checked visually, and each concentration plated in several dilutions for CFU count.

2.7.5. Nanoparticle internalization

The quantification of the internalization of these nanoparticles into the JM109 bacteria transformed with the pCMV-GFP plasmid was performed by adapting existing protocols[168]. First, a

new fresh plate was spread with the bacteria and grown at 37 °C overnight. Biomass was sampled to selective LB media and grown at 37 °C at 135 rpm. The total volume of the culture was 400 mL. Sample was measured and adjusted to the turbidity of 1 McFarland. The control and experimental samples all had a total volume of 10 mL. 1 mg of Fe_3O_4@PAA (III) formulation was added to the experimental samples totalling to a final concentration of NP per sample of 100 $\mu g.mL^{-1}$. Samples were collected at timepoints 0, 1,2, 4, 8 and 24 h.

The next phase of the protocol was started immediately after collection. Samples were centrifuged at 4000 g for 20 min and the supernatant was discarded. The pellet was resuspended in 5 mL of EDTA 0.02 M and gently inverted for 30 seconds to remove extracellular NPs and then centrifuged at 4000 g for 20 min, discarding the supernatants. This last step was repeated. The remaining pellet should only contain internalized nanoparticles. The pellets were acid digested by adding 1 mL of hydrochloric acid 12 M and the samples were filtered through 0.22 μm PES syringe filters from Branchia®. Quantification of iron was done through ICP at 235 nm.

For confocal imaging of internalized NPs, Fe_3O_4@PAA-*fluorescein* NPs were used with one hour of incubation. Total iron concentration was 4.6×10^{-2} $mg.mL^{-1}$.

2.7.6. Viability assay with hyperthermia

The study of magnetic hyperthermia influence on the growth of JM109 bacteria transformed with the pCMV-GFP plasmid was studied. The culture was grown until it reached the same turbidity of 1 McFarland. 500 μL of culture were added into three sterile glass tubes, and each tube had an iron concentration of 0, 1.35×10^{-2} and 1.35×10^{-2} $mg.mL^{-1}$ from Fe_3O_4@PAA (III), respectively (labelled as "[Fe]= 0 $mg.mL^{-1}$ + 26 °C, 1h", "[Fe]=1.36×10^{-2} $mg.mL^{-1}$ + 26 °C, 1h", and "[Fe]=1.36×10^{-2} $mg.mL^{-1}$ + HT (268 kHz, 25 mT, 1 h)"). All samples were kept at 37 °C at 135 rpm for NP internalization for 1 hour. The first two samples were kept at 26 °C for one additional hour without shaking, and the remaining one was subjected to induced magnetic hyperthermia for 1 hour at 268 kHz and 25 mT.

20 μL of each sample were added to 180 μL of sterile NaCl 0.95 % (m/v) in a 96-well plate, and then seven serial dilutions were performed. 10 μL (a drop) of each dilution was plated and grown at 37 °C for 24 hours. Each sample CFU count was assessed.

2.7.7. Standard PCR experiments

Colony PCR experiments were conducted in the Applied Biosystems™ Veriti™ Thermal Cycler, a 96-well instrument, to amplify the selected region of a determined construct.

One colony of bacterial cells was resuspended in 20 μL of LB media and grown for one hour at 37 °C, with vigorous shaking (200 rpm). The samples were assembled into 0.2 mL Eppendorf tubes' including *Taq* polymerase (0.25 μL, 1.25 units), dNTPs (1 μL, 800 μM), the GFP chosen primers (2.5 μL, 1 μM each, EGFP-F and EGFP-R), the reaction buffer (10 μL) and 2 μL of the grown culture. The negative control was prepared in the absence of the primers. The total reaction volume was 50 μL. The temperature program used is depicted in **Figure 16**.
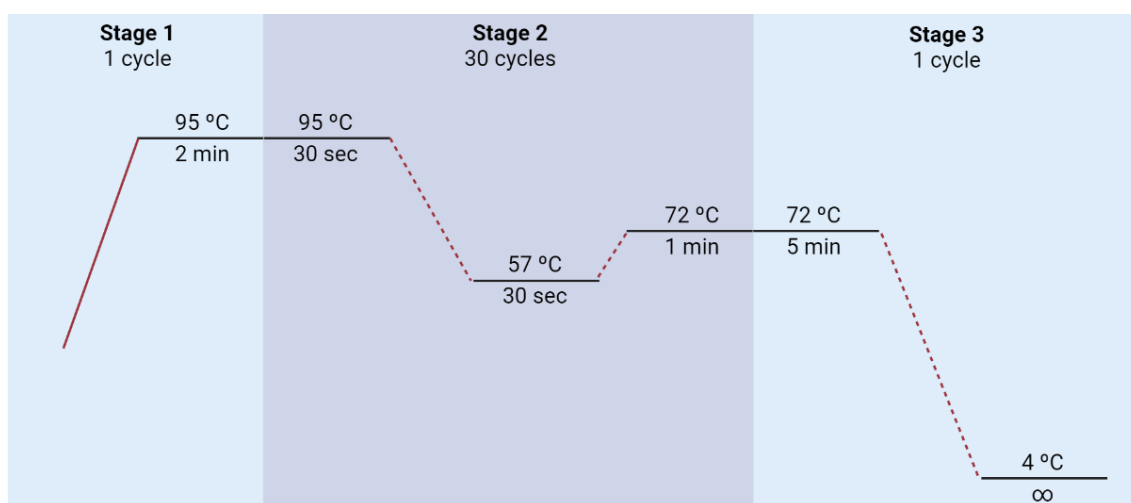
Figure 16. Schematic representation of all phases of PCR amplification program in Veriti™ Thermal Cycler.

The designed primers are named EGFP-F (forward primer) and EGFP-R (reverse primer) and they were designed with the OligoAnalyzer™ and Primer3web (version 4.1.0) tools. These segments are highlighted in the plasmid sequence in **Annex 1**. To allow for future functionalization via coupling reaction onto the surface of the magnetite nanoparticles, the primers were also ordered with an amino link C12 modification on their 5'end. These were purchased from ALS® and their properties are listed in **Table 5**. Final product output is a 950 base pairs (bp) length sequence.

Table 5. Name, sequence, length, melting temperature and GC% of the forward and reverse GFP specific primers (oligos).

Oligo name	Sequence (5' → 3')	Length	T_m (°C)	GC%
EGFP-F	[AmC12]TAACAACTCCGCCCCATTGA	20	59.09	50
EGFP-R	[AmC12]CCAGCCACCACCTTCTGATA	20	59.31	55

2.7.8. Electrophoresis gel analysis

The gel was prepared with a final concentration of agarose of 0.5 or 1 % on the running buffer (sodium burate) from Sigma-Aldrich®. The gel was stained with Invitrogen™ SYBR™ Safe DNA Gel Stain following their protocol. The warm gel solution was placed in the gel casting apparatus with an appropriate comb to create the wells. Running Sodium Burate Buffer was added until the solidified gel remained covered. The GeneRuler 1kb Plus DNA ladder was loaded as well as the PCR samples (6 μL), which already have loading dye. The gel was then run under a voltage of 300 V for 60 minutes. Gel images were obtained with Gel Imaging System (Gel Doc™ EZ) with the UV tray applicator. Digital analysis of PCR-electrophoresis gel using ImageJ software was performed following Antiabong, *et al.*, (2016) protocol[169].

2.7.9. PCR reaction with Fe_3O_4@PAA-Taq

The same protocol as the standard PCR reaction (section **2.7.7**) was followed, substituting "free" *Taq* polymerase (1.25 units) with Fe_3O_4@PAA-*Taq* (3.75 units). Also, another reaction was performed, using pCMV-GFP (0.25 μL, 25 ng) plasmid as template instead of the grown culture.

2.8. Magnetic hyperthermia cycles for PCR

The capacity to change and control the overall macroscopic temperature of the Fe_3O_4@PAA (III) sample was evaluated with the stock nanoparticle sample, which has an iron concentration of 23.2 mg.mL^{-1}. The dispersion medium used was milli-Q water. The frequency was fixed at 268 kHz and the alternating magnetic field applied was varied in a range from 0 to 320 G (0 to 32 mT) to achieve the desired temperatures. The cycle used is detailed in **Table 6**. This amplification program was performed with JM109 *Escherichia coli* cells with pCMV-GFP (8 μL grown culture) or pCMV-GFP (4 μL, 100 ng), Fe_3O_4@PAA-*Taq* ([Fe]=1.89 mg.mL^{-1}, 15 units of *Taq*), dNTPs (4 μL, 800 μM), the GFP chosen primers (10 μL, 1 μM each, EGFP-F and EGFP-R), and the reaction buffer (40 μL) which are the same proportions of the reaction in **2.7.9**.

Table 6. Listed description of step-by-step PCR amplification program in magnetic hyperthermia equipment.

Step	Function	Time (s)	*H* (G)	*f* (kHz)
1	Temperature stabilization	60	-	-
2	Attaining 90 °C	45	320	268
3	Maintaining 90 °C	180	170	268
4	Achieve annealing temperature	270	-	-
5	Maintaining 57 °C	30	70	268
6	Attaining 72 °C	6	320	268
7	Maintaining 72 °C	60	105	268
8	Attaining 90 °C	15	320	268

| 9 | Repeat step 4-8 for 30 cycles total | - | - | - |
| 10 | Skip step 8 in cycle 30; maintain 72 ℃ | 300 | 105 | 268 |

CHAPTER THREE:

RESULTS AND DISCUSSION

CHAPTER THREE: RESULTS AND DISCUSSION

1. Magnetite nanoparticle synthesis

The requirements that the synthetic protocol needed to provide for these magnetite nanoparticles were: high concentration of nanoparticles, large quantity and an average size optimized for magnetic hyperthermia application. Four formulations were synthesised, varying the PAA content and temperature to attempt to achieve different core sizes: Fe_3O_4@PAA (I) was synthesised with 1 gram of PAA at 200 °C; Fe_3O_4@PAA (II) and Fe_3O_4@PAA (III) were synthesised with 2 grams at 150 and 200 °C, respectively; Fe_3O_4@PAA (IV) was synthesised with 4 grams of this polymer at 200 °C. As the elements of this synthesis were joined together, a black precipitate was formed in all formulations, even before the closing and placement of the autoclave reactor on the oven. After retrieving the solution from the oven, it was possible to observe the same characteristic black colour of magnetite solutions. The synthesized nanoparticles were extensively characterized. Structural, magnetic, chemical, using the structural, magnetic, chemical, and functional characterization techniques detailed in **Chapter Two**.

First, the magnetite nanoparticles were characterized using dynamic light scattering – which allowed for the determination of the hydrodynamic size, PDI and average zeta potential of the nanoparticles, as shown in **Table 7**. Even though the Fe_3O_4@PAA (IV) synthesis had a higher polymer content and a higher hydrodynamic size, the hydrodynamic size of the formulations does not seem to directly correlate to the amount of polyacrylic acid added to the reactions. PDI values refer to the dispersity of the sample, the higher the value, the more polydisperse is the sample. Values above 0.4 indicate that the sample has a very broad particle size distribution[170]. According to the PDI (DLS) results, all samples are polydisperse, except formulation (III), which has an acceptable PDI value for most biomedical applications. The negative values of the average zeta potential of these formulations come from the carboxylic acids present at the surface of the nanoparticles. This highly negative zeta potential contributes to nanoparticles repelling each other, which improves colloidal stability. Moreover, having a final formulation with negative average zeta potential is advantageous, as positively charged NP are more rapidly cleared from the organism[62], thus they will remain in body longer - which aligns with their application.

Table 7. Average hydrodynamic size (nm), polydispersity index (PDI), zeta potential (mV), core size (nm) and PDI of all four PAA coated magnetite NPs.

Formulation	Polyacrylic acid content (g)	Hydrodynamic size (nm)	PDI (DLS)	Zeta potential (mV)	Core size (nm)	PDI (TEM)
(I)	1	55.6 ± 5.3	0.77 ± 0.15	-32.2 ± 0.9	7.1 ± 2.1	0.63
(II)	2	39.74 ± 19.4	0.83 ± 0.20	-70.0 ± 1.2	5.8 ± 1.3	0.30
(III)	2	45.4 ± 4.9	0.41 ± 0.09	-44.4 ± 0.8	9.0 ± 2.1	0.51
(IV)	4	101.1 ± 10.7	0.94 ± 0.02	-54.5 ± 0.35	6.5 ± 1.9	0.57

The magnetite nanoparticle formulations were also characterized by TEM - a statistical study of the size of the crystal core of the NPs was completed. The core size does not account for the organic coating, and thus, the TEM size is expected to be smaller than the DLS size, as registered also in **Table 7**. Moreover, the formulation (II) presents a good PDI value, the remaining formulations are in the range of moderate polydispersity[171]. On **Figure 17**, the magnetite nanoparticles present a spherical-like morphology. Formulations (II) and (III) appear to be crystalline (**Annex 3, Figure 38**). The core size distribution of the nanoparticles is shown in **Figure 17**, and shows that the inorganic core diameter ranges from 3 to 16 nm. Analysis of the TEM measurements using Gaussian curve fits show average core sizes of 7.0 nm, 5.5 nm, 8.6 nm, and 6.1 nm, respectively of each formulation in numeric order. As it is possible to note, immediately pouring PAA after the sodium hydroxide in the Teflon reactor and the increase in temperature affects the core size of the resulting nanoparticles: as intended the Fe_3O_4@PAA formulation (III) has a higher core size of 8.6 nm by the gaussian curve, when compared to 5.5 nm of formulation (II). However, altering the amount of PAA in the initial reaction does not appear to have the expected correlation effect in the core size. Additionally, there is no association between the hydrodynamic size (determined by DLS) and the average core size of any formulation.

Even though the theoretical ideal core size of magnetite nanoparticles for hyperthermia applications is about 16 nm[172] and the obtained average core size of the synthesized nanoparticles was smaller, it was decided to proceed with the nanoparticles produced using formulation (III), as is later discussed.

Furthermore, ICP measurements of each sample confirmed and quantified the present iron in formulation: (I) 13.55 mg.mL^{-1} (242.6 mM); (II) 21 mg.mL^{-1} (376 mM); (III) 23.2 mg.mL^{-1} (415.4 mM); and (IV) 6.25 mg.mL^{-1} (111.9 mM).
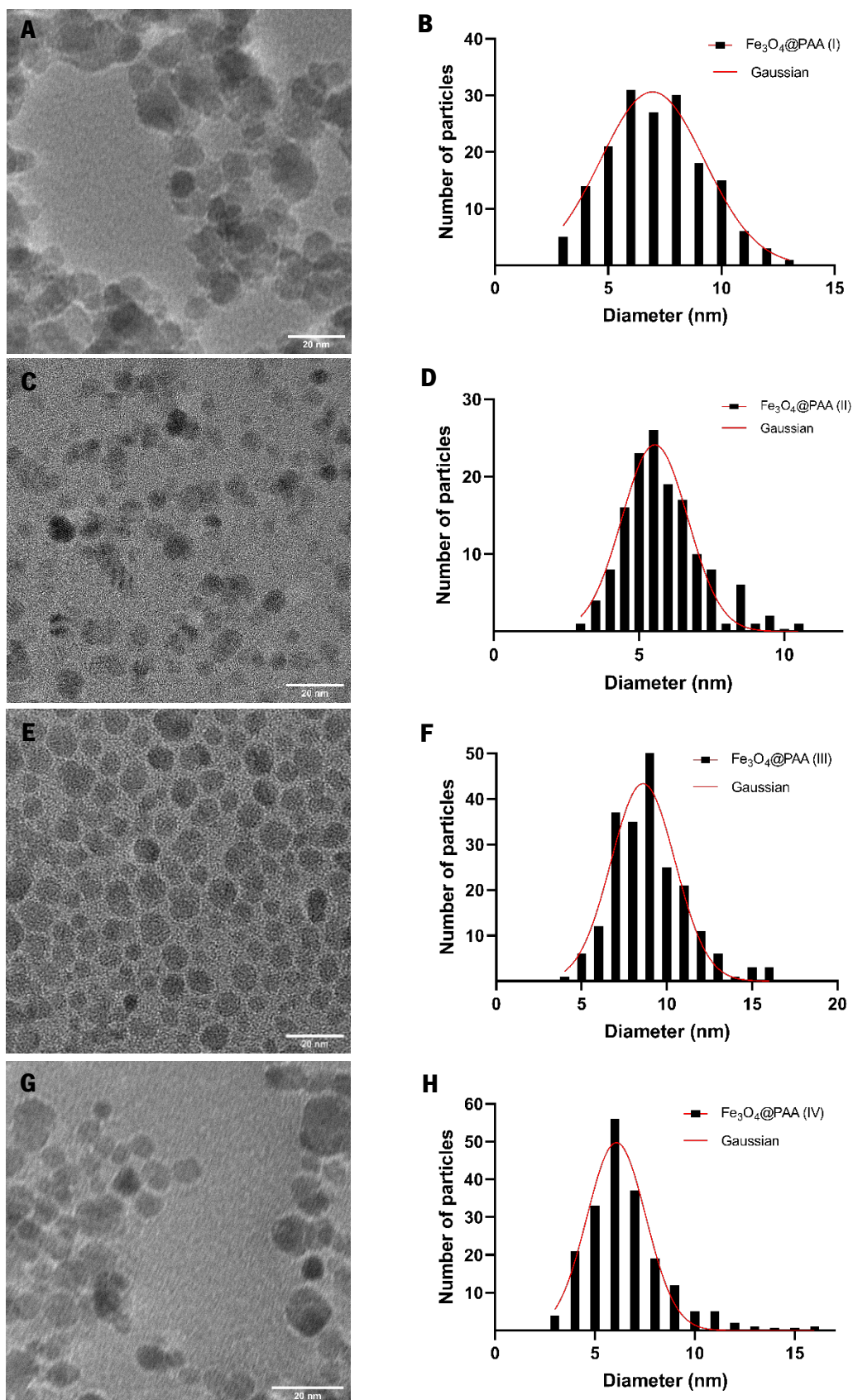
Figure 17. TEM micrographs of magnetite NPs coated with PAA (scale bars correspond to 20 nm), and their diameter distribution obtained by TEM, fitted with a Gaussian distribution: **(A-C)** Fe$_3$O$_4$@PAA (I); **(A-C)** Fe$_3$O$_4$@PAA (II); **(A-C)** Fe$_3$O$_4$@PAA (III); **(A-C)** Fe$_3$O$_4$@PAA (IV).

The X-Ray diffraction pattern of the magnetite nanoparticles coated with PAA is represented in **Figure 18**. Examining the nature of Bragg's peaks appearing in this XRD pattern, they match with the defined Bragg reflections of magnetite (JCPDS file no. 19-0629), which have 2θ values of 30.18 °, 35.55 °, 37.18 °, 43.21 °, 53.76 °, 57.15 °, 62.77 °. These peaks are shown and indexed as (2,2,0), (3,1,1), (2,2,2), (4,0,0), (4,2,2), (5,1,1) and (4,0,0), respectively, in the same figure. All synthesis match the pattern peaks, meaning that they are all composed by magnetite. No other significant peak is present in any of the spectra, confirmation of the good purity of the samples.
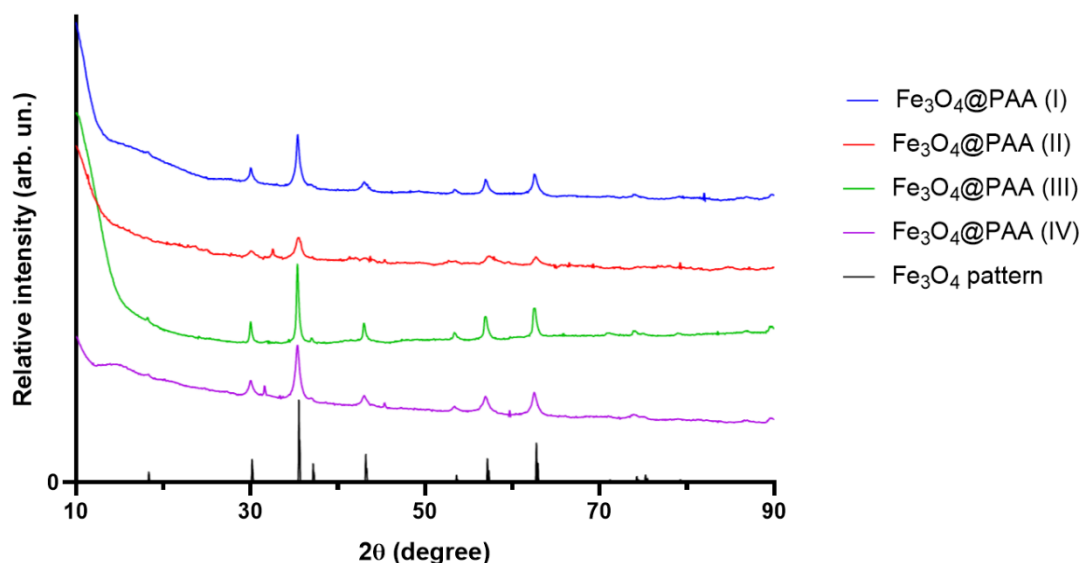
Figure 18. X-Ray diffraction pattern of all formulations of magnetite nanoparticles coated with PAA and the match magnetite pattern.

The UV-Vis spectra of all Fe_3O_4@PAA synthesis are presented in **Figure 19**, showing a common characteristic: the increase of the intensity of absorbance as the wavelength of the excitation light decreases, being consistent with subwavelength sized dielectric spheres (similar to L. Silva, *et al.*, 2020[173]). The spectra also show that there is no obvious absorption peak, even though a shoulder can be observed around 260 nm, coming most surely from the PAA capping of the nanoparticles.
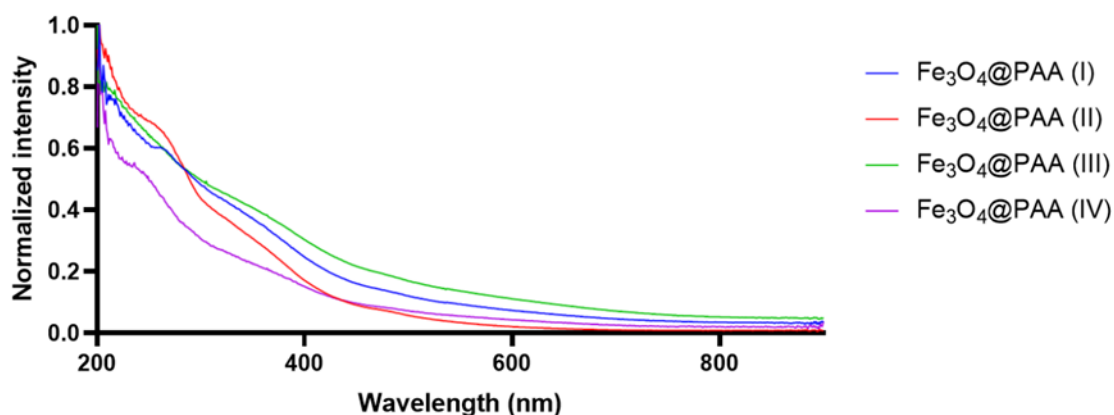
Figure 19. Ultraviolet-Visible normalized spectrums of all Fe_3O_4@PAA formulations.

The FTIR analysis of $Fe_3O_4@PAA$ and PAA was performed to evaluate the chemical nature of the surface of the nanoparticles, resulting in the spectra represented in **Figure 20**. These spectra exhibit a characteristic peak of the vibration of Fe^{2+}-O^{2+} groups at 555, 553, 572 and 561 cm^{-1}, respectively in formulation order (which generally takes the value of 589 cm^{-1}). A very intense peak at 1554 cm^{-1} in the PAA spectrum belongs to an asymmetrical vibration of COO^- [174], and after capping magnetite with this compound, the peak suffers a shift to a higher wavelength, at 1558 cm^{-1} for $Fe_3O_4@PAA$ (I), (III) and (IV), but lower wavelength for formulation (II). The subsequent peaks around 1395 cm^{-1} belong to the symmetrical vibrations of carboxylic acid groups, may it be free or bound[175], also shifting after the capping. Additionally, the peaks between 2800 and 3000 cm^{-1} show the presence of symmetrical C-H vibrations. This analysis confirms that the capping of magnetite with polyacrylic acid was successful.
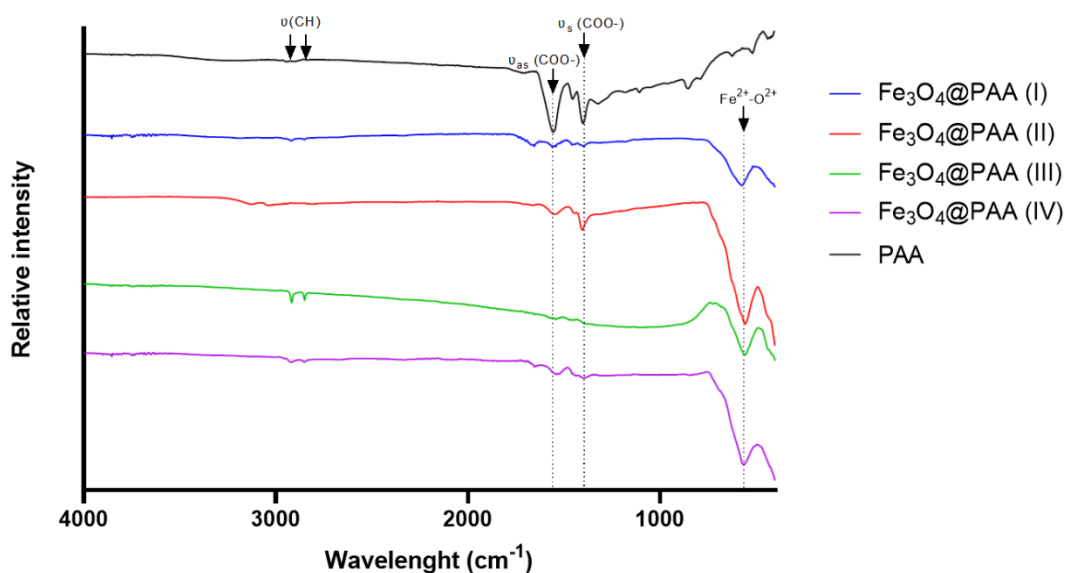
Figure 20. Fourier Transform Infra-Red spectra of the synthesised $Fe_3O_4@PAA$ formulations.

The thermogravimetric analysis of the nanoparticles formulations enables the determination of ratio between organic and inorganic content of the solutions. The profiles represented **Figure 21** were obtained after the normalization of the sample weight at 120 °C, where all water should be evaporated, thus leaving only the dried sample for examination. Up to around 600 °C, it is possible to observe loss of organic content from the samples. Given the nature of these samples, polyacrylic acid coated magnetite nanoparticles, the organic content is referent to PAA. The $Fe_3O_4@PAA$ (I) formulation retains 84.6 % of its weight, meaning there is a loss of 15.4 %; formulation (II) loses 34.67 % of organic content; the $Fe_3O_4@PAA$ (III) formulation loses 5.6 %; and $Fe_3O_4@PAA$ (IV) loses 47 %. Except for the $Fe_3O_4@PAA$ (III) formulation, for which a higher loss was expected, the formulations have a correlated loss of weight to PAA composition ratio. From

these data summarized in **Table 8**, we can assume that, for unknown reasons, the capping of PAA in formulation (III) was not as successful as in the remaining formulations. The amount of poly(acrylic) acid on the surface of these nanoparticles can dictate how they behave magnetically, as the interactions of the polymer and its quantity surrounding the nanoparticles' core can lead to different magnetic behaviours through modulation of interparticle magnetic interactions.
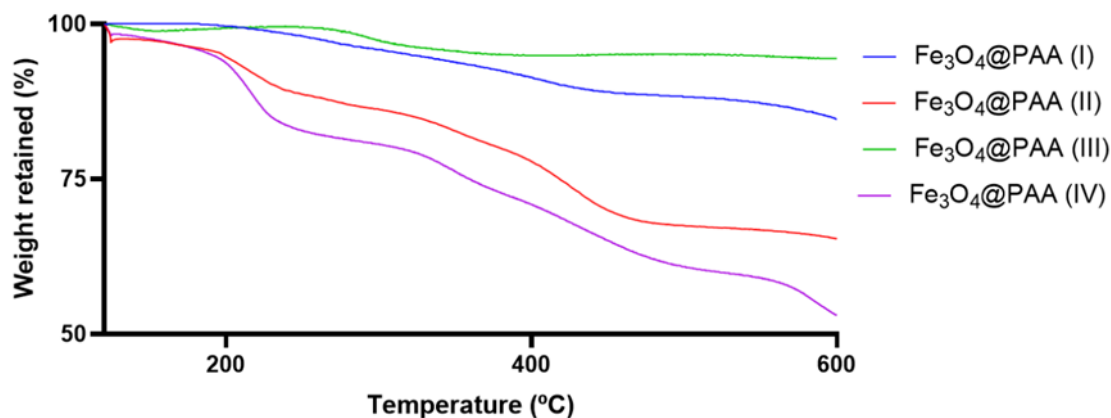
Figure 21. Thermogravimetric profile of the synthesised Fe_3O_4@PAA particles.

Table 8. Comparison between added PAA to weight retained (%) and respective loss of organic content (%) of all synthesized formulations.

Formulation	PAANa added (g)	Weight retained (%)	Losses of organic content (%)
Fe_3O_4@PAA (I)	1	84.6	15.4
Fe_3O_4@PAA (II)	2	65.3	34.7
Fe_3O_4@PAA (III)	2	94.4	5.6
Fe_3O_4@PAA (IV)	4	53.0	47.0

The SQUID analysis of the Fe_3O_4@PAA samples was performed with field-heated, field-cooled (FC), and zero-field-cooled (ZFC) configurations. The correspondent graphs are shown in **Figure 22**. In the plot of the ZFC-FC curves, **Figure 22A**, it is possible to distinguish two different magnetic behaviours, which are separated by T_B. The blocking temperature is approximately, in numeric order of formulations, 210 K, 105 K, more than 300 K, and 147 K. As said before, above this temperature the nanoparticles exhibit superparamagnetic behaviour[48], but below they exhibit ferromagnetic behaviour. It is also possible to observe the Verwey temperature transition, an electrical transition, around 100 K for formulation (III), as pure bulk magnetite exhibits[176] – the magnetite crystal lattice shifts from a monoclinic structure insulator to the metallic cubic inverse spinel structure (remaining so at room temperature), which is an effect of the long range ordering of Fe^{2+} and Fe^{3+} ions[177].

In **Figure 22B-C**, are shown the *M-H* magnetization curves at 5 and 300 K of each formulation. These hysterisis loops allow us to gather information about the magnetic saturation (M_s) of the sample, its remanence (M_r) and its coercivity (H_c). At the temperature of 5K it is noticeable the ferromagnetic-like behaviour (open loop) of all formulations, indicating that the nanoparticles are in a blocked state. On the other hand, at room tempertaure (300K or 27 °C), M_r and H_c are quasi-zero, as the nanoparticles are in the superparamegnetic regime. These latter values are registered in **Table 9**. The obtained magnetic saturation values of all formulations are smaller than the literature value for bulk magnetite, 92-100 emu.g⁻¹ [178,179], which is expected since particle magnetization significantly decreases as particle size is reduced below about 100 nm, and deviations from bulk behavior are frequently reported[180]. These variations originate in the changes in the magnetic ordering at the surface layer relative to that of the particle core[180].
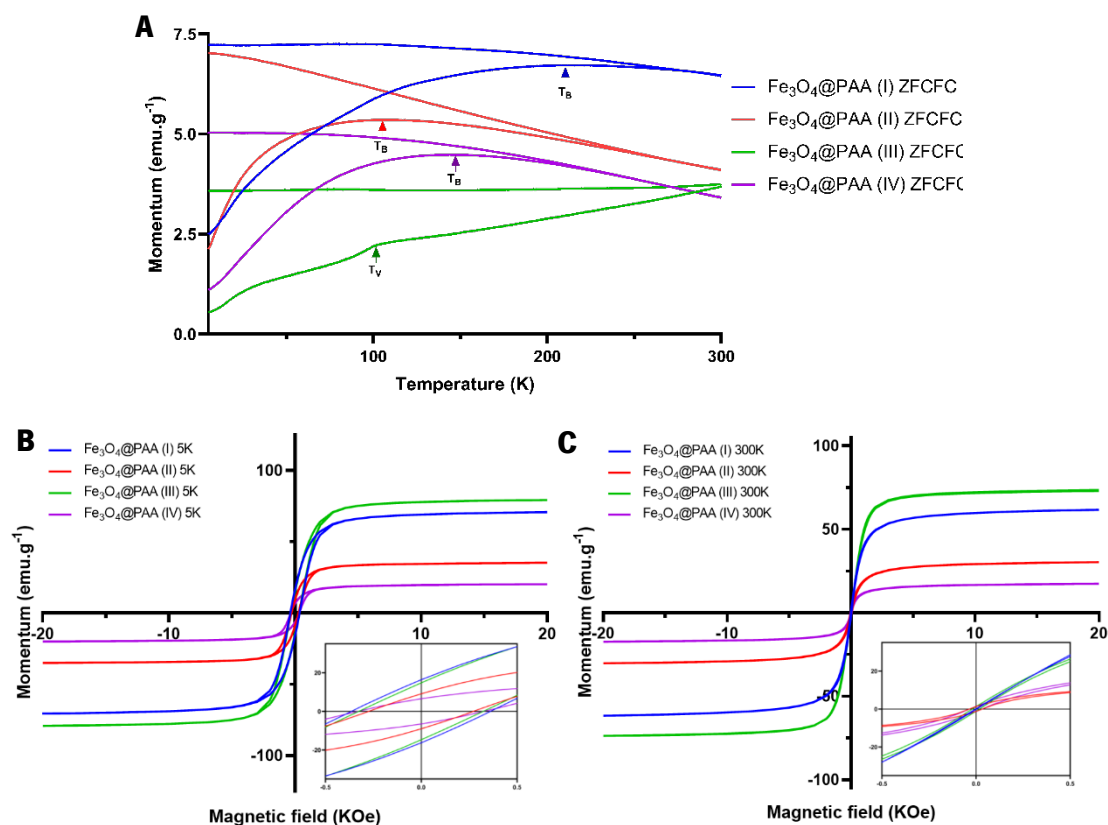
Figure 22. Magnetic characterization of Fe₃O₄@PAA formulations: **(A)** ZFC-FC characterization with an external field of 100 Oe (T_B and T_v are arrow identified when appliable); **(B-C)** hysteresis curves measured at 5 and 300 K, respectively, in the range of -20 to 20 kOe.

Table 9. Summary table of blocking temperature (T_B) and magnetic saturation (M_s), coercivity (H_c), and remanence (M_r) at 300 K.

Formulation	T_B (K)	M_s (emu.g⁻¹)	H_c (Oe)	M_r (emu.g⁻¹)
Fe₃O₄@PAA (I)	210	61.7	1.2	12.8
Fe₃O₄@PAA (II)	105	30.3	1.4	16.3
Fe₃O₄@PAA (III)	>300	73.6	1.0	111.3

Fe$_3$O$_4$@PAA (IV)	147	17.3	0.7	51.1

The extrapolation that formulation (III) has the largest core size, because it has the higher value of Ms, is consistent with TEM data (9.0 ± 2.1 nm). Core size is an important element to take into account in the nanoparticles' heating capacity for this project. However, the hydrodynamic size of this formulation is not the higher one, and, as said before, the size results from DLS do not seem correlated with amount of PAA, nor the core size. This is also the formulation that possesses the Verwey transition, which is a sign of its purity.

The characterization of the MR imaging capabilities of these nanoparticles was performed via relaxometry and MRI studies. The relaxometry was performed on the synthesised nanoparticles and relaxivity values were obtained by plotting the inverse of the relaxation time (relaxation time, in seconds^{-1}) dependence on iron concentration (mM) – shown in **Figure 23(A-B)**. Imaging tests were performed through MRI by quantitative experiments (T_1 and T_2 parametric maps), presented also in **Figure 23(C-D)** for all formulations. The respective linear regressions from these quantitative experiments are showed in **Annex 4** (**Figure 39**). **Table 10** shows the calculated r_1
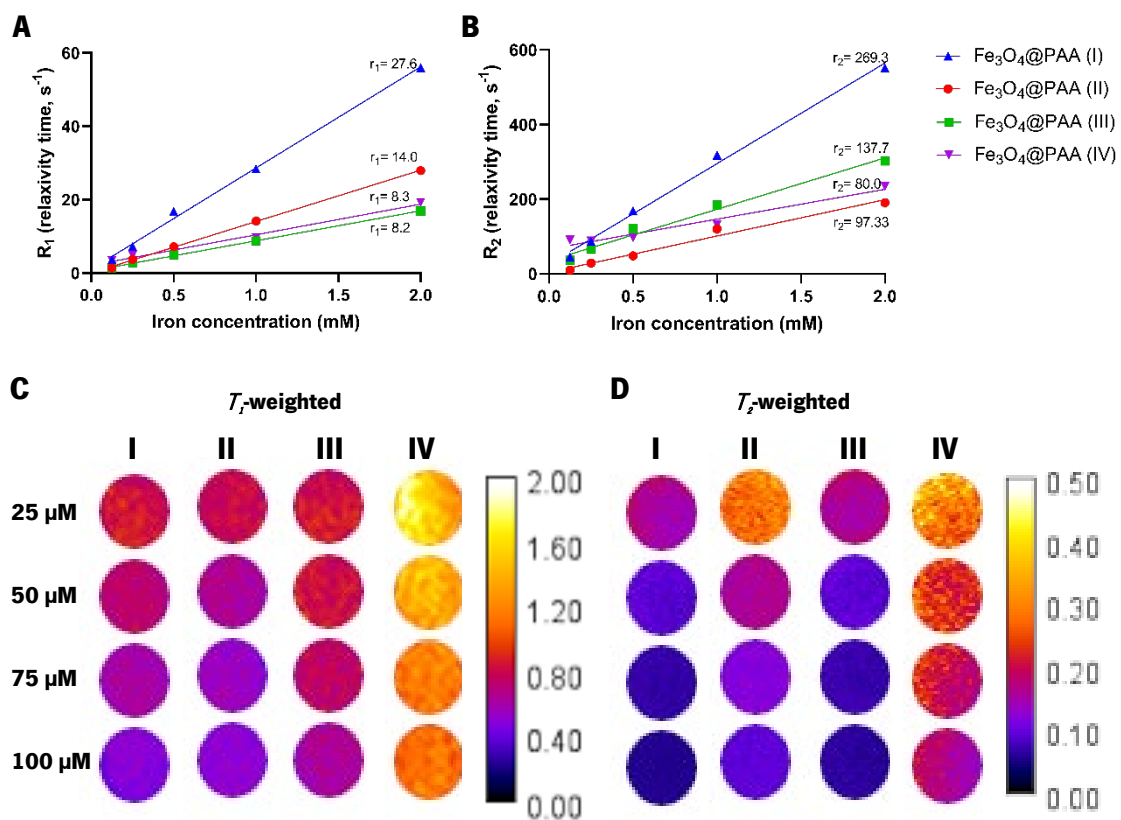
Figure 23. Linear regressions between relaxation time (s^{-1}) **(A)** R$_1$ and **(B)** R$_2$ and the concentration of iron (mM) of Fe$_3$O$_4$@PAA nanoparticles; and T_1 map **(C)** and T_2 map **(D)** quantitative measurements of Fe$_3$O$_4$@PAA (I), (II), (III) and (IV), respectively, with iron concentrations of 25, 50, 75 and 100 μM from top to bottom in each representation. Calibration bars are respectively after each map.

and r_2 values, as well as the r_2/r_1 ratios obtained from both techniques. Both relaxometry results and quantitative measurements (obtained using MPRAGE and MEMS sequences, respectively for T_1 and T_2) showed a contrast dependence on the concentration, showing clearly that these nanoparticles have a predominant T_2 contrast effect, as expected. The r_2/r_1 ratio gives information regarding the contrast agent: the higher the ratio is, the higher the T_2 effect[181]. It is also affected by the molecular structure of the capping agent[182]. The ratio does confirm that synthesis (I) and (II) could show dual contrast behaviour (both T_1 and T_2 contrast) as stated by the intermediate value of this ratio. The obtained values of r_1 are systematically lower with the MRI technique than with the relaxometry since the magnetic field applied is higher[183]. The r_2 values seem similar between the two techniques, even though they are significantly higher in the relaxometry data for formulation (I) and (IV), which can derive from the possible sedimentation of nanoparticles in solution within the measurement period (longer for MRI tests).

Additionally, it appears that formulations (I), (II), and (III) have a comparable contrast when compared to the r_2 values of the FDA-approved Resovist® (61 $mM^{-1}.s^{-1}$ at 1.5 T, and 143 $mM^{-1}.s^{-1}$ at 3T)[184]. When compared to r1 values of Resovist® (8.7 $mM^{-1}.s^{-1}$ at 1.5 T, and 4.6 $mM^{-1}.s^{-1}$ at 3T) all formulations are comparable, except the formulation (IV) has a lower T_1 contrast. Both formulations (I) and (II) have an unexpected higher T_1 contrast. It is know that the relaxation time depends on the diameter of the nanoparticles in study, and generally, higher r_2 implies higher core size for magnetite nanoparticles[185,186]. Since formulation (I) has a higher r_2, it was expected that these nanoparticles' core size was bigger than the remaining formulations. Yet, the relaxivity of a formulation not only depends on its core composition and size, but size distribution, capping agent and other parameters[186]: so it is likely that other factors are interfering with the relaxivity, and that formulation (I) is not the bigger one.

Table 10. Data registration of r_1, r_2 and r_2/r_1 ratio for both relaxometry and MRI characterization.

Formulation	Relaxometry (1.47 T)			MRI (3.00 T)		
	r_1 (mM^{-1}.s^{-1})	r_2 (mM^{-1}.s^{-1})	r_2/r_1	r_1 (mM^{-1}.s^{-1})	r_2 (mM^{-1}.s^{-1})	r_2/r_1
(I)	27.6	269.3	9.8	11.8	163	13.9
(II)	14	97.3	7	10.0	95.1	9.6
(III)	8.2	137.7	16.8	5.2	139.9	27.2
(IV)	8.3	80	9.6	3.6	33.2	9.2

2. Functional characterization

The capacity of the Fe_3O_4@PAA nanoparticles to generate heat under the application of an alternating magnetic field was determined. The values of Specific Absorption Rate (SAR) and ILP (Intrinsic Loss Power) can be calculated from the data of Temperature evolution versus AMF application time. The SAR and ILP are determined using **equation (1)** and **(2)**, respectively for each concentration: the final values were determined by the average value between different concentrations, as SAR and ILP should be independent of concentration (**Table 11**). A graphical representation of the SAR values (average of SAR in different iron concentrations) of all synthesis are embodied in **Figure 24A**. According to this figure, formulation Fe_3O_4@PAA (III) has the greater potential for hyperthermia applications, with a SAR value of 853 W.g^{-1}., which is 7.5 times higher than the SAR reported for Feridex® (a commercial iron oxide nanoparticles-based contrast agent, 115 W.g^{-1})[187]. For this project, the nanoparticles need to reach 95 °C – for the DNA denaturation step – in a matter of seconds, which is possible with formulation (III). As expected, at a fixed field of 20 mT and a fixed frequency of 869 kHz, as the samples are diluted and the concentration of iron lowered, the maximum macroscopic temperature achieved decreases, represented in **Figure 24B**.

Table 11. Data registration of SAR (W.g^{-1}) and ILP (W.(g.kHz)$^{-1}$.mT^{-2}) values for the original stock and for the iron concentrations of 0.93 mg.mL^{-1}, 0.23 mg.mL^{-1}, and 0.09 mg.mL^{-1} of the different formulations.

Formulation	Parameter	Original stock	0.93 mg.mL^{-1}	0.23 mg.mL^{-1}	0.09 mg.mL^{-1}
(I)	SAR (W.g^{-1})	332	388	361	270
	ILP (W.(g.kHz)$^{-1}$.mT^{-2})	9.5E-01	1.1E+00	1.0E+00	7.8E-01
(II)	SAR (W.g^{-1})	145	189	72	90
	ILP (W.(g.kHz)$^{-1}$.mT^{-2})	4.2E-04	5.4E-04	2.1E-04	2.6E-04
(III)	SAR (W.g^{-1})	856	935	720	900
	ILP (W.(g.kHz)$^{-1}$.mT^{-2})	2.5E-03	2.7E-03	2.1E-03	2.6E-03
(IV)	SAR (W.g^{-1})	213	189	179	63
	ILP (W.(g.kHz)$^{-1}$.mT^{-2})	6.1E-01	5.4E-01	5.2E-01	1.8E-01

To be able to mimic PCR conditions - cycle phases with different times and temperatures – several functional studies looking into temperature versus applied field were performed, thus, leading to the protocol described in Chapter Three in heading **2.8**. Looking at each nanoparticle as a local-heat source, the induced temperature variations from nano- to macro-scale are a crucial characteristic to explore. The purpose of this initial optimization of applied fields with such a high
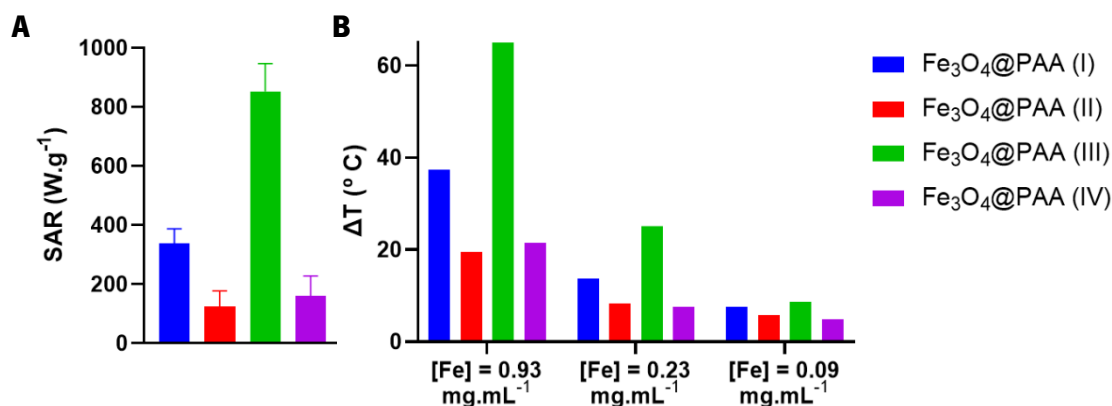
Figure 24. Graphical representation of **(A)** SAR (W.g⁻¹) comparison between formulations and **(B)** maximum achieved temperature at different iron concentrations.

concentration of SPIONs was to try to equal nanoscale and macroscale temperature. Assuming that the macroscopic temperature of the sample registered from the temperature probe is different from the surface temperature of the nanoparticles, with the same applied field and frequency, it is important to point out that only the macroscopic temperature was measured. This solution iron concentration is 23.2 mg.mL⁻¹. However, these conditions are the closest we can get to measuring the actual surface temperature of these nanoparticles, hence lowering the likelihood of experiment-related inaccuracy. This is one of the challenges (macroscopic temperature vs real nano-temperature) of working with nanoparticles that has not been solved – there is still little research on this issue[173].

Figure 25 shows the cycle that will be performed for PCR using the nanoparticle's ability to generate heat. As it is possible to observe, each phase of the cycle is easy to achieve at this frequency (268 kHz): it takes little time to go from room temperature to the temperature needed for the denaturation of DNA (90 to 95 °C, 45 sec); maintaining 57 °C (annealing temperature of the specific GFP primers), reaching and maintaining 72 °C (extension temperature, 6 sec) and reaching and maintaining 90°C (for the start of the following cycle, 15 sec). It is also similar to the time that a normal PCR takes. However, reaching annealing temperature after the denaturation
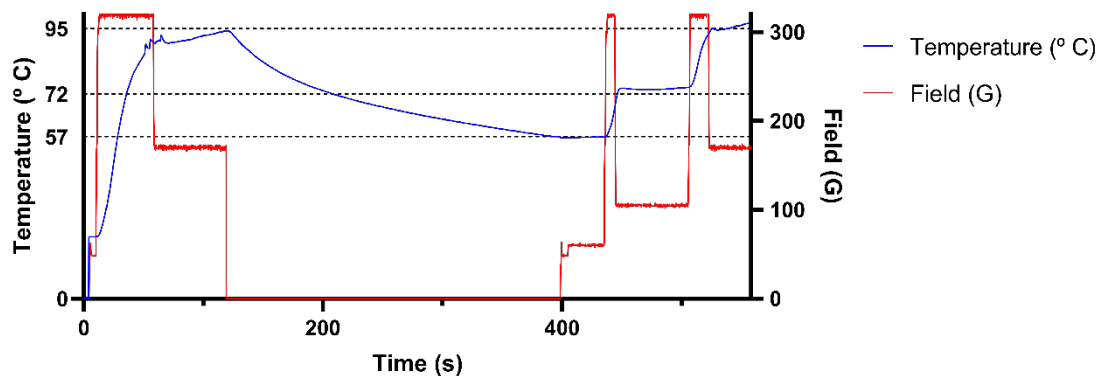
Figure 25. Magnetic hyperthermia experiment with the developed nanoparticles of a full PCR cycle.

phase takes a long time (270 s, approximately) as this system does not have a built-in cooling system. This limits the quantifying opportunities that were feasible before, as it takes 225 minutes to complete thirty cycles. In a rapid cycle, 30 cycles of standard PCR take 10 to 30 minutes [188], depending on the length of the amplified region, while in this case it takes 80 minutes. At the research level, this factor is crucial for amplification detection, but *in vivo* applications time would not be a problem since fewer cycles would be required.

3. Nanoparticles functionalization

Functionalization of nanoparticles with different ligands was achieved through the coupling of carboxylic acid groups of the poly(acrylic) acid polymer on the surface of the magnetite nanoparticles with amine groups on the ligand using peptide coupling reagents, such as EDC and sulfo-NHS.

In an effort to quantify the carboxylic acid groups (from the PAA polymer) on the surface of the Fe_3O_4@PAA nanoparticles available to participate in the coupling reaction, an EDC/sulfo-NHS coupling reaction was performed on the Fe_3O_4@PAA nanoparticles with the ligand *fluorescein cadaverine*. **Figure 26A** shows the absorbance of *fluorescein cadaverine* at various concentrations from 200 to 900 nm (standards) in Phosphate Buffered Saline (PBS, 10 mM, pH 7.4) as the dilution solvent – to make the measurements in pH of 7.4. These standards measurements have a common peak at the wavelength of 481 nm. **Figure 26B** shows the linearization of the absorbance at 481 nm for each concentration of *fluorescein cadaverine*, which allows for the interpolation of the concentration of *fluorescein* in the samples after the coupling reaction. Moreover, as is represented in **Figure 26C** by the data points, as the quantity of nanoparticles increases, the quantity of reacted *fluorescein cadaverine* reaches saturation; the nonlinear regression (curve fit) of these data points is also represented. The nonlinear regression represents the saturation binding of *fluorescein cadaverine* to the NPs, following an adaptation of the binding equation: **equation (8)**. The analysis of this data allows for the calculation of B_{max} and K_d, being their respective values approximately 3.6×10^5 mol and 8.2×10^9 mol.

$$[Fluorescein] = \frac{B_{max}[Fe_3O_4@\text{PAA}]}{K_d + [Fe_3O_4@\text{PAA}]} \tag{8}$$

Considering that the number of molecules of *fluorescein cadaverine* that were bound to the NPs is equal to the number of carboxylic acid groups on the PAA are available for coupling, it is possible to determine the quantity of COOH groups available per Fe_3O_4@PAA nanoparticle. In

more suitable units, it was determined that were available approximately 14.2 μmol of COOH groups available in 100 μL of the stock solution of Fe_3O_4@PAA nanoparticles synthesized or, in other units, approximately 67 available COOH groups in each nanoparticle.
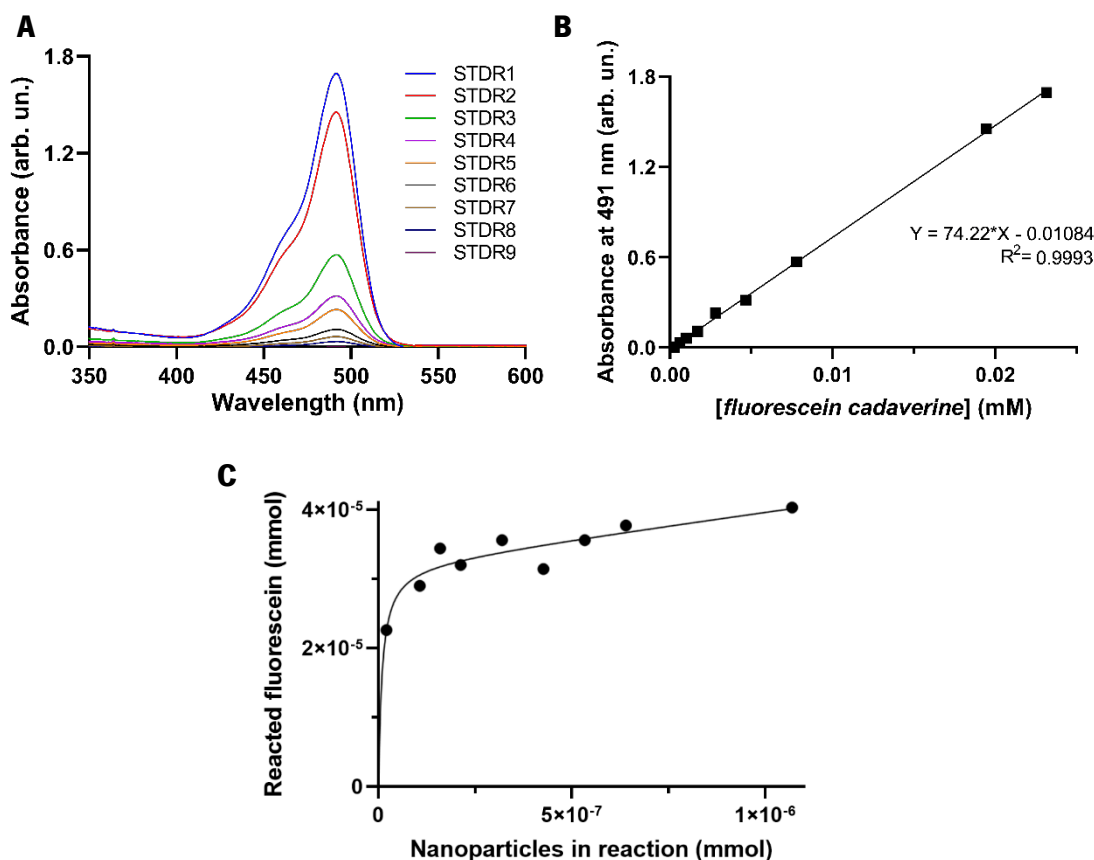
Figure 26. Graphic representation of **(A)** *fluorescein cadaverine* absorbance at different concentrations; **(B)** the linearization of *fluorescein cadaverine* absorbance at 481 nm in function of its concentration (mM); and **(C)** the reacted *fluorescein cadaverine* (mmol) in function of the nanoparticles (mmol) in reaction.

It was then possible to move forward with the process of functionalization of these nanoparticles with different proteins. The goal of this functionalization was to obtain nanoparticles with functional proteins and with protein to nanoparticle ratios of 3:1. The first protein that was functionalized was BSA as this protein is inexpensive, more accessible, and easily quantifiable compared to the protein *Taq* polymerase.

In the development of the optimization process, EDC and sulfo-NHS were used ten equivalents compared to the protein itself; and the quantity of protein used was 3/67 (ratio of three proteins linked to each NP, which has approximately 67 COOH groups available) equivalents in regard to the nanoparticles. The protein optimization process as described lead to the achievement of a ratio of number of protein (BSA) to nanoparticle of 2.8:1, very close to the original 3:1 goal.

After functionalization with BSA, the nanoparticles presented a larger hydrodynamic size of 60.2 ± 6.8 nm, resulting from the presence of proteins on the surface, and a lower absolute

value of zeta potential of -24.5 ± 0.7 mV, surpassing the threshold for a stable formulation (± 30 mV) – below the threshold, the nanoparticles tend to aggregate since the repulsion forces are no longer sufficient to avoid aggregation. This increase in zeta potential may be from the coupling of BSA, as there are less carboxylic acid groups available – and the bound BSA cancel out negative charges of COO^- groups. The Fe_3O_4@PAA (III) suspension had a pH of 6.3, the Fe_3O_4@PAA-BSA solution has a pH of 6.11 and BSA's isoelectric point is between pH 4.5 – 5.0: this implies that BSA is positively charged in the Fe_3O_4@PAA-BSA formulation.

The UV-Vis spectra in **Figure 27** shows that there is also no obvious absorption peak, even though a shoulder can be observed in the spectrum from the sample containing BSA at around 280 nm, which is the location of the expected peak from the absorbance of proteins, like BSA.
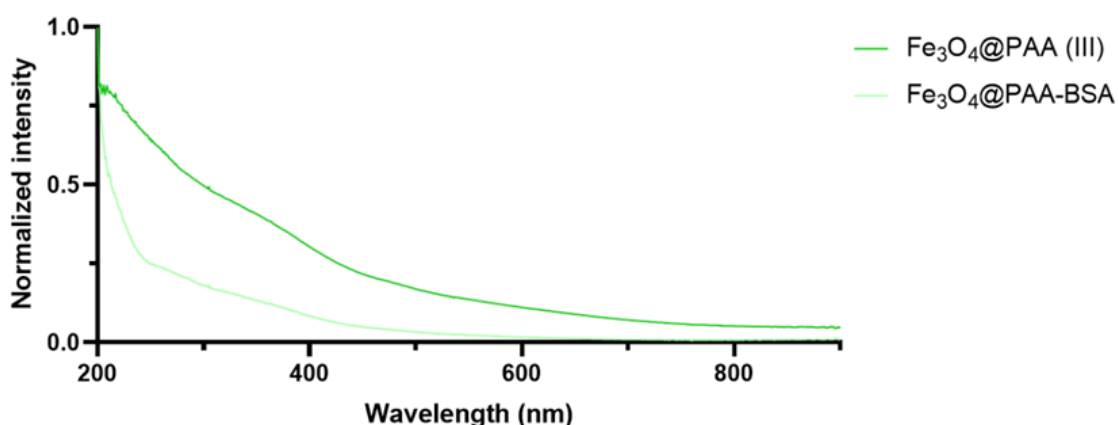
Figure 27. Ultraviolet-Visible normalized spectrums of all Fe_3O_4@PAA (III) formulation and Fe_3O_4@PAA-BSA formulation.

The FTIR analysis of Fe_3O_4@PAA-BSA and BSA was performed to confirm the outcome of the BSA functionalization onto the PAA coated magnetite nanoparticles. This data is represented in **Figure 28**. By comparing the spectrum of Fe_3O_4@PAA-BSA and Fe_3O_4@PAA (III), it is possible to observe changes upon functionalization of the nanoparticles with BSA. The spectra of free BSA and Fe_3O_4@PAA-BSA share common vibrations characteristic of proteins: a very intense peak at 3286 cm^{-1} that shows the presence of stretching hydroxyl peaks, υ(-OH)[189]; symmetrical C-H vibrations between 2800 and 3000 cm^{-1}, identical to all four formulations of magnetite nanoparticles; a peak at 1650 cm^{-1} from C=O the stretching mode of amide I[190]; another at 1521 cm^{-1} from the N-H bending mode of amide II[190], which is indicative of a protein with high proportion of α-helix[191]; another at 1386 cm^{-1} from the C-N stretching mode[190] –strong primary amide scissoring[191]. It is also notable the characteristic peak of the vibration of Fe^{2+}-O^{2+} functional groups at 582 cm^{-1}.
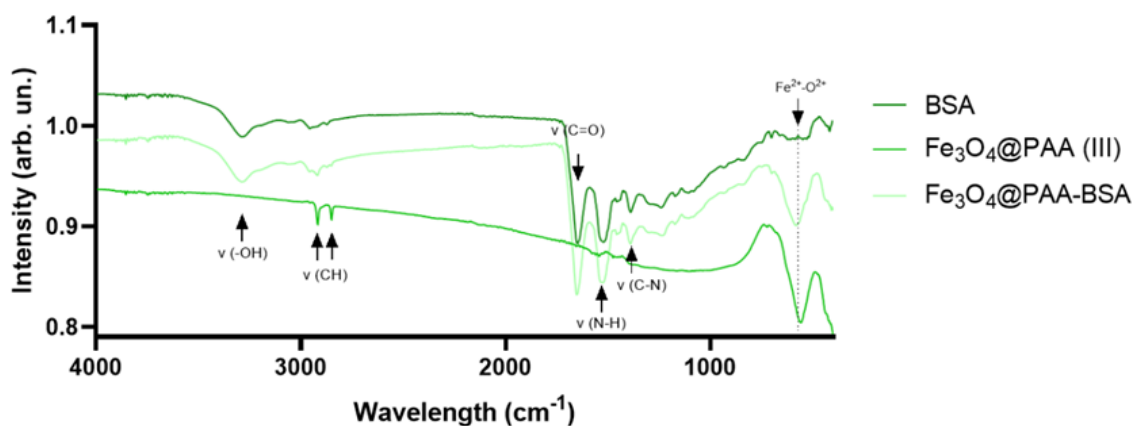
Figure 28. Fourier Transform Infra-Red spectra of Fe₃O₄@PAA (III), Fe₃O₄@PAA-BSA and BSA.

The thermogravimetric analysis of the BSA bounded magnetite nanoparticles allows the determination of ratio between organic and inorganic content of the solutions. The profiles represented in **Figure 29** were achieved with the same protocol as previously. The BSA coupled NPs, showed a higher loss of organic content (11.4 %) when compared to the precursor Fe_3O_4@PAA formulation (5.6 %). Thus, it is possible to conclude that the difference in losses derives from the BSA content of the sample.
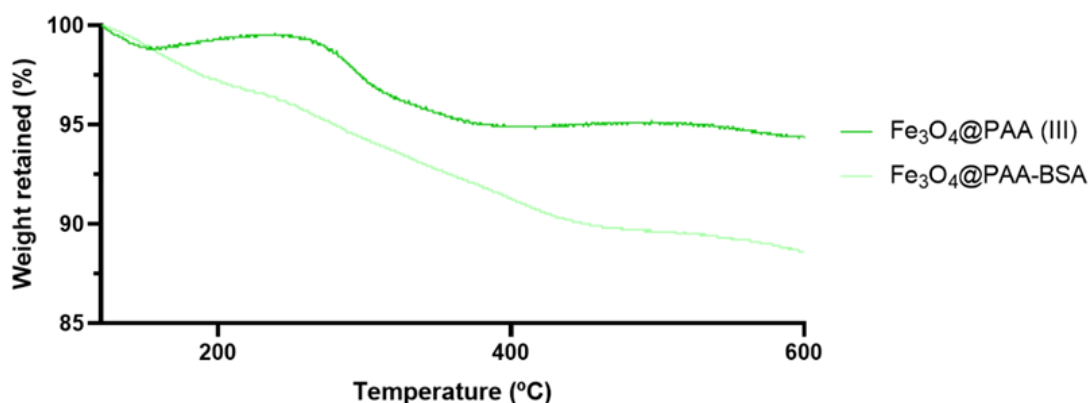
Figure 29. Thermogravimetric analysis of Fe₃O₄@PAA (III) and Fe₃O₄@PAA-BSA.

Importantly, when the magnetite nanoparticles were functionalized with BSA, the maximum temperature achieved by applying AMF was not considerably altered in comparison to the original formulation of magnetite nanoparticles, as it is represented in **Figure 30**. So, protein functionalization onto the surface of magnetite nanoparticles does not interfere with the heat generating capacity of the nanoparticles, at least in the stoichiometries and conditions used in this Thesis.

Following the optimized protocol of protein functionalization described above, *Taq* polymerase functionalized Fe_3O_4@PAA NPs (Fe_3O_4@PAA-*Taq* NPs) were achieved with a ratio of 2.969:1 of *Taq* polymerase to NP.
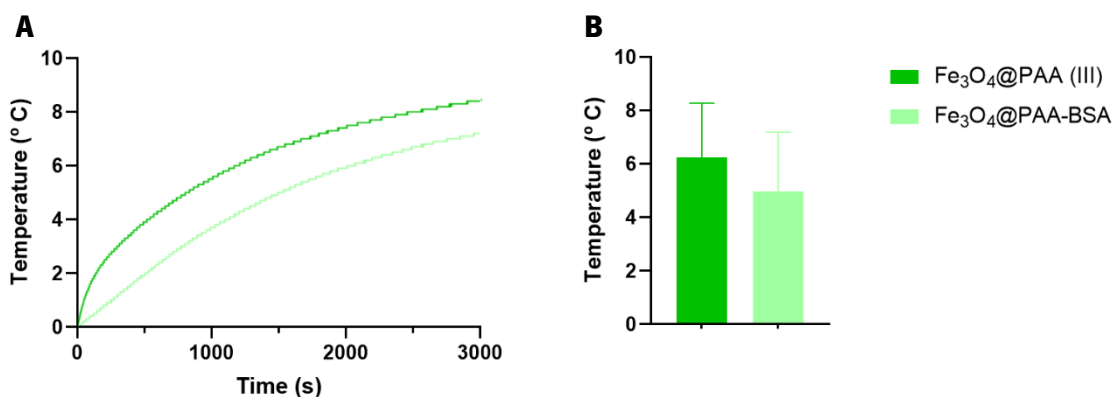
Figure 30. Schematic representation of the maximum temperature achieved of Fe₃O₄@PAA (III) and Fe₃O₄@PAA -BSA under AFM (20 mT, 869 kHz) **(A)** in function of time and **(B)** in cumulative comparison, in which iron concentration equals 0.093 mg.mL⁻¹.

EGFP-F and EGFP-R primers functionalization onto the surface of the nanoparticles was the next step. However, this functionalization was not possible, even though several attempts were made (**Annex 2, Table 12**). Three different quantification techniques were applied to each reaction, but the results remained ambiguous. None of the outcomes aligned between the different approaches. Thus, primers functionalization remained unsuccessful.

4. *In vitro* testing

4.1 Plasmid extraction

Large amounts of plasmid DNA were required to act as the DNA template for the PCR experiments that were to follow. Typically, enough genetic material for such research can be obtained from an overnight cell culture for the purpose of extracting cell material for retrieving plasmid DNA. The transfection of bacteria, in this case *Escherichia coli* cells, with the selected plasmid (pCMV-GFP), was the first step to achieve this goal. After the transfection of JM109 cells with the pCMV-GFP plasmid, they were grown out for the purpose of plasmid extraction. A total of 2.5 Litres of LB selective medium were used, resulting in the extraction of approximately 4.41 mg of the plasmid. The concentration of the plasmid was determined by NanoDrop™, which gave a value of 1.26 μg/μL. The 260/280 and 260/230 ratios are measurements of purity that need to be accounted for. The 260/280 ratio value gives information about the purity of the DNA, as the DNA is considered "pure" when this value is approximately 1.8. On the other hand, the 260/230 ratio is a secondary measurement of DNA purity, which tends to be higher than the previous one and is acceptable between 2 and 2.2. This plasmid sample shows values of 1.829 and 2.037 for the 260/280 and 260/230 ratios, respectively, indicating that the sample could be considered

"pure". The plasmid was kept stored in the Buffer EB that came with the QIAGEN Plasmid Giga Kit at -20 °C until use.

An electrophoresis gel was run to verify the presence and size of the plasmid, represented in **Figure 31(A-C)**: it shows a band of above the 5,000 bp and another one larger than 20,000 bp. Since the plasmid used has 4,479 bp, this sample appears to have supercoiled plasmid DNA (given the larger size - >5,000 bp - identification) and genomic DNA contamination (>20,000 bp). Since plasmid extraction kits follow a precise and well-established technique, contamination is not typically anticipated. The natural next step was to repeat this plasmid extraction using other commercial kits, like the QIAprep Spin Miniprep Kit in **Figure 31(D-F)** and the GRiSP Miniprep Kit in **Figure 31(G-I),** which in the end gave the same kind of genomic contamination at larger base pairs than the molecular weight marker. Without sequencing and without its size, we can only speculate of its nature. If this contamination is in fact genomic DNA, it could come from an inefficient lysis step. To remediate this, an additional lysis step was added after the use of lysis buffers from the QIAprep Spin Miniprep, consisting of 3 cycles of freeze-thawing between -80 and 30 °C and 10 cycles of sonication on ice (30 second pulse, 30 second pause, 30 % amplitude), which is an adaptation from Silva *et al* [167]. This approach resulted in the smeared bands presented
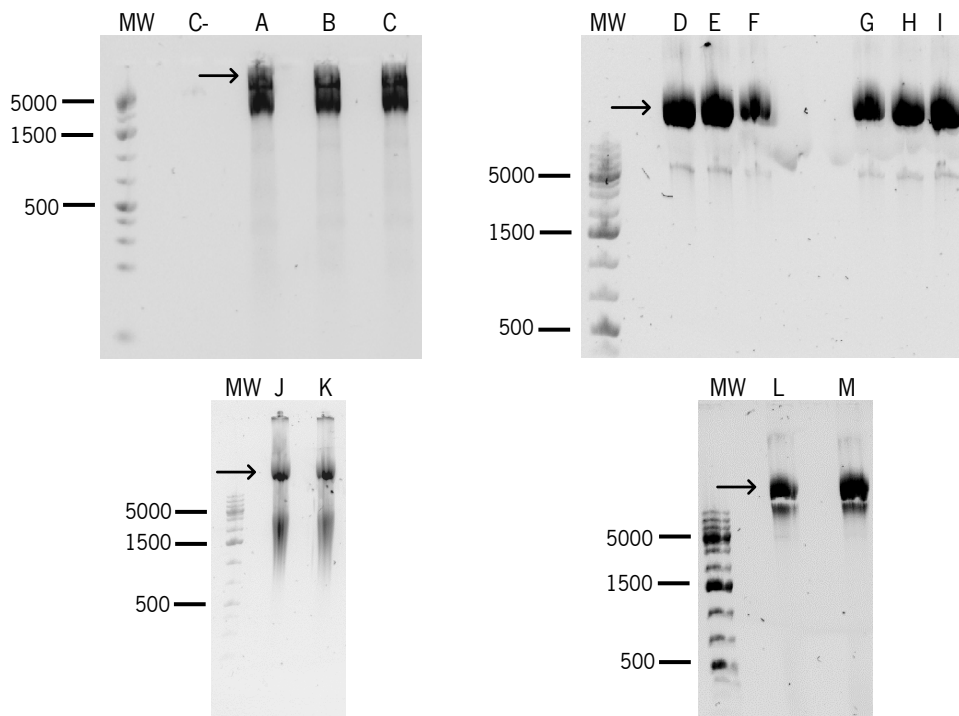
Figure 31. Plasmid extraction agarose gel imaging with **(A-C)** QIAGEN Giga Kit, **(D-F)** QIAprep Spin Miniprep Kit, **(G-I)** GRiSP Miniprep Kit, **(J-K)** QIAprep Spin Miniprep Kit with additional lysis process, **(L-M)** Zymo Zyppy Plasmid Miniprep Kit; MW in each image represents the lane containing the molecular weight ladder and "C-" is the negative control of the experiment (only water). Reference bands are detailed for easier examination (5000, 1500 and 500 bp). Contamination bands are indicated by the black arrows.

in **Figure 31(J-K)**, indicating the degradation of the DNA, and also containing the same contamination. Additionally, the Zyppy Plasmid Miniprep Kit protocol was followed, which is represented in **Figure 31(L-M)**, also demonstrating the same pattern of contamination.

The objective of this section was to extract pure plasmid DNA, yet we were unsuccessful. So, it was agreed to proceed with colony PCR. The high temperature (95 $^\circ$C) in the beginning of the PCR reaction leads to the exit of the plasmid into the PCR solution (through cell lysis), where all reagents are accessible. With the current genomic DNA contamination, it was also considered that *Taq* polymerase inhibition in high DNA concentrations would be unavoidable.

4.2 Toxicity and internalization assays

A Minimum Inhibitory Concentration (MIC) assay was performed within triplicates to evaluate the growth of the JM109 cells in the presence of different amounts of nanoparticles, with iron concentrations ranging from 0 to 0.5 mg.mL^{-1}. Visually, at these range of concentrations there was not a growth inhibition effect, meaning that the MIC value is superior to the concentrations of iron tested. The growth of bacteria could not be quantified through the absorbance at 600 nm, as the nanoparticles interfered in those readings. However, colony-forming units (CFU) counting of all samples were performed (**Figure 32**). The differences between each iron concentration and the control sample were not significant, which confirms the visual assessment of viability. All future assays will be performed within this range of iron concentration.
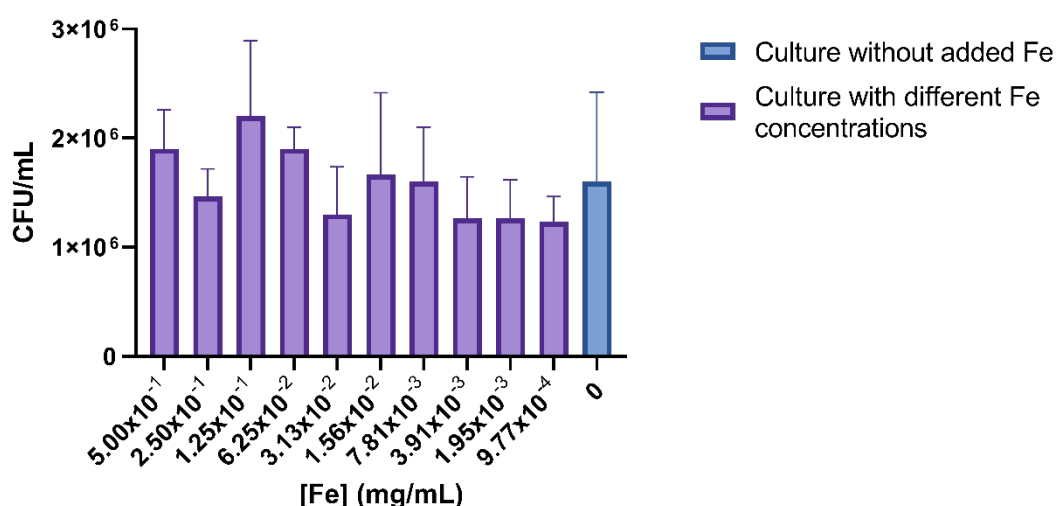
Figure 32. Bar representation of colony-forming units of *Escherichia coli* cells in the presence of different iron concentrations (varying from 0 to 0.5 mg.mL^{-1}): a Minimum Inhibitory Concentration assay by Broth Dilution Method.

The internalization of NPs was studied in the concentration of 100 μg.mL^{-1}. Through ICP-AES it was possible to determine the concentration of iron in the interior of the bacterial cells in

each sample at a given time. A two-way ANOVA statistical test was performed to evaluate the variability of the obtained data. The outcome of this analysis is represented in **Figure 33**. Control samples, only constituted by the LB medium and the culture cells, have dynamic iron contents throughout the experiment period: there is a continuous increase of iron concentration inside the bacterial cells until the hour 8 of growth, which are significative for hour 4 and 8 (p=0.0016 and p=0.0015, respectively). These variations can be explained by their growth phase: *E. coli* doubles its iron contents (in storage) in the transition from exponential to stationary phase [192]. On the other hand, the experimental samples, which had the additional NPs in their culture, revealed that their internalization is noticeable from hour 1. Nevertheless, the low internalization values reflect these nanoparticles coating nature: the lipopolysaccharides on the outer membrane of Gram-negative bacteria, such as *E. coli*, have a negative charge [193] and, consequently, repel these PAA coated NPs, as they also have a negative net charge. There seems to be a decrease in the internalization of NPs from hour 1 through 2, 4 and 8, which can be the result from an excretion mechanism of the active bacterial cells, but at hour 24 the bacteria presented the highest value of internalized iron. The difference of internalization between hour 8 and 24 is also statistically significant (p=0.0092). Overall, the variation of time is not significant, but the variation related to the absence (control data) or presence (experimental data) of NPs is significative with a p value of less than 0.0001. The statistical data implies that the internalization of iron is significative and 1 hour of incubation is enough for the bacteria to internalize a significant amount of nanoparticles.
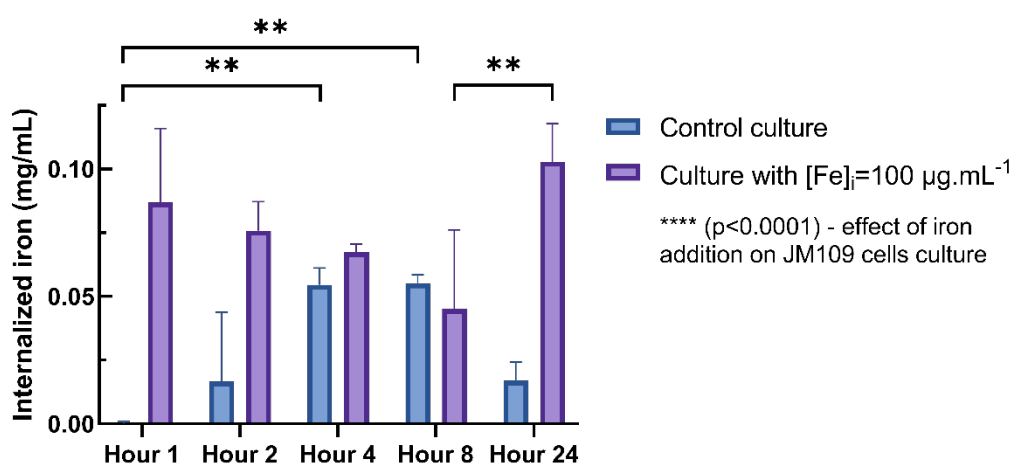
Figure 33. Column graphic detailing concentration of iron (mg.mL⁻¹) in the interior of the E. coli cells after 1, 2, 4, 8 and 24 hours of reaction. Symbols "**" and "****" refer to a comparison with a p value inferior to 0.01 and 0.0001, respectively.

To complement this information, **Figure 34**, shows representative confocal microscopy images of *E. coli* cells that were exposed or not-exposed to Fe$_3$O$_4$@PAA-*fluoresecein* for 1 hour. It is possible to see some nanoparticles agglomerations with variable sizes as well as the fluorescence

of the ligand in some cells and outside of them. This imaging corroborates the data from the internalization assay.
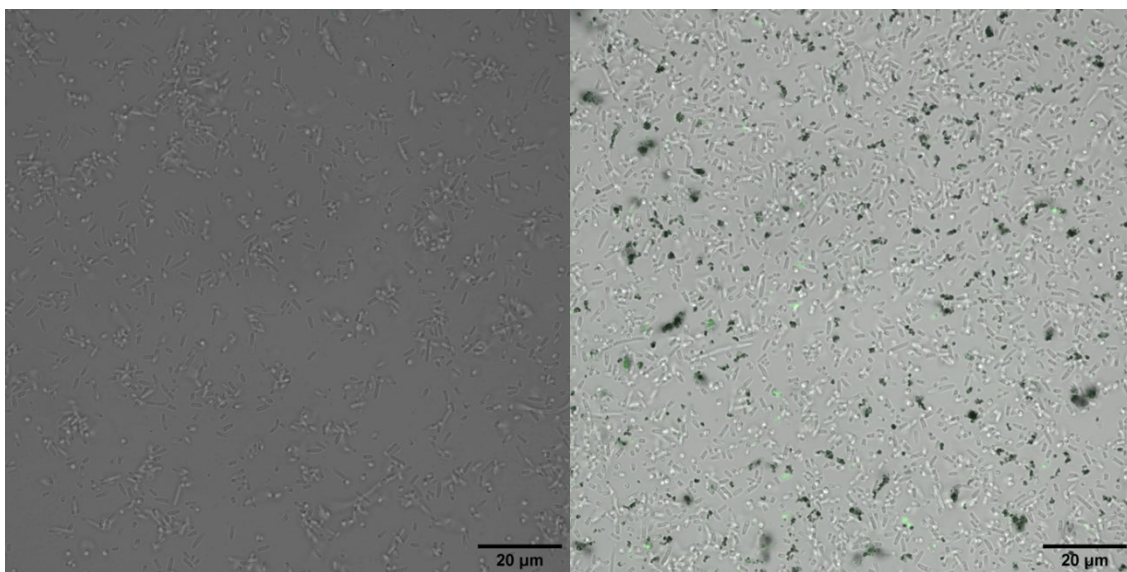
Figure 34 . Confocal micrographs at 63X magnification of *Escherichia coli* cells non-exposed **(A)** and exposed **(B)** to *fluorescein* cadaverine functionalized PAA coated magnetite nanoparticles for 1 hour. Scale bars are 20 μm.

Viability studies with hyperthermia were performed with an iron concentration of 1.36×10^{-2} mg.mL^{-1}. In comparison to the control, the growth of the cells incubated with nanoparticles was not statistically different. The data, **Figure 35**, shows an unexpected average viability increase in the cells that were incubated with nanoparticles and subjected to a hyperthermia protocol (pink bar), as the viability rose to approximately 158 ± 58.7 %, even though a decrease was expected from the exposure to the generated heat. This trend in the growth of the bacteria incubated with NP and submitted to AMF could come from the very mild increase in macroscopic temperature induced by the NPs that activate cell growth. The control sample (blue bar) as well as the cells incubated with nanoparticles (purple bar) were subjected to an incubation at 26 °C for the same period (1 hour) as the hyperthermia protocol was conducted, to minimize the growth effects of rising temperatures for the bacteria. An ordinary one-way ANOVA statistical test was performed to evaluate the variability of the obtained data, which revealed that the effect of the interaction of the cells with nanoparticles only is not statistically significant (p=0.9181); and their further subjection to hyperthermia is also not statistically significant (p=0.0891).
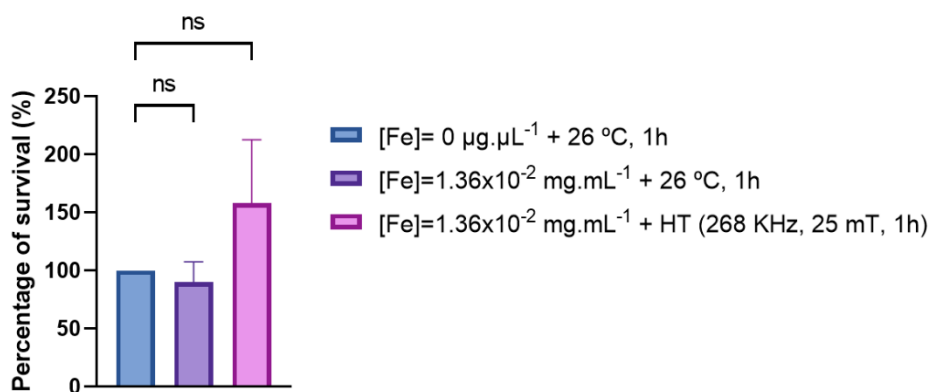
Figure 35. Viability studies on *E. coli* cells with magnetic nanoparticles Fe$_3$O$_4$@PAA (III): in blue is the control group (with no added iron at 26 °C for 1 hour), purple is the bacteria cells incubated with nanoparticles ([Fe]= 1.36x10^{-2} mg.mL^{-1} at 26 °C for 1 hour), and in pink is the bacteria cells incubated with nanoparticles with application of hyperthermia ([Fe]=1.36x10^{-2} mg.mL^{-1} at 268 kHz and 25 mT for 1 hour). Symbol "ns" refers to a p value superior to 0.05.

4.3 PCR: optimization and experimental

Finally, testes on standard PCR reaction and its optimization were started. This led to the procedure detailed in section **2.7.7**. With this protocol, the lack of primers in the sample solution was used as a negative control, since without these components it is not expected any kind of amplification. After optimization, the standard composition of this PCR reaction was used as the "Standard positive control" for the remaining hypothesis, which is displayed in **Figure 36** as "C+". The standard melting temperature was determined to be 57 °C. PCR inhibition by nanoparticles was also evaluated, showing that nanoparticles presence does not affect the outcome of the PCR reaction.

Next, to assess if the activity of *Taq* polymerase was compromised by its functionalization onto the nanoparticles, a PCR reaction was performed with the Fe$_3$O$_4$@PAA-*Taq* substituting the free *Taq* polymerase. **Figure 36A** shows the electrophoresis gel of this reaction compared to the standard positive control. Yet, for the same concentration of *Taq* polymerase in reaction (lane "1x") the amplification band is absent. However, when the concentration of this protein is increased 3 times (lane "3x"), the amplification band is present and of the same size as the standard positive control amplification. So, the protein activity is not compromised. ImageJ gel analysis (**Figure 36B**) revealed that the *Taq* polymerase activity is reduced to 50.9 % when functionalized, and so, when increase its concentration to 3 times (3.75 units – lane "3x") the standard concentration its activity increases to a total of 10 times. It was assumed that because the functionalization can happen anywhere in the protein, the local site specific for extending hybridized primers can in some cases be obstructed; or the steric accessibility of the local site is affected. This can explain why at

66

the same concentration as free *Taq*, Fe$_3$O$_4$@PAA-*Taq* were not able to produce enough copies of the desired gene as to see a band.
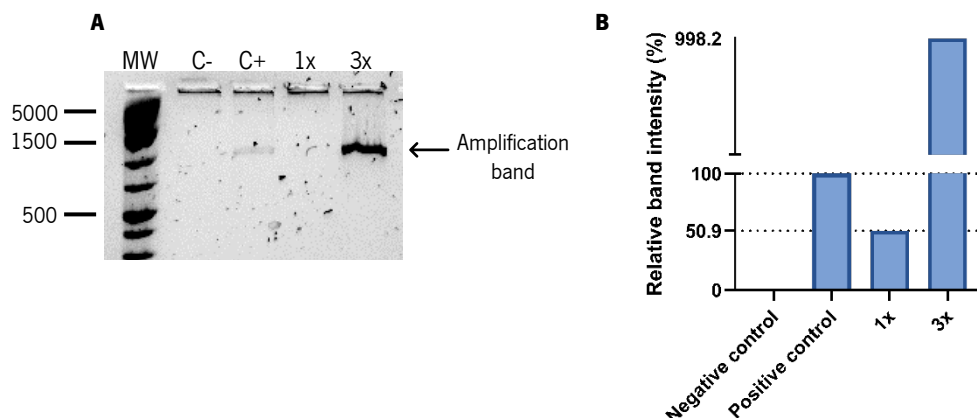
Figure 36. Assessing remaining functionality of functionalized nanoparticles with *Taq* polymerase: **(A)** electrophoresis gel and **(B)** Image J analysis bar representation of relative band intensity of each lane. MW represents the lane containing the molecular weight ladder, "C-" is the negative control of the experiment (without primers), "C+" is the positive control established as standard PCR control, "1x" contains 1.25 units of the functionalized polymerase, and "3x" contains 3.75 units of the functionalized polymerase. Reference bands are detailed for easier examination (5000, 1500 and 500 bp). Amplification band is indicated by the black arrow.

Following, the protocol described in section **2.8**, the magnetic hyperthermia assisted PCR was attempted with the nanoparticle's formulation of Fe$_3$O$_4$@PAA-*Taq* and the grown culture. **Figure 37A** shows the electrophoresis gel of this reaction. Compared to the same positive control, the band "MH$_{PCR}$" that appears in the gel is of the same size of the plasmid, which leads to believe that the heat from the NPs leads to the release of the plasmid to the outside of the cell wall. The absence of plasmid band in the negative controls (lanes labelled as "C-$_1$" and C-$_2$", respectively, with the same composition of "MH$_{PCR}$" and "Standard positive control") confirms that there is enough heat produced by the NPs for the release of the plasmid to occur. This may be from bacterial lysis. No product of amplification is seen. One hypothesis is that the amplification product ended up entangled with cell debris. So, MH assisted PCR was performed in the presence of only the pCMV-GFP plasmid[166], ordered from Addgene to simplify the reaction. These results, however, were quite different (**Figure 37B**). No band of amplification was seen but a very faint band (on the lane labelled "MH$_{PCR}$p") appeared close to the well. Because the plasmid concentration is so low (0.5 µg.mL^{-1}), it was not expected to see its band. And anyway, the base pairs of this product were much larger than those of the plasmid. Its exact constitution may not be possible to determine without sequencing, but the presence or absence of plasmid in this band was further tested.

To determine if nanoparticles, plasmid, amplification product and primers were entangled the same sample, MH$_{PCR}$p, was submitted to three conditions: 95 °C heat for 5 minutes, in hopes that DNA chains would be denaturated and separated; centrifugation at 14 000 rpm for 1 hour to

precipitate potential nanoparticles present; and the combination of the first two conditions in that order. The band still remained in the same place. Moreover, the unknown band as well as a sample of standard positive control were recovered and examined with a DNA extraction kit. Both samples extractions were used as DNA templates in a standard PCR reaction (same conditions as in section **2.7.7**). This assay, in **Figure 37C**, revealed that this band is neither composed of the plasmid nor the amplification band (lane "St$_{PCR2}$" and "MH$_{PCR2}$"). ImageJ gel analysis also confirmed what was visually concluded.
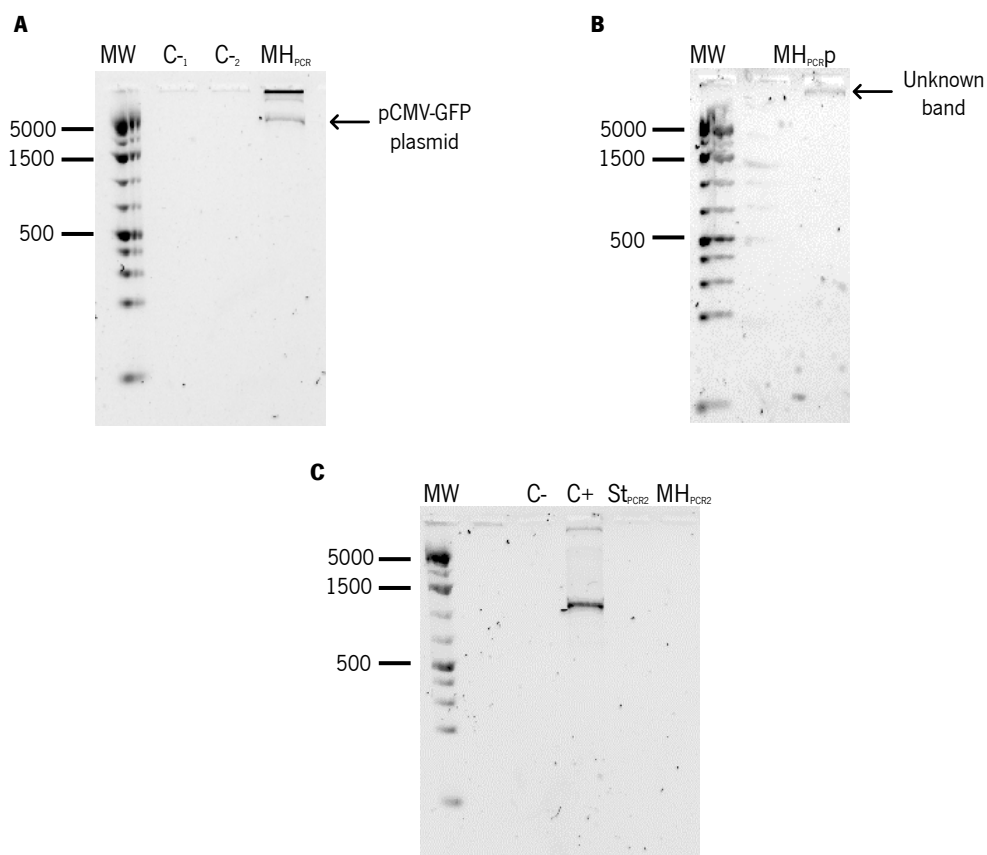
Figure 37. Electrophoresis gel run at 300 V for 60 min of **(A)** magnetic hyperthermia assisted PCR with Fe$_3$O$_4$@PAA -*Taq* and JM109 cells transfected with pCMV-GFP; **(B)** magnetic hyperthermia assisted PCR with Fe$_3$O$_4$@PAA-*Taq* and pCMV-GFP; and **(C)** assay on entanglement hypothesis. MW represents the lane containing the molecular weight ladder, "C-", "C-$_1$" and "C-$_2$" are negative controls of each experiment, "C+" is the positive control established as standard PCR control, MH$_{PCR}$, MH$_{PCR}$p, St$_{PCR2}$, and MH$_{PCR2}$ are the results of each experiment. Reference bands are detailed for easier examination (5000, 1500 and 500 bp). pCMV-GFP and unknow band are indicated by black arrows.

There were several different MH assisted PCR conditions tested, including varying the iron concentration (0.3 mg.mL^{-1}, 1.89 mg.mL^{-1}, 2.32 mg.mL^{-1}, 2.34 mg.mL^{-1}, 2.95 mg.mL^{-1}, 23.2 mg.mL^{-1}), using *Taq*-functionalized or non-functionalized nanoparticles, varying the times for each PCR phase (90s for each phase), omitting the step involving the temperature decreasing waiting period, performing the annealing phase with a water bath at 57 °C (instead of its magnetic induction), and different combinations of these modifications. All of which had the same unsuccessful outcome.

Even though MH assisted PCR amplification was not yet achieved, these results can be attributed to several facts. Discarding the possible entanglement between plasmid DNA and primers (as there is not plasmid DNA in the unknown band), the possibility that the melting temperature is not being exactly achieved on the surface of the nanoparticles or that the time to achieve 95, 57 or 72 °C is too slow is relevant. As mentioned, PCR is a very sensitive technique. Attempting to achieve those identical conditions in an unmanageable environment such as the one used, does come with certain disadvantages. Some aspects of the development of this project are uncontrollable, and negative results will merely lead to speculation until there is a more defined methodology with a defined, controlled environment.

CHAPTER FOUR:

CONCLUSIONS AND FUTURE PROSPECTS

CHAPTER FOUR: CONCLUSIONS AND FUTURE PROSPECTS

1. Conclusion

The inherent properties of magnetite nanoparticles, conjugated with selected DNA primers (for the GFP gene in the proposed proof-of-concept) and the enzyme *Taq polymerase* through specific stable covalent functionalization, have the potential for local *on demand* amplification of genetic material *in vivo*. In this project, *Taq*-functionalised magnetic Fe_3O_4@PAA nanoparticles were employed to externally control the amplification of genetic material.

Poly(acrylic) acid coated magnetite nanoparticles were successfully synthesised by the hydrothermal method for this project requirements. MNPs were functionalized via peptide coupling reaction with the thermostable enzyme *Taq* polymerase and EGFP forward and reverse primers. A ratio of 3 *Taq* polymerase proteins to 1 nanoparticle was achieved. However, a ratio of 25 primers to 1 nanoparticle was attempted, but not successful. Extensive physico-chemical and functional characterization was performed of the systems that seemed fit.

Magnetite great heating potential is explored throughout the project: the temperatures required for the specific phases of PCR are attained (95, 57 and 72 $^{\circ}$C). Yet, the macroscopic versus nanoscopic temperature still remained an obstacle in the accomplishment of proving the proof-of-concept. An *in vitro* evaluation of this system performance was studied in bacterial cells (*Escherichia coli*), revealing through MIC, internalization, and viability assays, the biocompatibility of the nanoparticles. High concentrations of these iron oxide nanoparticles would be required for growth inhibition of the bacteria cells. Internalization of nanoparticles in JM109 cells was sufficient. Viability assays with induced magnetic hyperthermia revealed an increase in viability with MH, unexpectedly.

Standard PCR reaction parameters were established. *Taq* polymerase retained 50.9 % its activity when functionalized. Moreover, MH assisted PCR cycles with JM109 cells (*E. coli*) transfected with pCMV-GFP plasmid or with only pCMV-GFP plasmid were performed, yet they were unsuccessful.

2. Future prospects

The size of the core of these nanoparticles should further been improved in order to augment the heating capacity of these nanoparticles, as well as the size distribution: a more homogenous size distribution leads to a collective response. Also, it would be ideal to functionalize

the primers onto the surface of the nanoparticles, completing the system with all biological components involved for the amplification.

Moreover, the greater issue in the development of this project was the determination of the surface temperature, when was only possible to measure the macroscopic temperature of the sample. The extensive characterization of the nanoscale temperature of the nanoparticles when subjected to determined fields and frequencies is a crucial aspect to the successfulness of this project. The only way to comment on what is happening with the reaction is with that information. Recently, Richardson, *et al.*, 2006[194], attempted to measure the temperature on the surface of gold nanoparticles through examination of power threshold for the melting process (of the ice they were imbedded in) with time-resolved Raman signal. Other methodologies were attempted to determine the surface temperature of nanoparticles[195,196] or even other materials[197].

Moreover, the simplification of the performance required by the nanoparticles could also facilitate in the continuation of this project. For example, loop-mediated isothermal amplification is an amplification technique that would be simpler to adjust temperature parameters, since amplification occurs at 65 °C without other specific temperatures.

It was not possible to develop this project enough to explore it on human cell lines. However, the effect of exteriorization of the plasmid (bacterial lysis) by the heat generated through magnetic hyperthermia application could be explored. Testing with different cells (other bacteria or fungi) to verify that this event is not particular to this *Escherichia coli* strain.

CHAPTER FIVE: BIBLIOGRAPGY

CHAPTER FIVE: BIBLIOGRAPHY

1. Cox, D. B. T., Platt, R. J. & Zhang, F. Therapeutic Genome Editing: Prospects and Challenges. *Nat. Med.* **21**, 121–131 (2015).
2. Human Gene Therapy for Rare Diseases. (2020).
3. What are CAR T cell therapy, RNA therapy, and other genetic therapies? *MedlinePlus* https://medlineplus.gov/genetics/understanding/therapy/othergenetictherapy/ (2022).
4. Jen, K.-Y. Gene Amplification. in *Brenner's Encyclopedia of Genetics* (eds. Maloy, S. & Hughes, K.) 171–172 (Academic Press, 2013). doi:10.1016/B978-0-12-374984-0.00582-9.
5. Albertson, D. G. Gene amplification in cancer. *Trends Genet.* **22**, 447–455 (2006).
6. Araki, Y., Hamafuji, T., Noguchi, C. & Shimizu, N. Efficient Recombinant Production in Mammalian Cells Using a Novel IR/MAR Gene Amplification Method. *PLOS ONE* **7**, e41787 (2012).
7. Lipscomb, M. L., Palomares, L. A., Hernández, V., Ramírez, O. T. & Kompala, D. S. Effect of Production Method and Gene Amplification on the Glycosylation Pattern of a Secreted Reporter Protein in CHO Cells. *Biotechnol. Prog.* **21**, 40–49 (2005).
8. Reller, L. B., Weinstein, M. P. & Petti, C. A. Detection and Identification of Microorganisms by Gene Amplification and Sequencing. *Clin. Infect. Dis.* **44**, 1108–1114 (2007).
9. Heselmeyer-Haddad, K. *et al.* Detection of Genomic Amplification of the Human Telomerase Gene (TERC) in Cytologic Specimens as a Genetic Test for the Diagnosis of Cervical Dysplasia. *Am. J. Pathol.* **163**, 1405–1416 (2003).
10. Alexandrov, A., Shu, M.-D. & Steitz, J. A. Fluorescence Amplification Method for Forward Genetic Discovery of Factors in Human mRNA Degradation. *Mol. Cell* **65**, 191–201 (2017).
11. Matsui, A., Ihara, T., Suda, H., Mikami, H. & Semba, K. Gene amplification: mechanisms and involvement in cancer. *Biomol. Concepts* **4**, 567–582 (2013).
12. Savelyeva, L. & Schwab, M. Amplification of oncogenes revisited: from expression profiling to clinical application. *Cancer Lett.* **167**, 115–123 (2001).
13. Hogarty, M. D. & Brodeur, G. M. Gene Amplification in Human Cancers: Biological and Clinical Significance. in *The Online Metabolic and Molecular Bases of Inherited Disease* (eds. Valle, D. L., Antonarakis, S., Ballabio, A., Beaudet, A. L. & Mitchell, G. A.) (McGraw-Hill Education, 2019).
14. Gonçalves, G. A. R. & Paiva, R. de M. A. Gene therapy: advances, challenges and perspectives. *Einstein* **15**, 369–375 (2017).
15. Alex, S. M. & Sharma, C. P. Nanomedicine for gene therapy. *Drug Deliv. Transl. Res.* **3**, 437–445 (2013).
16. Pathak, A., Vyas, S. P. & Gupta, K. C. Nano-vectors for efficient liver specific gene transfer. *Int. J. Nanomedicine* **3**, 31–49 (2008).
17. Pogue, R. E. *et al.* Rare genetic diseases: update on diagnosis, treatment and online resources. *Drug Discov. Today* **23**, 187–195 (2018).
18. Emery, D. W. Gene therapy for genetic diseases: On the horizon. *Clin. Appl. Immunol. Rev.* **4**, 411–422 (2004).
19. Wolfe, J. H. Gene Therapy in Large Animal Models of Human Genetic Diseases. *ILAR J. Natl. Res. Counc. Inst. Lab. Anim. Resour.* **50**, 107–111 (2009).
20. Coleman, W. B. & Tsongalis, G. J. Laboratory Approaches in Molecular Pathology—The Polymerase Chain Reaction. in *Diagnostic Molecular Pathology* 15–23 (Elsevier, 2017). doi:10.1016/B978-0-12-800886-7.00002-9.

21. Garibyan, L. & Avashia, N. Polymerase Chain Reaction. *J. Invest. Dermatol.* **133**, 1–4 (2013).

22. Higashi, T. *et al.* Nanomaterial-assisted PCR based on thermal generation from magnetic nanoparticles under high-frequency AC magnetic fields. *Chem. Phys. Lett.* **635**, 234–240 (2015).

23. Kambli, P. & Kelkar-Mane, V. Nanosized Fe3O4 an efficient PCR yield enhancer— Comparative study with Au, Ag nanoparticles. *Colloids Surf. B Biointerfaces* **141**, 546–552 (2016).

24. Woodman, M. E. Direct PCR of Intact Bacteria (Colony PCR). *Curr. Protoc. Microbiol.* **9**, 6 (2008).

25. Packeiser, H., Lim, C., Balagurunathan, B., Wu, J. & Zhao, H. An Extremely Simple and Effective Colony PCR Procedure for Bacteria, Yeasts, and Microalgae. *Appl. Biochem. Biotechnol.* **169**, 695–700 (2013).

26. Snapp, E. L. Fluorescent Proteins: A Cell Biologist's User Guide. *Trends Cell Biol.* **19**, 649– 655 (2009).

27. Kumar, A. & Kaur, J. Primer Based Approach for PCR Amplification of High GC Content Gene: Mycobacterium Gene as a Model. *Mol. Biol. Int.* **2014**, 937308 (2014).

28. Feynman, R. P. There's Plenty of Room at the Bottom. *Eng. Sci.* **XXIII**, 13 (1960).

29. Potočnik, J. Commission Recommendation of 18 October 2011 on the definition of nanomaterial. *Official Journal of the European Union* 38–40 (2011).

30. Magdolenova, Z. *et al.* Mechanisms of genotoxicity. A review of in vitro and in vivo studies with engineered nanoparticles. *Nanotoxicology* **8**, 233–278 (2014).

31. M.G., K., V, K. & F, H. History and Possible Uses of Nanomedicine Based on Nanoparticles and Nanotechnological Progress. *J. Nanomedicine Nanotechnol.* **06**, (2015).

32. Zdrojewicz, Z., Waracki, M., Bugaj, B., Pypno, D. & Cabała, K. Medical applications of nanotechnology. *Zastos. Nanotechnologii W Med.* **69**, 1196–1204 (2015).

33. Amiri, M., Salavati-Niasari, M. & Akbari, A. Magnetic nanocarriers: Evolution of spinel ferrites for medical applications. *Adv. Colloid Interface Sci.* **265**, 29–44 (2019).

34. Boulaiz, H. *et al.* Nanomedicine: Application Areas and Development Prospects. *Int. J. Mol. Sci.* **12**, 3303–3321 (2011).

35. Plaseska-Karanfilska, D. *Human Genetic Diseases*. (InTech, 2011).

36. Riehemann, K. *et al.* Nanomedicine-Challenge and Perspectives. *Angew. Chem. Int. Ed.* **48**, 872–897 (2009).

37. Shubayev, V. I., Pisanic, T. R. & Jin, S. Magnetic nanoparticles for theragnostics. *Adv. Drug Deliv. Rev.* **61**, 467–477 (2009).

38. Yigit, M. V., Moore, A. & Medarova, Z. Magnetic Nanoparticles for Cancer Diagnosis and Therapy. *Pharm. Res.* **29**, 1180–1188 (2012).

39. Fraga García, P. *et al.* High-gradient magnetic separation for technical scale protein recovery using low cost magnetic nanoparticles. *Sep. Purif. Technol.* **150**, 29–36 (2015).

40. Zhang, B. *et al.* Preparation of highly fluorescent magnetic nanoparticles for analytes-enrichment and subsequent biodetection. *J. Colloid Interface Sci.* **353**, 426–432 (2011).

41. Trang, T. N. Q., Vinh, L. Q., Doanh, T. T. & Thu, V. T. H. Structure-adjustable colloidal silver nanoparticles on polymers grafted cellulose paper-based highly sensitive and selective SERS sensing platform with analyte enrichment function. *J. Alloys Compd.* **867**, 159158 (2021).

42. Gloag, L., Mehdipour, M., Chen, D., Tilley, R. D. & Gooding, J. J. Advances in the Application of Magnetic Nanoparticles for Sensing. *Adv. Mater.* **31**, 1904385 (2019).

43. Sinatra, F. Understanding the Interaction Between Blood Flow and an Applied Magnetic Field. (University of South Florida, 2010).

44. Issa, B., Obaidat, I., Albiss, B. & Haik, Y. Magnetic Nanoparticles: Surface Effects and Properties Related to Biomedicine Applications. *Int. J. Mol. Sci.* **14**, 21266–21305 (2013).

45. Kittel, C. Physical Theory of Ferromagnetic Domains. *Rev. Mod. Phys.* **21**, 541–583 (1949).

46. Bean, C. P. & Livingston, J. D. Superparamagnetism. *J. Appl. Phys.* **30**, S120–S129 (1959).

47. Kefeni, K. K., Msagati, T. A. M., Nkambule, T. TI. & Mamba, B. B. Spinel ferrite nanoparticles and nanocomposites for biomedical applications and their toxicity. *Mater. Sci. Eng. C* **107**, 110314 (2020).

48. Wallyn, J., Anton, N. & Vandamme, T. F. Synthesis, Principles, and Properties of Magnetite Nanoparticles for In Vivo Imaging Applications—A Review. *Pharmaceutics* **11**, 601 (2019).

49. Akbarzadeh, A., Samiei, M. & Davaran, S. Magnetic nanoparticles: Preparation, physical properties, and applications in biomedicine. *Nanoscale Res. Lett.* **7**, 144 (2012).

50. Bean, C. P. & Livingston, J. D. Superparamagnetism. *J. Appl. Phys.* **30**, 120S-129S (2016).

51. Sahoo, B. *et al.* Biocompatible mesoporous silica-coated superparamagnetic manganese ferrite nanoparticles for targeted drug delivery and MR imaging applications. *J. Colloid Interface Sci.* **431**, 31–41 (2014).

52. Weller, D. & Doerner, M. F. Extremely High-Density Longitudinal Magnetic Recording Media. *Annu. Rev. Mater. Sci.* **30**, 611–644 (2000).

53. Moyano, A. *et al.* Carbon-Coated Superparamagnetic Nanoflowers for Biosensors Based on Lateral Flow Immunoassays. *Biosensors* **10**, 80 (2020).

54. Dai, J. *et al.* Magnetic coupling induced increase in the blocking temperature of γ-Fe2O3 nanoparticles. *J. Appl. Phys.* **87**, 7397–7399 (2000).

55. Petracic, O. Superparamagnetic nanoparticle ensembles. *Superlattices Microstruct.* **47**, 569–578 (2010).

56. Bruvera, I. J., Mendoza Zélis, P., Pilar Calatayud, M., Goya, G. F. & Sánchez, F. H. Determination of the blocking temperature of magnetic nanoparticles: The good, the bad, and the ugly. *J. Appl. Phys.* **118**, 184304 (2015).

57. Majetich, S., Wen, T. & Mefford, O. Magnetic Nanoparticles. *MRS Bull. Mater. Res. Soc.* **38**, 899–903 (2013).

58. Caldorera-Moore, M., Guimard, N., Shi, L. & Roy, K. Designer nanoparticles: Incorporating size, shape, and triggered release into nanoscale drug carriers. *Expert Opin. Drug Deliv.* **7**, 479–495 (2010).

59. Wu, W., Wu, Z., Yu, T., Jiang, C. & Kim, W.-S. Recent progress on magnetic iron oxide nanoparticles: synthesis, surface functional strategies and biomedical applications. *Sci. Technol. Adv. Mater.* **16**, 023501 (2015).

60. Zahmatkesh, I. *et al.* Effect of nanoparticle shape on the performance of thermal systems utilizing nanofluids: A critical review. *J. Mol. Liq.* **321**, 114430 (2021).

61. Jo, D. H., Kim, J. H., Lee, T. G. & Kim, J. H. Size, surface charge, and shape determine therapeutic effects of nanoparticles on brain and retinal diseases. *Nanomedicine Nanotechnol. Biol. Med.* **11**, 1603–1611 (2015).

62. Krishnan, K. M. Biomedical Nanomagnetics: A Spin Through Possibilities in Imaging, Diagnostics, and Therapy. *IEEE Trans. Magn.* **46**, 2523–2558 (2010).

63. Peigneux, A. *et al.* Functionalized Biomimetic Magnetic Nanoparticles as Effective Nanocarriers for Targeted Chemotherapy. *Part. Part. Syst. Charact.* **36**, 1900057 (2019).

64. Singh, R. & Lillard, J. W. Nanoparticle-based targeted drug delivery. *Exp. Mol. Pathol.* **86**, 215–223 (2009).

65. Majewski, P. & Thierry, B. Functionalized Magnetite Nanoparticles—Synthesis, Properties, and Bio-Applications. *Crit. Rev. Solid State Mater. Sci.* **32**, 203–215 (2007).

66. Stephen, Z. R., Kievit, F. M. & Zhang, M. Magnetite nanoparticles for medical MR imaging. *Mater. Today* **14**, 330–338 (2011).

67. Johannsen, M. *et al.* Termoterapia en cáncer de próstata mediante el uso de nanopartículas magnéticas. *Actas Urol. Esp.* **31**, 660–667 (2007).

68. Sachdev, J. C. *et al.* Phase I study of liposomal irinotecan in patients with metastatic breast cancer: findings from the expansion phase. *Breast Cancer Res. Treat.* **185**, 759–771 (2021).

69. Whittle, J. R. *et al.* First in human nanotechnology doxorubicin delivery system to target epidermal growth factor receptors in recurrent glioblastoma. *J. Clin. Neurosci.* **22**, 1889–1894 (2015).

70. Tiquia-Arashiro, S. & Rodrigues, D. Nanoparticles Synthesized by Microorganisms. in 1–51 (2016). doi:10.1007/978-3-319-45215-9_1.

71. Thiruppathi, R., Mishra, S., Ganapathy, M., Padmanabhan, P. & Gulyás, B. Nanoparticle Functionalization and Its Potentials for Molecular Imaging. *Adv. Sci.* **4**, 1600279 (2017).

72. Malhotra, N. *et al.* Potential Toxicity of Iron Oxide Magnetic Nanoparticles: A Review. *Molecules* **25**, 3159 (2020).

73. Kumar, P., Agnihotri, S. & Roy, I. Preparation and characterization of superparamagnetic iron oxide nanoparticles for magnetically guided drug delivery. *Int. J. Nanomedicine* **13**, 43–46 (2018).

74. Olsvik, O. *et al.* Magnetic separation techniques in diagnostic microbiology. *Clin. Microbiol. Rev.* **7**, 43–54 (1994).

75. Germano, J. *et al.* A Portable and Autonomous Magnetic Detection Platform for Biosensing. *Sensors* **9**, 4119–4137 (2009).

76. Fernandes, A. C. *et al.* Lab-on-Chip Cytometry Based on Magnetoresistive Sensors for Bacteria Detection in Milk. *Sensors* **14**, 15496–15524 (2014).

77. Tay, Z. W. *et al.* Magnetic Particle Imaging-Guided Heating in Vivo Using Gradient Fields for Arbitrary Localization of Magnetic Hyperthermia Therapy. *ACS Nano* **12**, 3699–3713 (2018).

78. Desforges, J. F. & Simon, H. B. Hyperthermia. *N. Engl. J. Med.* **329**, 483–487 (1993).

79. Lepock, J. R. Cellular effects of hyperthermia: relevance to the minimum dose for thermal damage. *Int. J. Hyperthermia* **19**, 252–266 (2003).

80. Revia, R. A. & Zhang, M. Magnetite nanoparticles for cancer diagnosis, treatment, and treatment monitoring: recent advances. *Mater. Today* **19**, 157–168 (2016).

81. Tombácz, E., Csanaky, C. & Illés, E. Polydisperse fractal aggregate formation in clay mineral and iron oxide suspensions, pH and ionic strength dependence. *Colloid Polym. Sci.* **279**, 484–492 (2001).

82. Pankhurst, Q. A., Connolly, J., Jones, S. K. & Dobson, J. Applications of magnetic nanoparticles in biomedicine. *J. Phys. Appl. Phys.* **36**, R167–R181 (2003).

83. M. H. Falk, R. D. I. Hyperthermia in oncology. *Int. J. Hyperthermia* **17**, 1–18 (2001).

84. Koo, K. N., Ismail, A. F., Othman, M. H. D., Bidin, N. & A Rahman, M. Preparation and characterization of superparamagnetic magnetite (Fe3O4) nanoparticles: A short review. *Malays. J. Fundam. Appl. Sci.* **15**, 23–31 (2019).

85. Laurent, S., Dutz, S., Häfeli, U. O. & Mahmoudi, M. Magnetic fluid hyperthermia: Focus on superparamagnetic iron oxide nanoparticles. *Adv. Colloid Interface Sci.* **166**, 8–23 (2011).

86. de Châtel, P. F., Nandori, I., Hakl, J., Mészáros, S. & Vad, K. Magnetic particle hyperthermia: Neel relaxation in magnetic nanoparticles under circularly polarized field. *J. Phys. Condens. Matter* **21**, 124202 (2009).

87. Nemati, Z. *et al.* Enhanced Magnetic Hyperthermia in Iron Oxide Nano-Octopods: Size and Anisotropy Effects. *J. Phys. Chem. C* **120**, 8370–8379 (2016).

88. Deatsch, A. E. & Evans, B. A. Heating efficiency in magnetic nanoparticle hyperthermia. *J. Magn. Magn. Mater.* **354**, 163–172 (2014).

89. Magnetic Resonance Imaging (MRI). *National Institutes of Health (NIH)* https://www.nibib.nih.gov/science-education/science-topics/magnetic-resonance-imaging-mri (2022).

90. Brito, B., Price, T. W., Gallo, J., Bañobre-López, M. & Stasiuk, G. J. Smart magnetic resonance imaging-based theranostics for cancer. *Theranostics* **11**, 8706–8737 (2021).

91. Hendrick, R. E. *Breast MRI: fundamentals and technical aspects*. (Springer, 2008).

92. van Geuns, R.-J. M. *et al.* Basic principles of magnetic resonance imaging. *Prog. Cardiovasc. Dis.* **42**, 149–156 (1999).

93. Katti, G., Ara, S. A. & Shireen, A. Magnetic Resonance Imaging (MRI) – A Review. *Intenational J. Dent. Clin.* **3**, 7 (2011).

94. Wahsner, J., Gale, E. M., Rodríguez-Rodríguez, A. & Caravan, P. Chemistry of MRI Contrast Agents: Current Challenges and New Frontiers. *Chem. Rev.* **119**, 957–1057 (2019).

95. Nelson, N. R., Port, J. D. & Pandey, M. K. Use of Superparamagnetic Iron Oxide Nanoparticles (SPIONs) via Multiple Imaging Modalities and Modifications to Reduce Cytotoxicity: An Educational Review. *J. Nanotheranostics* **1**, 105–135 (2020).

96. Neuwelt, A. *et al.* Iron-Based Superparamagnetic Nanoparticle Contrast Agents for MRI of Infection and Inflammation. *AJR Am. J. Roentgenol.* **204**, W302–W313 (2015).

97. Thorat, N. D. *et al.* Physically stimulated nanotheranostics for next generation cancer therapy: Focus on magnetic and light stimulations. *Appl. Phys. Rev.* **6**, 041306 (2019).

98. Jin, R., Lin, B., Li, D. & Ai, H. Superparamagnetic iron oxide nanoparticles for MR imaging and therapy: design considerations and clinical applications. *Curr. Opin. Pharmacol.* **18**, 18–27 (2014).

99. Zhou, Y., Peng, Z., Seven, E. S. & Leblanc, R. M. Crossing the blood-brain barrier with nanoparticles. *J. Controlled Release* **270**, 290–303 (2018).

100. Kim, Y.-R. *et al.* Toxicity of 100 nm zinc oxide nanoparticles: a report of 90-day repeated oral administration in Sprague Dawley rats. *Int. J. Nanomedicine* **9**, 109–126 (2014).

101. Hong, T.-K. *et al.* A comprehensive in vitro and in vivo study of ZnO nanoparticles toxicity. *J. Mater. Chem. B* **1**, 2985–2992 (2013).

102. Khalili Fard, J., Jafari, S. & Eghbal, M. A. A Review of Molecular Mechanisms Involved in Toxicity of Nanoparticles. *Adv. Pharm. Bull.* **5**, 447–454 (2015).

103. Ma, Y. *et al.* A review of the application of nanoparticles in the diagnosis and treatment of chronic kidney disease. *Bioact. Mater.* **5**, 732–743 (2020).

104. Ali, A. *et al.* Synthesis, characterization, applications, and challenges of iron oxide nanoparticles. *Nanotechnol. Sci. Appl.* **9**, 49–67 (2016).

105. Ma, J., Ming-Yuen Lee, S., Yi, C. & Li, C.-W. Controllable synthesis of functional nanoparticles by microfluidic platforms for biomedical applications – a review. *Lab. Chip* **17**, 209–226 (2017).

106. Justin, C., Philip, S. A. & Samrot, A. V. Synthesis and characterization of superparamagnetic iron-oxide nanoparticles (SPIONs) and utilization of SPIONs in X-ray imaging. *Appl. Nanosci.* **7**, 463–475 (2017).

107. Baumgartner, J. *et al.* Nucleation and growth of magnetite from solution. *Nat. Mater.* **12**, 310–314 (2013).

108. Li, J., Wu, Q. & Wu, J. Synthesis of Nanoparticles via Solvothermal and Hydrothermal Methods. in *Handbook of Nanoparticles* (ed. Aliofkhazraei, M.) 295–328 (Springer International Publishing, 2016). doi:10.1007/978-3-319-15338-4_17.

109. Thanh, N. T. K., Maclean, N. & Mahiddine, S. Mechanisms of Nucleation and Growth of Nanoparticles in Solution. *Chem. Rev.* **114**, 7610–7630 (2014).

110. Babooram, K. 28 - Novel solution routes to ferroelectrics and relaxors. in *Handbook of Advanced Dielectric, Piezoelectric and Ferroelectric Materials* (ed. Ye, Z.-G.) 852–883 (Woodhead Publishing, 2008). doi:10.1533/9781845694005.7.852.

111. Dembski, S., Schneider, C., Christ, B. & Retter, M. 5 - Core-shell nanoparticles and their use for in vitro and in vivo diagnostics. in *Core-Shell Nanostructures for Drug Delivery and Theranostics* (eds. Focarete, M. L. & Tampieri, A.) 119–141 (Woodhead Publishing, 2018). doi:10.1016/B978-0-08-102198-9.00005-3.

112. Nawaz, M. *et al.* 2 - Magnetic and pH-responsive magnetic nanocarriers. in *Stimuli Responsive Polymeric Nanocarriers for Drug Delivery Applications* (eds. Makhlouf, A. S. H. & Abu-Thabit, N. Y.) 37–85 (Woodhead Publishing, 2019). doi:10.1016/B978-0-08-101995-5.00002-7.

113. Yusoff, A. H. M., Salimi, M. N. & Jamlos, M. A review: Synthetic strategy control of magnetite nanoparticles production. *Adv. Nano Res.* **6**, 1–19 (2018).

114. Ealia, S. A. M. & Saravanakumar, M. P. A review on the classification, characterisation, synthesis of nanoparticles and their application. *IOP Conf. Ser. Mater. Sci. Eng.* **263**, 032019 (2017).

115. Odularu, A. T. Metal Nanoparticles: Thermal Decomposition, Biomedicinal Applications to Cancer Treatment, and Future Perspectives. *Bioinorg. Chem. Appl.* **2018**, 9354708 (2018).

116. Toyos-Rodríguez, C. *et al.* A Simple and Reliable Synthesis of Superparamagnetic Magnetite Nanoparticles by Thermal Decomposition of Fe(acac)3. *J. Nanomater.* **2019**, e2464010 (2019).

117. Campos, E. A., Pinto, D. V. B. S., Oliveira, J. I. S. de, Mattos, E. da C. & Dutra, R. de C. L. Synthesis, Characterization and Applications of Iron Oxide Nanoparticles - a Short Review. *J. Aerosp. Technol. Manag.* **7**, 267–276 (2015).

118. V. Nikam, A., V. Prasad, B. L. & A. Kulkarni, A. Wet chemical synthesis of metal oxide nanoparticles: a review. *CrystEngComm* **20**, 5091–5107 (2018).

119. Niculescu, A.-G., Chircov, C. & Grumezescu, A. M. Magnetite nanoparticles: Synthesis methods – A comparative review. *Methods* **199**, 16–27 (2022).

120. Haw, C. Y. *et al.* Hydrothermal synthesis of magnetite nanoparticles as MRI contrast agents. *Ceram. Int.* **36**, 1417–1422 (2010).

121. Daou, T. J. *et al.* Hydrothermal Synthesis of Monodisperse Magnetite Nanoparticles. *Chem. Mater.* **18**, 4399–4404 (2006).

122. Torres-Gómez, N. *et al.* Shape Tuning of Magnetite Nanoparticles Obtained by Hydrothermal Synthesis: Effect of Temperature. *J. Nanomater.* **2019**, e7921273 (2019).

123. Yang, G. & Park, S.-J. Conventional and Microwave Hydrothermal Synthesis and Application of Functional Materials: A Review. *Materials* **12**, 1177 (2019).

124. Gulati, S., Sachdeva, M. & Bhasin, K. K. Capping agents in nanoparticle synthesis: Surfactant and solvent system. in 030214 (2018). doi:10.1063/1.5032549.

125. Javed, R. *et al.* Role of capping agents in the application of nanoparticles in biomedicine and environmental remediation: recent trends and future prospects. *J. Nanobiotechnology* **18**, 172 (2020).

126. Küçükdermenci, S., Kutluay, D. & Avgin, I. Synthesis of a Fe3O4/paa-based magnetic fluid for Faraday-rotation measurements. *Mater. Tehnol.* **47**, 71–78 (2012).

127. Xu, Y., Zhuang, L., Lin, H., Shen, H. & Li, J. W. Preparation and characterization of polyacrylic acid coated magnetite nanoparticles functionalized with amino acids. *Thin Solid Films* **544**, 368–373 (2013).

128. Lin, C.-L., Lee, C.-F. & Chiu, W.-Y. Preparation and properties of poly(acrylic acid) oligomer stabilized superparamagnetic ferrofluid. *J. Colloid Interface Sci.* **291**, 411–420 (2005).

129. Terao, K. Poly(acrylic acid) (PAA). in *Encyclopedia of Polymeric Nanomaterials* (eds. Kobayashi, S. & Müllen, K.) 1–6 (Springer Berlin Heidelberg, 2021). doi:10.1007/978-3-642-36199-9_279-1.

130. Piñeiro-Redondo, Y. *et al.* The influence of colloidal parameters on the specific power absorption of PAA-coated magnetite nanoparticles. *Nanoscale Res. Lett.* **6**, 383 (2011).

131. Mizutani, N. *et al.* Effect of ferrous/ferric ions molar ratio on reaction mechanism for hydrothermal synthesis of magnetite nanoparticles. *Bull. Mater. Sci.* **31**, 713–717 (2008).

132. Ozel, F., Kockar, H. & Karaagac, O. Growth of Iron Oxide Nanoparticles by Hydrothermal Process: Effect of Reaction Parameters on the Nanoparticle Size. *J. Supercond. Nov. Magn.* **28**, 823–829 (2015).

133. Panáček, A. *et al.* Polyacrylate-Assisted Size Control of Silver Nanoparticles and Their Catalytic Activity. *Chem. Mater.* **26**, 1332–1339 (2014).

134. Dang, M. C., Huynh, K. K. & Dang, D. M. T. Synthesis of Silver Nanoparticles Using Poly(acrylic acid) as a Capping Agent for Conductive Ink in Inkjet Printing Application. *Biol. Chem. Res.* **6**, 111–119 (2019).

135. Kumar, P. *et al.* Temperature selectivity for single phase hydrothermal synthesis of PEG-400 coated magnetite nanoparticles. *Dalton Trans.* **49**, 8672–8683 (2020).

136. Bartczak, D. & Kanaras, A. G. Preparation of Peptide-Functionalized Gold Nanoparticles Using One Pot EDC/Sulfo-NHS Coupling. *Langmuir* **27**, 10119–10123 (2011).

137. Schmid, F.-X. Biological Macromolecules: UV-visible Spectrophotometry. in *Encyclopedia of Life Sciences* (ed. John Wiley & Sons, Ltd) a0003142 (John Wiley & Sons, Ltd, 2001). doi:10.1038/npg.els.0003142.

138. Swinehart, D. F. The Beer-Lambert Law. *J. Chem. Educ.* **39**, 333 (1962).

139. Sawant, S. D., Baravkar, A. A. & Kale, R. N. FT-IR SPECTROSCOPY: PRINCIPLE, TECHNIQUE AND MATHEMATICS. *Int. J. Pharma Bio Sci.* **2**, 513–519 (2011).

140. Gaffney, J. S., Marley, N. A. & Jones, D. E. Fourier Transform Infrared (FTIR) Spectroscopy. in *Characterization of Materials* (ed. Kaufmann, E. N.) 32 (John Wiley & Sons, Inc., 2012). doi:10.1002/0471266965.com107.pub2.

141. Tang, C. Y. & Yang, Z. Transmission Electron Microscopy (TEM). in *Membrane Characterization* 145–159 (Elsevier, 2017). doi:10.1016/B978-0-444-63776-5.00008-5.

142. Reimer, L. *Transmission Electron Microscopy: Physics of Image Formation and Microanalysis*. vol. 36 (Springer Berlin Heidelberg, 2013).

143. Verleysen, E. *et al.* Evaluation of a TEM based Approach for Size Measurement of Particulate (Nano)materials. *Materials* **12**, 2274 (2019).

144. Michalke, B. & Nischwitz, V. Speciation and Element-Specific Detection. in *Liquid Chromatography* 633–649 (Elsevier, 2013). doi:10.1016/B978-0-12-415806-1.00022-X.

145. Weeks, E. R. & Semwogerere, D. Confocal MIcroscopy. in *Confocal Microscopy* (Encyclopedia of Biomaterials and Biomedical Engineering, 2008).

146. Nwaneshiudu, A. *et al.* Introduction to confocal microscopy. *J. Invest. Dermatol.* **132**, 1–5 (2012).

147. Bhattacharjee, S. DLS and zeta potential – What they are and what they are not? *J. Controlled Release* **235**, 337–351 (2016).

148. Joseph, E. & Singhvi, G. Multifunctional nanocrystals for cancer therapy: a potential nanocarrier. in *Nanomaterials for Drug Delivery and Therapy* 91–116 (Elsevier, 2019). doi:10.1016/B978-0-12-816505-8.00007-2.

149. McNeil-Watson, F. Electrophoretic Light Scattering. in *Encyclopedia of Biophysics* (ed. Roberts, G. C. K.) 648–654 (Springer Berlin Heidelberg, 2013). doi:10.1007/978-3-642-16712-6_288.

150. Clogston, J. D. & Patri, A. K. Zeta Potential Measurement. in *Characterization of Nanoparticles Intended for Drug Delivery* (ed. McNeil, S. E.) vol. 697 63–70 (Humana Press, 2011).

151. Rami, J. M., Patel, C. D., Patel, C. M. & Patel, M. V. Thermogravimetric analysis (TGA) of some synthesized metal oxide nanoparticles. *Mater. Today Proc.* **43**, 655–659 (2021).

152. Saadatkhah, N. *et al.* Experimental methods in chemical engineering: Thermogravimetric analysis—TGA. *Can. J. Chem. Eng.* **98**, 34–43 (2020).

153. Vyazovkin, S. Thermogravimetric Analysis. in *Characterization of Materials* (ed. Kaufmann, E. N.) com029.pub2 (John Wiley & Sons, Inc., 2012). doi:10.1002/0471266965.com029.pub2.

154. Jenks, W. G., Sadeghi, S. S. H. & Wikswo, J. P. SQUIDs for nondestructive evaluation. *J. Phys. Appl. Phys.* **30**, 293–323 (1997).

155. Weinstock, H. A review of SQUID magnetometry applied to nondestructive evaluation. *IEEE Trans. Magn.* **27**, 3231–3236 (1991).

156. Lenz, J. E. A review of magnetic sensors. *Proc. IEEE* **78**, 973–989 (1990).

157. Kraft, A., Rupprecht, C. & Yam, Y.-C. Superconducting Quantum Interference Device. *UBC Phys.* 6 (2017).

158. Tóth, É., Helm, L. & Merbach, A. E. Relaxivity of MRI Contrast Agents. in *Contrast Agents I: Magnetic Resonance Imaging* (ed. Krause, W.) 61–101 (Springer, 2002). doi:10.1007/3-540-45733-X_3.

159. Mandal, D. Ultra-thin films of a ferroelectric copolymer: P(VDF-TrFE). (LAMBERT Academic Publisher, 2012).

160. Epp, J. X-ray diffraction (XRD) techniques for materials characterization. in *Materials Characterization Using Nondestructive Evaluation (NDE) Methods* 81–124 (Elsevier, 2016). doi:10.1016/B978-0-08-100040-3.00004-3.

161. Sima, F. *et al.* Laser thin films deposition and characterization for biomedical applications. in *Laser Surface Modification of Biomaterials* 77–125 (Elsevier, 2016). doi:10.1016/B978-0-08-100883-6.00003-4.

162. Périgo, E. A. *et al.* Fundamentals and advances in magnetic hyperthermia. *Appl. Phys. Rev.* **2**, 041302 (2015).

163. Wu, K. & Wang, J.-P. Magnetic hyperthermia performance of magnetite nanoparticle assemblies under different driving fields. *AIP Adv.* **7**, 056327 (2017).

164. Brezovich, I. Low frequency hyperthermia: Capacitive and ferromagnetic thermoseed methods. *Med. Phys. Monogr.* **16**, 82–111 (1988).

165. Bañobre-López, M., Piñeiro, Y., López-Quintela, M. A. & Rivas, J. Magnetic Nanoparticles for Biomedical Applications. in *Handbook of Nanomaterials Properties* (eds. Bhushan, B., Luo, D., Schricker, S. R., Sigmund, W. & Zauscher, S.) 457–493 (Springer Berlin Heidelberg, 2014). doi:10.1007/978-3-642-31107-9_29.

166. Matsuda, T. & Cepko, C. L. Electroporation and RNA interference in the rodent retina in vivo and in vitro. *Proc. Natl. Acad. Sci.* **101**, 16–22 (2004).

167. Silva, M. D., Oliveira, H., Faustino, A. & Sillankorva, S. Characterization of MSlys, the endolysin of Streptococcus pneumoniae phage MS1. *Biotechnol. Rep.* **28**, e00547 (2020).

168. Dalai, S. *et al.* Studies on interfacial interactions of TiO2 nanoparticles with bacterial cells under light and dark conditions. *Bull. Mater. Sci.* **37**, 371–381 (2014).

169. Antiabong, J. F., Ngoepe, M. G. & Abechi, A. S. Semi-quantitative digital analysis of polymerase chain reaction-electrophoresis gel: Potential applications in low-income veterinary laboratories. *Vet. World* **9**, 935–939 (2016).

170. Takechi-Haraya, Y. *et al.* Current Status and Challenges of Analytical Methods for Evaluation of Size and Surface Modification of Nanoparticle-Based Drug Formulations. *AAPS PharmSciTech* **23**, 150 (2022).

171. Mudalige, T. *et al.* Characterization of Nanomaterials. in *Nanomaterials for Food Applications* 313–353 (Elsevier, 2019). doi:10.1016/B978-0-12-814130-4.00011-7.

172. Khandhar, A. P., Ferguson, R. M., Simon, J. A. & Krishnan, K. M. Enhancing cancer therapeutics using size-optimized magnetic fluid hyperthermia. *J. Appl. Phys.* **111**, 07B306-07B306-3 (2012).

173. L. Silva, P. *et al.* Mapping intracellular thermal response of cancer cells to magnetic hyperthermia treatment. *Nanoscale* **12**, 21647–21656 (2020).

174. Grabowska, B. & Holtzer, M. Structural examination of the cross-linking reaction mechanism of polyacrylate binding agents. *Arch. Metall. Mater.* **54**, 427–437 (2009).

175. Marius, C., Banica, R., Ieta, A. & Grozescu, I. Superparamagnetic Unusual Behavior of Micrometric Magnetite Monodisperse Monocrystals Synthesized by Fe-EDTA Thermal Decomposition. *Part. Sci. Technol. - Part. SCI Technol.* **30**, (2012).

176. Gehring, A. U., Fischer, H., Charilaou, M. & García-Rubio, I. Magnetic anisotropy and Verwey transition of magnetosome chains in Magnetospirillum gryphiswaldense. *Geophys. J. Int.* **187**, 1215–1221 (2011).

177. Buschow, K. H. J. *Handbook of magnetic materials*. vol. 8 (Elsevier, 1195).

178. Cornell, R. M. & Schwertmann, U. *The iron oxides: structure, properties, reactions, occurrences, and uses*. (Wiley-VCH, 2003).

179. Colombo, M. *et al.* Biological applications of magnetic nanoparticles. *Chem. Soc. Rev.* **41**, 4306–4334 (2012).

180. Batlle, X. *et al.* Magnetite nanoparticles with almost bulk magnetic properties: the role of the surfactant. (2007).

181. Reimer, P. & Balzer, T. Ferucarbotran (Resovist): a new clinically approved RES-specific contrast agent for contrast-enhanced MRI of the liver: properties, clinical development, and applications. *Eur. Radiol.* **13**, 1266–1276 (2003).

182. Farzadniya, A., Faeghi, F. & Shanehsazzadeh, S. Quantitative Effect of Magnetic Field Strength on PEGylated Superparamagnetic Iron Oxide Nanoparticles. *Appl. Magn. Reson.* **48**, 597–607 (2017).

183. Bryant, R. G., Mendelson, D. A. & Lester, C. C. The magnetic field dependence of proton spin relaxation in tissues. *Magn. Reson. Med.* **21**, 117–126 (1991).

184. Rohrer, M., Bauer, H., Mintorovitch, J., Requardt, M. & Weinmann, H.-J. Comparison of Magnetic Properties of MRI Contrast Media Solutions at Different Magnetic Field Strengths. *Invest. Radiol.* **40**, 715–724 (2005).

185. Adolphi, N. *et al.* Characterization of magnetite nanoparticles for SQUID-relaxometry and magnetic needle biopsy. *J. Magn. Magn. Mater.* **321**, 1459–1464 (2009).

186. Zhou, Z., Yang, L., Gao, J. & Chen, X. Structure–Relaxivity Relationships of Magnetic Nanoparticles for Magnetic Resonance Imaging. *Adv. Mater.* **31**, 1804567 (2019).

187. Nandwana, V. *et al.* Theranostic Magnetic Nanostructures (MNS) for Cancer. *Cancer Treat. Res.* **166**, 51–83 (2015).

188. Meuer, S., Wittwer, C. & Nakagawara, K. *Rapid Cycle Real-Time PCR: Methods and Applications*. (Springer Science & Business Media, 2012).

189. Lazarevic, A., Pokrajac, D., Marcano Olaizola, A. & Melikechi, N. Support vector machine based classification of fast Fourier transform spectroscopy of proteins. in *Advanced Biomedical and Clinical Diagnostic Systems VII* vol. 7169 63–70 (SPIE, 2009).

190. Tang, I.-M., Krishnamra, N., Charoenphandhu, N., Hoonsawat, R. & Pon-On, W. Biomagnetic of Apatite-Coated Cobalt Ferrite: A Core–Shell Particle for Protein Adsorption and pH-Controlled Release. *Nanoscale Res. Lett.* **6**, (2011).

191. Retnakumari, A. *et al.* Molecular-receptor-specific, non-toxic, near-infrared-emitting Au cluster-protein nanoconjugates for targeted cancer imaging. *Nanotechnology* **21**, 055103 (2009).

192. Abdul-Tehrani, H. *et al.* Ferritin Mutants of Escherichia coli Are Iron Deficient and Growth Impaired, and fur Mutants are Iron Deficient. *J. Bacteriol.* **181**, 1415–1428 (1999).

193. Slavin, Y. N., Asnis, J., Häfeli, U. O. & Bach, H. Metal nanoparticles: understanding the mechanisms behind antibacterial activity. *J. Nanobiotechnology* **15**, 65 (2017).

194. Richardson, H. H. *et al.* Thermooptical Properties of Gold Nanoparticles Embedded in Ice: Characterization of Heat Generation and Melting. *Nano Lett.* **6**, 783–788 (2006).

195. Lee, J., Govorov, A. O. & Kotov, N. A. Nanoparticle Assemblies with Molecular Springs: A Nanoscale Thermometer. *Angew. Chem. Int. Ed.* **44**, 7439–7442 (2005).

196. Carlson, M. T., Khan, A. & Richardson, H. H. Local Temperature Determination of Optically Excited Nanoparticles and Nanodots. *Nano Lett.* **11**, 1061–1069 (2011).

197. Fischer, L. H., Harms, G. S. & Wolfbeis, O. S. Upconverting Nanoparticles for Nanoscale Thermometry. *Angew. Chem. Int. Ed.* **50**, 4546–4551 (2011).

CHAPTER SIX: ANNEXES

CHAPTER SIX: ANNEXES

Annex 1: pCMV-GFP sequence with underlined selected primers annealing region and green identified amplified region.

5'-ctagtaatagtaatcaattacggggtcattagttcatagcccatatatggagttccgcgttacataacttacggtaaatggcccgcctggct

gaccgcccaacgacccccgcccattgacgtcaataatgacgtatgttcccatagtaacgccaatagggactttccattgacgtcaatgggtg

gagtatttacggtaaactgcccacttggcagtacatcaagtgtatcatatgccaagtacgccccctattgacgtcaatgacggtaaatggccc

gcctggcattatgcccagtacatgaccttatgggactttcctacttggcagtacatctacgtattagtcatcgctattaccatggtgatgcggtttt

ggcagtacatcaatgggcgtggatagcggtttgactcacggggatttccaagtctccacccattgacgtcaatgggagtttgttttggcacca

aaatcaacgggactttccaaaatgtcgt<u>aacaactccgccccattga</u>cgcaaatgggcggtaggcgtgtacggtgggaggtctatataagc

agagctggtttagtgaaccgtcagatccgctagcgctaccggactcagatctcgagctcaagcttcgaattctgcagtcgacggtaccgcgg

gcccgggatccaccggtcgccaccatggtgagcaagggcgaggagctgttcaccggggtggtgcccatcctggtcgagctggacggcga

cgtaaacggccacaagttcagcgtgtccggcgagggcgagggcgatgccacctacggcaagctgaccctgaagttcatctgcaccaccg

gcaagctgcccgtgccctggcccacccctcgtgaccaccctgacctacggcgtgcagtgcttcagccgctaccccgaccacatgaagcag

cacgacttcttcaagtccgccatgcccgaaggctacgtccaggagcgcaccatcttcttcaaggacgacggcaactacaagacccgcgc

cgaggtgaagttcgagggcgacaccctggtgaaccgcatcgagctgaagggcatcgacttcaaggaggacggcaacatcctggggcac

aagctggagtacaactacaacagccacaacgtctatatcatggccgacaagcagaagaacggcatcaaggtgaacttcaagatccgcc

acaacatcgaggacggcagcgtgcagctcgccgaccactaccagcagaacacccccatcggcgacggccccgtgctgctgcccgaca

accactacctgagcacccagtccgccctgagcaaagaccccaacgagaagcgcgatcacatggtcctgctggagttcgtgaccgccgcc

gggatcactctcggcatggacgagctgtacaagtaaagcggccgcactcctcaggtgcaggctgcc<u>tatcagaaggtggtggctgg</u>tgtgg

ccaatgccctggctcacaaataccactgagatctttttccctctgccaaaaattatggggacatcatgaagccccttgagcatctgacttctgg

ctaataaaggaaatttattttcattgcaatagtgtgttggaattttttgtgtctctcactcggaaggacatatgggagggcaaatcatttaaaacat

cagaatgagtatttggtttagagtttggcaacatatgcccatatgctggctgccatgaacaaaggttggctataaagaggtcatcagtatatga

aacagcccctgctgtccattccttattccatagaaaagccttgacttgaggttagattttttttatattttgtttgtgttatttttttctttaacatcccct

aaaattttccttacatgttttactagccagattttcctcctctcctgactactcccagtcatagctgtccctcttctcttatggagatccctcgacct

gcagcccaagcttggcgtaatcatggtcatagctgtttcctgtgtgaaattgttatccgctcacaattccacacaacatacgagccggaagca

taaagtgtaaagcctggggtgcctaatgagtgagctaactcacattaattgcgttgcgctcactgcccgctttccagtcgggaaacctgtcgtg

ccagcggatccgcatctcaattagtcagcaaccatagtcccgcccctaactccgcccatcccgcccctaactccgcccagttccgcccatt

ctccgccccatggctgactaatttttttttatttatgcagaggccgaggccgcctcggcctctgagctattccagaagtagtgaggaggctttttt g

gaggcctaggcttttgcaaaaagctaacttgtttattgcagcttataatggttacaaataaagcaatagcatcacaaatttcacaaataaagc

atttttttcactgcattctagttgtggtttgtccaaactcatcaatgtatcttatcatgtctggatccgctgcattaatgaatcggccaacgcgcggg

gagaggcggtttgcgtattgggcgctcttccgcttcctcgctcactgactcgctgcgctcggtcgttcggctgcggcgagcggtatcagctcac

tcaaaggcggtaatacggttatccacagaatcaggggataacgcaggaaagaacatgtgagcaaaaggccagcaaaaggccaggaac

cgtaaaaaggccgcgttgctggcgttttttccataggctccgccccccctgacgagcatcacaaaaatcgacgctcaagtcagaggtggcga

aacccgacaggactataaagataccaggcgtttccccctggaagctccctcgtgcgctctcctgttccgacccctgccgcttaccggatacct

gtccgcctttctcccttcgggaagcgtggcgctttctcatagctcacgctgtaggtatctcagttcggtgtaggtcgttcgctccaagctgggctg

tgtgcacgaaccccccgttcagcccgaccgctgcgccttatccggtaactatcgtcttgagtccaacccggtaagacacgacttatcgccac

tggcagcagccactggtaacaggattagcagagcgaggtatgtaggcggtgctacagagttcttgaagtggtggcctaactacggctacac

tagaagaacagtatttggtatctgcgctctgctgaagccagttaccttcggaaaaagagttggtagctcttgatccggcaaacaaaccaccg

ctggtagcggtggtttttttgtttgcaagcagcagattacgcgcagaaaaaaaggatctcaagaagatcctttgatcttttctacggggtctgac

gctcagtggaacgaaaactcacgttaagggattttggtcatgagattatcaaaaaggatcttcacctagatcctttaaattaaaaatgaagttt

taaatcaatctaaagtatatatgagtaaacttggtctgacagttaccaatgcttaatcagtgaggcacctatctcagcgatctgtctatttcgttc

atccatagttgcctgactccccgtcgtgtagataactacgatacgggagggcttaccatctggccccagtgctgcaatgataccgcgagacc

cacgctcaccggctccagatttatcagcaataaaccagccagccggaagggccgagcgcagaagtggtcctgcaactttatccgcctcca

tccagtctattaattgttgccgggaagctagagtaagtagttcgccagttaatagtttgcgcaacgttgttgccattgctacaggcatcgtggtgt

cacgctcgtcgtttggtatggcttcattcagctccggttcccaacgatcaaggcgagttacatgatcccccatgttgtgcaaaaaagcggttag

ctccttcggtcctccgatcgttgtcagaagtaagttggccgcagtgttatcactcatggttatggcagcactgcataattctcttactgtcatgcc

atccgtaagatgcttttctgtgactggtgagtactcaaccaagtcattctgagaatagtgtatgcggcgaccgagttgctcttgcccggcgtca

atacgggataataccgcgccacatagcagaactttaaaagtgctcatcattggaaaacgttcttcggggcgaaaactctcaaggatcttacc

gctgttgagatccagttcgatgtaacccactcgtgcacccaactgatcttcagcatcttttactttcaccagcgtttctgggtgagcaaaaacag

gaaggcaaaatgccgcaaaaaagggaataagggcgacacggaaatgttaatactcatactcttcctttttcaatattattgaagcatttatc

agggttattgtctcatgagcggatacatatttgaatgtatttagaaaaataaacaaatagggggttccgcgcacatttccccgaaaagtgccac

ctgggtcgacattgattattga-3'

Annex 2:

**Table 12.** Constituents of the various reactions for primers functionalization.

	COOH⁻ (mmols)	EDC (mmol)	sulfo-NHS (mmol)	EGFP (mmol)	EDC/sulfo-NHS:EGFP	EGFP:COOH⁻	Purification method
1	7.12×10^{-6}	5.43×10^{-6}	5.31×10^{-6}	2.66×10^{-6}	2:1	25:67	Centrifugation
2	7.12×10^{-6}	2.66×10^{-5}	2.66×10^{-5}	2.66×10^{-6}	10:1	25:67	Centrifugation
3	7.12×10^{-6}	2.66×10^{-3}	2.66×10^{-3}	2.66×10^{-6}	1000:1	25:67	Centrifugation and VIVASPIN 500
4	7.12×10^{-6}	2.66×10^{-3}	2.66×10^{-3}	2.66×10^{-4}	10:1	2500:67	Centrifugation
5	7.12×10^{-6}	1.06×10^{-3}	1.06×10^{-3}	1.06×10^{-5}	100:1	100:67	Centrifugation

Annex 3:
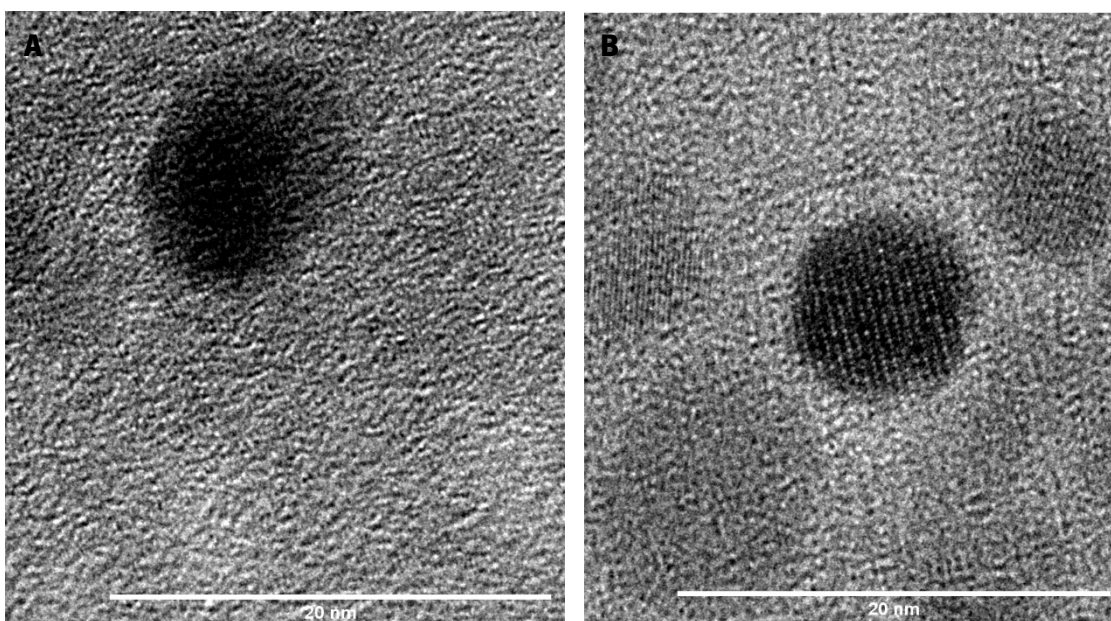
Figure 38. Crystalline morphology-like of formulations (II) and (III), **(A)** and **(B)**, respectively. Scale bars are 20 nm.

Annex 4:
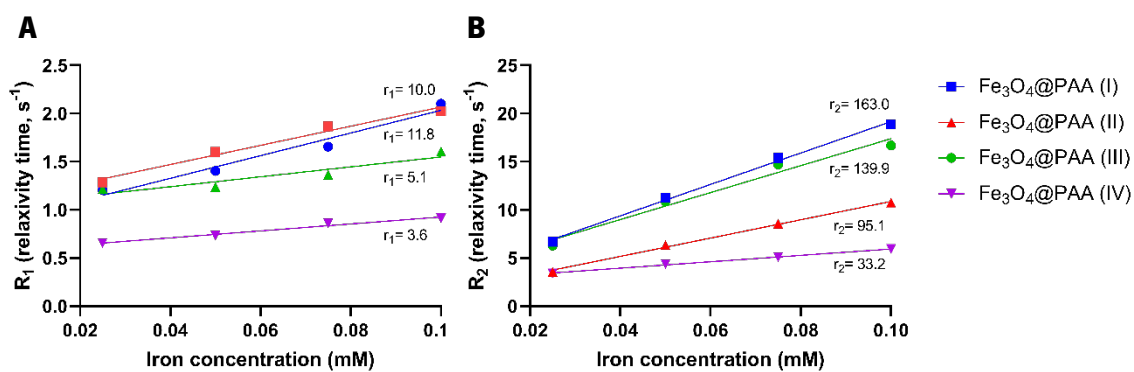
Figure 39. Linear regressions of the inverse of the relaxation time (relaxivity time, in seconds[-1]) dependence on iron concentration (mM) of MRI **(A)** T_1 (left) and **(B)** T_2 (right) maps.